Heat transfer study of millimetric zigzag channels for the development and scale-up of compact heat-exchangers reactors

Hanbin Shi

Université Fédérale
Toulouse Midi-Pyrénées

THÈSE

En vue de l'obtention du

DOCTORAT DE L'UNIVERSITÉ DE TOULOUSE

Délivré par l'Université Toulouse 3 - Paul Sabatier

Présentée et soutenue par

Hanbin SHI

Le 6 décembre 2019

Etude du transfert de chaleur en canaux millimétriques de type zigzag pour le développement et l'extrapolation de réacteurs-échangeurs compacts

---

Ecole doctorale : **MEGEP - Mécanique, Energétique, Génie civil, Procédés**

Spécialité : **Génie des Procédés et de l'Environnement**

Unité de recherche :
LGC - Laboratoire de Génie Chimique

Thèse dirigée par
Michel CABASSUD et Nathalie RAIMONDI

Jury

M. **Jean-Marc COMMENGE,** Rapporteur
M. **Daniel BOUGEARD,** Rapporteur
Mme Kamelia BOODHOO, Examinatrice
M. Christophe GOURDON, Examinateur
M. Michel CABASSUD, Directeur de thèse
Mme Nathalie RAIMONDI, Directrice de thèse
M. David FLETCHER, Invité

Abstract

This thesis is about the thermal characterization of compact heat-exchanger (HEX) reactors. The objective is to measure heat transfer coefficients in these devices and understand the effect of intensification of heat transfer related to their geometry. The compact HEX reactor prototypes used are composed of three plates: two plates called process plate and utility plate where millimetric square straight or zigzag channels are engraved, separated by an aluminum plate. The heat transfer coefficient is measured experimentally and numerically. The influence of channel geometry, fluid properties and flow rates on heat transfer is discussed. An experimental method for measuring the local temperature is implemented, based on laser-induced fluorescence. Finally, the effect of scale-up of these devices for the implementation of competitive exothermic reactions is studied.

Résumé

Cette thèse porte sur la caractérisation thermique de réacteurs échangeurs de chaleur compacts. Le but est de mesurer des coefficients de transfert thermique dans ces appareils et de comprendre l'effet d'intensification du transfert thermique lié à leur géométrie. Des prototypes de réacteurs échangeurs sont utilisés, composés de trois plaques : deux plaques dites « procédé » et « utilité » où sont gravés des canaux millimétriques droits ou en zigzag de section carrée, séparées par une plaque en aluminium. Le coefficient de transfert de chaleur est déterminé expérimentalement et numériquement. L'influence de la géométrie du canal, des propriétés des fluides et des débits sur le transfert de chaleur est discutée. Une méthode expérimentale de mesure de la température locale est mise en œuvre, basée sur de la fluorescence induite par laser. Enfin, l'effet d'un changement d'échelle de ces appareils pour la mise en œuvre de réactions compétitives exothermiques est étudié.

Table of contents

Introduction vii

Chapter I: Bibliography 1

1. Process intensification 1

2. Presentation of several intensified reactors 5

2.1 Rotating packed bed reactors 5

2.2 Spinning disk reactor 7

2.3 Microreactors 9

2.4 Static mixers 10

2.5 Heat-exchanger reactors 12

2.5.1 Generalities 12

2.5.2 Alfa Laval Plate Reactor 13

2.5.3 Corning Advanced-Flow™ Reactors 14

2.5.4 Chart Shimtech reactor 15

2.5.5 Heat-exchanger reactor SiC/Al 16

3. Millimetric zigzag channel 17

3.1 Flow characteristics 17

3.1.1 Laminar flow regime 17

3.1.2 Secondary flow 18

3.1.3 Chaotic flow 19

3.2 Hydrodynamic performances 21

3.2.1 Residence time distribution and mixing 21

3.2.2 Pressure drop 22

3.3 Thermal performances 23

4. Conclusion 29

Chapter II: Experimental method for the heat transfer study 31

1. Materials and methods 31

1.1 Experimental prototypes 31

1.2 Experimental setup 33

1.3 Method for heat transfer coefficient calculation 35

2. Heat transfer performance of prototypes (zigzag and straight channels)..... 39
2.1 Overall heat transfer coefficient 39
2.2 Heat transfer coefficient in zigzag channels 40
3. Influence of fluid properties on heat transfer in prototypes with zigzag channels 42
3.1 Overall heat transfer coefficient 42
3.2 Heat transfer coefficient in zigzag channels 43
3.3 Global heat transfer performances of HEX reactors with millimetric channels 44
4. Dimensionless correlation for heat transfer coefficient in zigzag channels 45
5. Conclusion 48
Chapter III : Numerical method for heat transfer study 51
1. Numerical method 51
1.1 Equations and solution method..... 51
1.2 Computational domain and meshing method 52
2. Results and discussion 54
2.1 Parameters of interest: definitions 54
2.2 Grid independence studies 55
2.3 Local results..... 56
2.3.1 Analysis of the temperature field..... 56
2.3.2 Evolution of *Nu* and *f* versus *Re* 60
2.3.3 Evolution of *Nu* and *f* versus L_s 65
2.3.4 Fourier analysis for non-periodic flow detection..... 67
2.4 Global results 69
2.4.1 Average Nusselt number and friction factor..... 69
2.4.2 Heat transfer enhancement..... 71
2.4.3 Thermo-hydraulic performance factor..... 72
3. Comparison between simulation and experimental results..... 74
4. Conclusions 76
Chapter IV: Characterization of temperature field by laser-induced fluorescence 79
1. Principle of laser-induced fluorescence thermometry with two dyes 79
1.1 Fluorescence signal equation..... 79

1.2 Temperature measurement based on two dyes 80
2. Materials 82
2. 1 Chemicals 82
2.2 Experimental prototypes and channel geometries 83
2.3 Experimental setup 83
3. Method 85
3.1 Temperature calibration experiment 85
3.2 Temperature measurement in heat transfer experiment 85
3.3 Image processing 86
3.3.1 Image registration between two cameras 86
3.3.2 Image registration between an experiment and that at the reference temperature 87
4. Results 87
4.1 Temperature calibration 87
4.1.1 Calibration equation 87
4.1.2 Calibration verification 89
4.2 Temperature measurement in heat transfer experiment 90
4.3 Comparison between temperature calculated with LIF and heat transfer model 94
5. Conclusion 98
Chapter V: Study of heat transfer performance in compact HEX reactors with implementation of chemical reactions 101
1. Chemical reaction 101
2. Simulation model 103
2.1 Geometry of HEX reactors 103
2.2 Assumptions 104
2.3 Calculation of concentration and temperature 104
3. Results 106
3.1 Reaction case $E_1 > E_2$ 106
3.2 Reaction case $E_1 < E_2$ 110
4. Conclusion 115
General conclusion 117

References **121**
Nomenclature **131**
Appendix A: Experimental data in Chapter II **137**

Introduction

The concept of process intensification emerged 40 years ago. Although the initial aim was to reduce the cost of units by reducing the size, there are other obvious benefits from size reduction, such as process safety, energy efficiency and environmental impact. Indeed the industrial pollution is nowadays singled out for its significant contribution to climate change, terrestrial and aquatic ecosystem degradation and public health deterioration. Therefore the industries have to modify their processes or develop new ones to insure their sustainability. The concept of the "factory of the future" has evidently emerged recently due to the significant technological progresses in terms of equipment manufacturing techniques, digitalization, robotics… The objectives of the factory of the future are to propose sustainable processes where the human work is facilitated and secured and that participate to the safe and clean territorial reindustrialization.

The intensification of the chemical processes requires the use of performant, flexible and compact technologies. For reaction engineering, numerous devices have been developed over the past decade such as compact heat-exchanger (HEX) reactors. They are miniaturized and multi-functionalized equipment with many advantages such as good heat transfer performances, better temperature control and reactive volume confinement. Despite the very successful demonstrations of these devices for the implementation of highly exothermic reactions, their use in industry is still marginal. The main obstacle to develop these technologies is the low capacity of production. Scale-up is then required to increase the capacity of the intensified reactors. For this step, the main challenge is the determination of scale-up laws to be able to estimate the size of the device that will provide the best compromise between production increase and performance degradation. The final objective will then be to guide the choice between different scale-up strategies based on device numbering-up and/or scaling-up.

This thesis is about the thermal characterization of compact HEX reactors with zigzag channels. The objective is to measure the heat transfer coefficient in these devices by different techniques (experimental and numerical) and to evaluate the effect of intensification of heat transfer related to their geometry. The influence of the channel geometry in terms of hydraulic diameter and straight length between bends on the heat transfer coefficient has been particularly studied. The characterization methods have been adapted to compact devices to correlate the heat transfer coefficient in terms of fluid properties, channel geometry and operating conditions.

In Chapter I, the concept of process intensification is firstly introduced. Some intensified reactors are presented, in particular the compact HEX reactors. Their global thermo-hydraulic performances are described and possible methods for the characterization proposed in the literature are discussed.

In Chapter II, the experimental method for thermal performance characterization of compact HEX reactors is described and discussed, based on temperature measurement by thermocouples at the channel inlet and outlet. A correlation of Nusselt number is proposed in terms of Reynolds number, Prandtl number and geometric parameters.

In Chapter III, a numerical method based on computational fluid dynamics (CFD) simulation is used to study the flow and heat transfer. It allows the acquisition of local information like velocity and temperature fields which can be used to analyze and understand the overall performances of compact HEX reactors.

In Chapter IV, an experimental technique based on laser-induced fluorescence thermometry with two-color/two-dyes is developed for local temperature measurement in compact HEX reactors. The accuracy of the method is discussed in comparison with the temperature calculated from a heat transfer model.

In the last chapter, a 1D plug flow model is used to evaluate different scale-up strategies of compact HEX reactors with zigzag channels. Conversion, selectivity and hot point are determined as a function of the channel hydraulic diameter for two reaction cases: temperature favors the formation of the main product and temperature favors the formation of the by-product.

Chapter I: Bibliography

1. Process intensification

The concept of process intensification emerged in the late 1970s, introduced by Ramshaw in the company ICI (UK) with the simple goal of reducing the plant capital cost by reducing the size or volume of the process plant components. In 1995, Ramshaw [1] made a definition of process intensification as a strategy for making dramatic reductions in the size of a chemical plant so as to reach a given production objective. This definition is quite narrow, for example the decrease of energy consumption and waste can also be considered as process intensification. This concept was then broadened by Stankiewicz and Moulijn [2]: « any chemical engineering development that leads to a substantially smaller, cleaner, and more energy efficient technology is process intensification ».

At the beginning, process intensification is merely driven by the economic interest of reducing the equipment size in the plant to reduce the capital cost. However, the size reduction of equipment is often coupled to the reduction of the total amount of chemicals (toxic, flammable...) present in the production plant (from the raw materials to the final products) which reduces the inherent risk of the process. Then the reduction of the devices also brings flexibility of production and an easy control of the industrial processes. Of course, size reduction can also enhance mass transfer and/or heat transfer performances of the devices by increasing the relative importance of fluxes through surfaces (interfacial area, heat exchange area…) compared to the production of mass and/or heat in the volumes. In reaction engineering, this can make possible to reach higher yield and selectivity for transfer limited reactive processes without changing the chemical route of synthesis. Reduction in the energy consumption of separation operations can then be expected. Inspired by these advantages, lots of process intensification projects have been carried out in this century, such as the project of Rhodia [3] and the ‘project House’ of Degussa [4].

Many routes have been considered in recent years to intensify processes. Stankiewicz and Moulijn [2] divided them into two parts: by the use of intensified equipment (novel equipment for intensifying reaction, mixing and heat exchange) and/or intensified methods (integration of reaction with other unit operations, development of new hybrid separations and application of alternative energy sources in processes) as presented in Figure I-1.

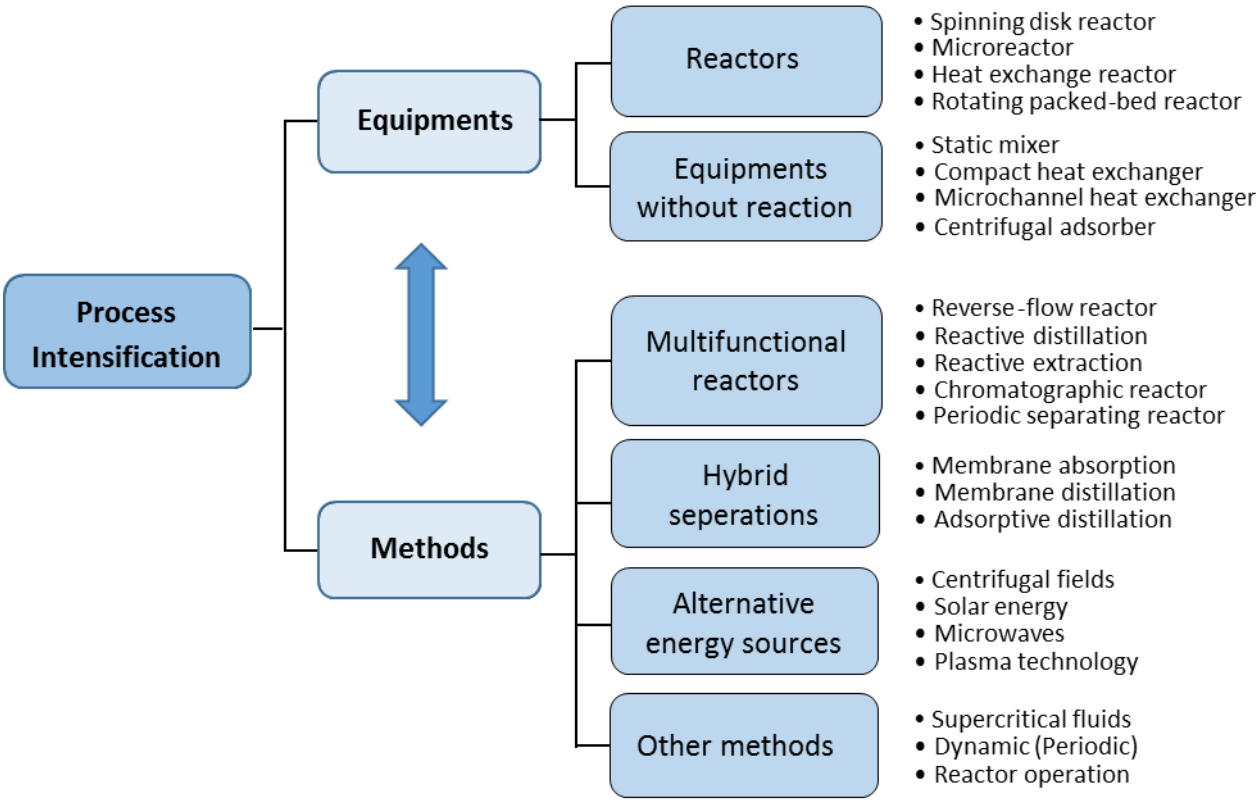

Figure I-1: Process intensification classification by Stankiewicz and Moulijn [2]

Following this classification, Ponce-Ortega et al. [5] presented a new process intensification classification as they found some "limitations" in the previous works that focused on unit-based intensification, not overall process-plant intensification: the strong interactions among unit operations within the process were ignored and the effect of one unit intensification on the rest of the process was not considered. Ponce-Ortega et al. firstly provided new definition of process intensification that lies in one or more of the following:

• Smaller equipment for given throughput, producing the same throughout using smaller equipment or less volume than commonly used today.

• Higher throughput for given equipment size or given process, producing higher throughput using the same equipment or process.

• Less holdup for equipment or less inventory for process of certain material for the same throughput, reducing holdup or inventory of certain material for the same production.

• Less usage of utility materials (heating or cooling utilities, solvents…) and feedstock for a given throughput and given equipment size.

• Higher performance for given unit size, improving unit performance (heat duty of heat exchanger, yield of reactor) for given unit size and throughput.

Based on this definition, they proposed a new classification of process intensification which is divided into two main classes: unit intensification and plant intensification, as shown in Figure I-2. They furtherly proposed a general mathematical formulation for each intensification process with the consideration of the existing units and new units through a disjunctive formulation.

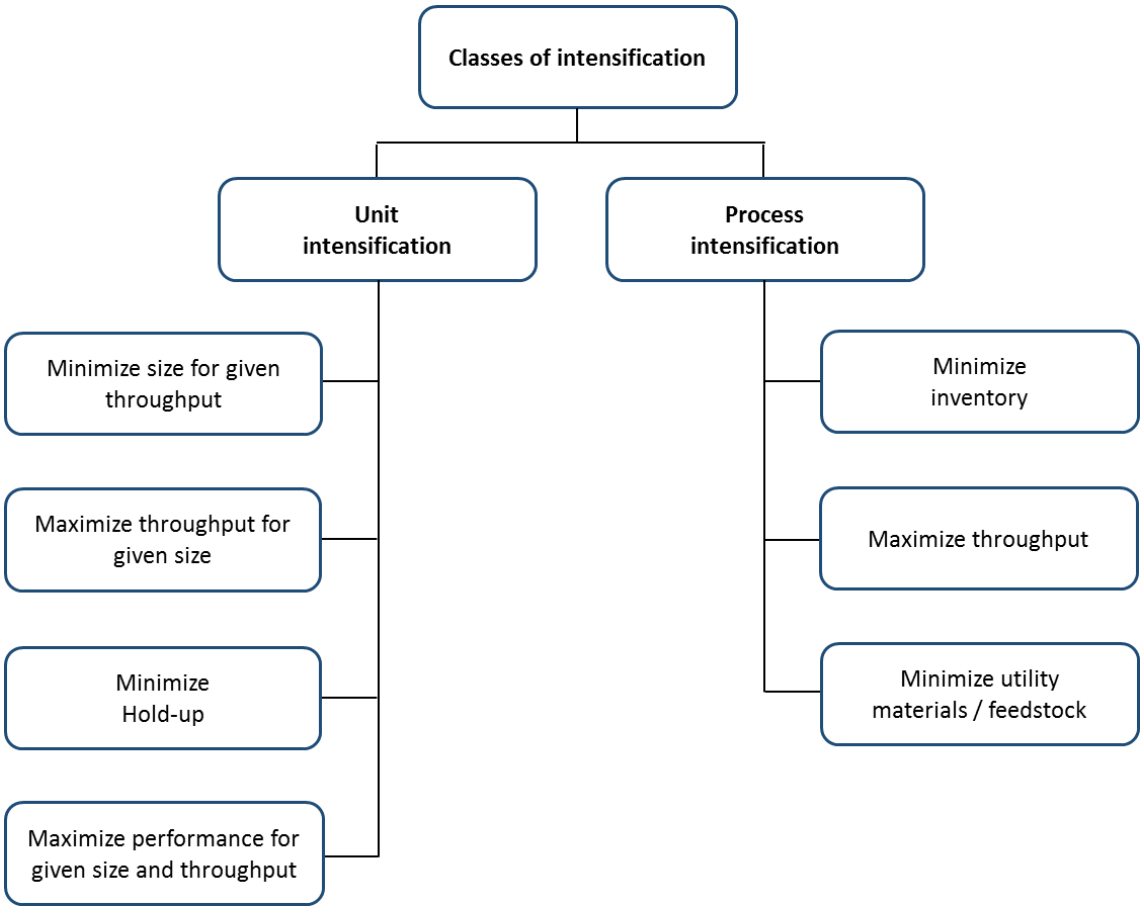

Figure I-2: Process intensification classification by Ponce-Ortega et al [5]

Gerven and Stankiewicz [6] presented a more comprehensive and fundamental view on process intensification (as shown in Figure I-3), which includes the generic principles and different approaches to realize these principles at all scales, as they found that most of the definitions

only partly grasped the complete picture of process intensification. They defined four principles of process intensification are as follows:

Principle 1: Maximize the effectiveness of intra- and intermolecular events. This principle is primarily about changing reaction kinetics. Process intensification should look for the engineering methods to better control the factors that affect the reaction kinetics.

Principle 2: Give each molecule the same processing experience. This principle is not only about macroscopic residence time distribution, dead zones, or bypassing but also meso- and micromixing as well as temperature gradients. A plug-flow reactor with gradientless, volumetric heating is very close to the idea of this principle.

Principle 3: Optimize the driving forces at every scale and maximize the specific surface area to which these forces apply. This principle is about the transport rates across interfaces. Increased transfer areas (or surface-to-volume ratios) can be obtained by changing the length scale, e.g., from the millimeter to the micrometer scales.

Principle 4: Maximize the synergistic effects from partial processes. Synergistic effects should be sought and utilized at all possible scales. Most commonly such utilization is the multifunctionality on the macroscale.

They distinguished four approaches in four domains: spatial, thermodynamic, functional, and temporal, which can realize the four principles presented above. They named these four approaches “structure”, “energy”, “synergy” and “time”. They furtherly divided the process intensification into three scales: molecular scale (molecular collisions and diffusion), mesoscale (particles, bubbles, films, phases) and macroscale (processing units and plants).

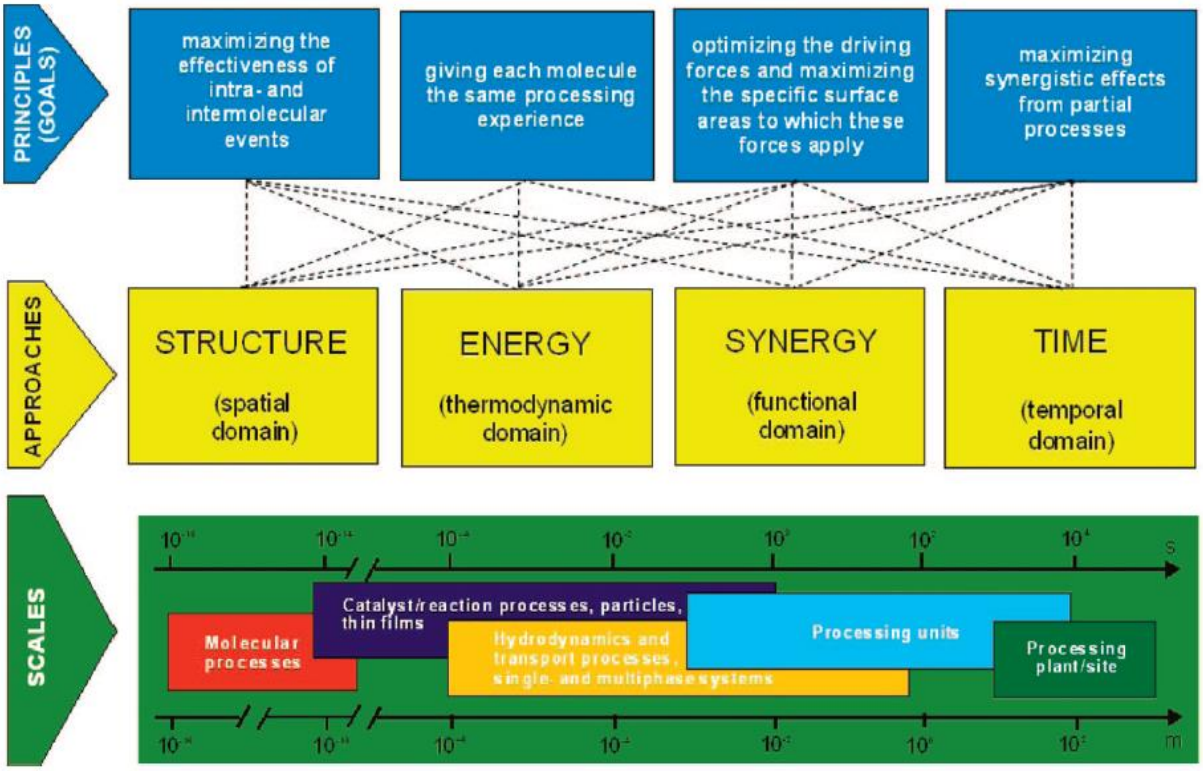

Figure I-3: Fundamental view on process intensification based on four principles and including four approaches within four domains [6]

2. Presentation of several intensified reactors

In chemical engineering, the reactor is the most important part in the process since it is the unit for carrying out chemical reactions and for the synthesis of various products. In this part, several continuous intensified reactors are presented which draw great concern in the process intensification. The technologies described are chosen in agreement with those identified in Figure I-1. They are rotating packed bed reactors, spinning disk reactors and microreactors, with different process intensification strategies. Static mixers are also included in this descriptive part as they are often used upstream of reactors for efficient reactant mixing. Finally heat-exchanger reactors will be presented more in details as they constitute the object of this thesis work.

2.1 Rotating packed bed reactors

Rotating packed bed reactors have drawn great attention as a method for process intensification in the last three decades. This technology (HiGee) was developed by Ramshaw and his co-workers [7] in the late 1970s at ICI, UK, which showed excellent mass transfer performances.

Since then, many researches on rotating packed bed reactors have been carried out and many applications have been installed in the industry for various productions, among which the nanoparticles are the most popular. Kang et al. [8] presented a novel mass-transfer intensified approach for efficient preparation of monodisperse $CaCO_3$ nanoparticles as overbased nanodetergents with rotating packed bed reactors. Fan et al. [9] reported a continuous technique for the preparation of Fe_3O_4 nanoparticles using impinging stream-rotating packed bed reactor. Lin and his coworkers reported the preparation of CuO nanoparticles and ZnO nanoparticles by the precipitation method in rotating packed bed reactors [10,11].

Rotating packed bed reactors consist of an annular cylindrical rotor with a packed bed and a static housing. The rotor is driven by the motor, generating the centrifugal force which can tremendously improve micromixing as well as heat transfer. The schematic of a rotating packed bed reactor for liquid-liquid processes is shown in Figure I-4 [12]. The rotor is the most important part in rotating packed bed reactors which can be made of various packing types, like gas spheres, solid foam, and discs [13]. Rotating packed bed reactors are normally operated for gas-liquid processes (counter-currently) and liquid-liquid processes (co-currently).

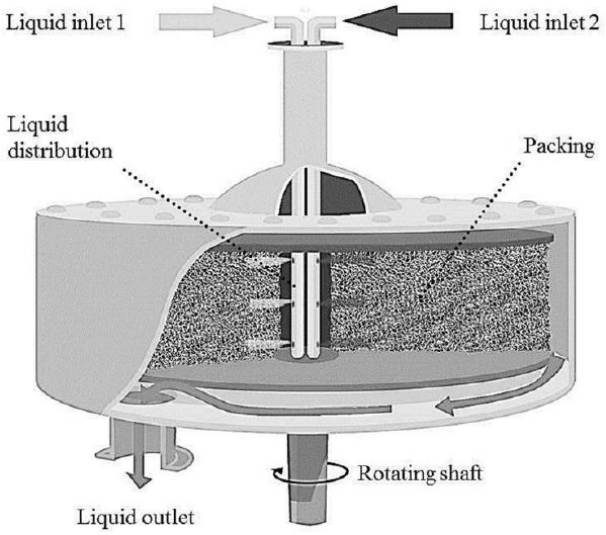

Figure I-4: Schematic of a rotating packed bed reactor for liquid-liquid processes [12]

Zhao et al. [14] reviewed the advances on the high gravity (Higee) technology in rotating packed bed reactors, including the studies on liquid flow, gas-liquid mass transfer, residence time distribution and micromixing, and its applications in absorption, stripping, nanoparticles preparation, sulfonation, polymerization and emulsification. Wenzel and Górak [12] made a review on the fundamentals of liquid micromixing in rotating packed bed reactors and delivered

an assessment of micromixing based on the Villermaux-Dushman protocol. Shi et al. [15] performed numerical study on the liquid phase flow patterns in rotating packed bed reactors. Neumann et al. [16] made a review of industrial rotating packed bed reactor applications and introduced a guide (distinctive decision trees) to facilitate the identification of processes where it is beneficial to use rotating packed bed reactors.

2.2 Spinning disk reactor

Spinning disk reactor (SDR) is another type of reactor that uses Higee technology. Spinning disk reactor generally has a working disk with a diameter between 60 mm and 500 mm which can be heated or cooled (as shown in Figure I-5), it is connected to a motor which can generate centrifugal and shear forces and form a thin liquid film (20-300 μm). This can create a high surface-to-volume ratio and gives a heat transfer coefficient up to 25 $kW.m^{-2}.K^{-1}$ [17]. The rotational speed ranges from 100 to 6000 rpm (typically around 1000 rpm) [18]. The reactants (process fluid) are introduced in the center of the disk, they travel across the surface and form a thin liquid film in the surface of the disk. The liquid leaves the edge of the disk and can be collected. The heat transfer fluid is introduced from the below of the disk and passes countercurrently with the process fluid, as presented in the following figure.

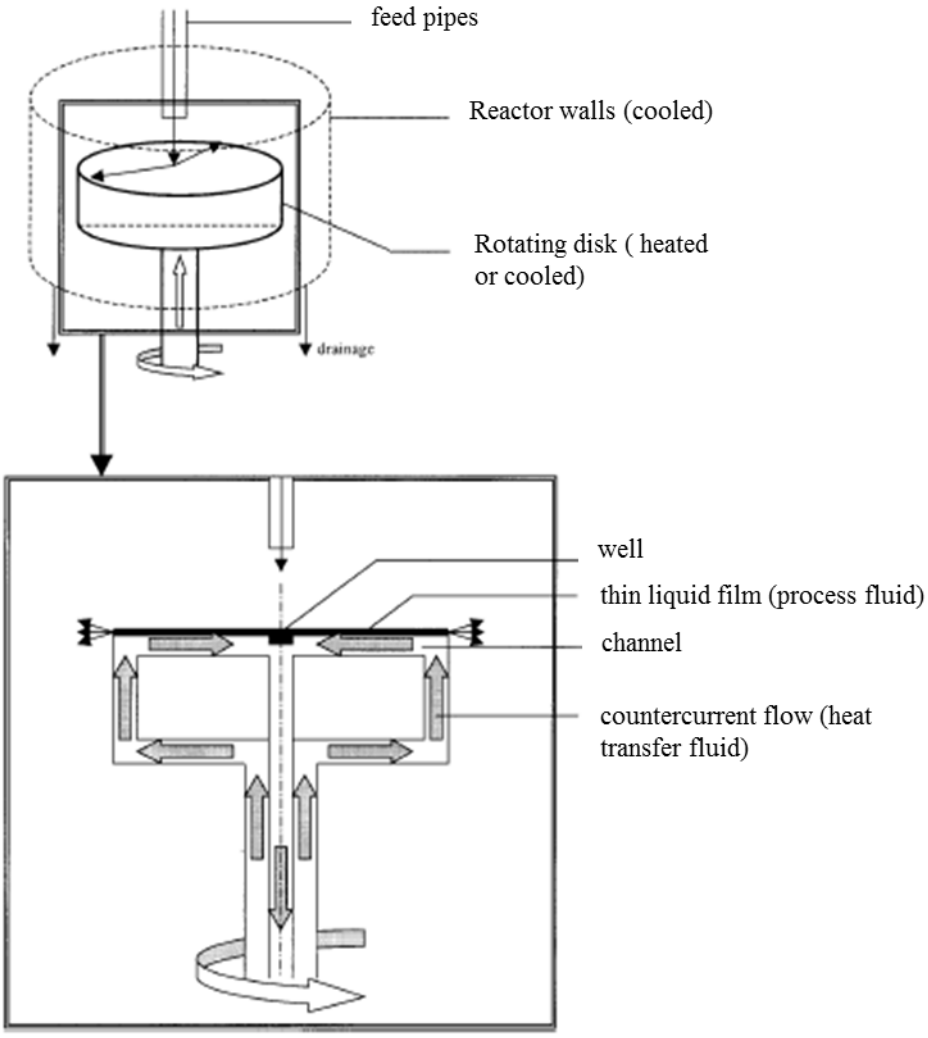

Figure I-5: Schematic of spinning disk reactor [19]

Spinning disk reactor has the characteristics like intense mixing in the thin liquid film, short residence time, plug flow behavior and high solid/liquid, liquid/vapour heat and mass transfer [18]. These properties allow the wide use of spinning disk reactor in chemical reactions. Boodhoo and Jachuck [20] studied the styrene polymerization (highly exothermic reaction) in a spinning disk reactor, their results showed SDR can significantly enhance the reaction rate, improve product quantity and inherent safety. Oxley et al. [19] evaluated a spinning disk reactor for the manufacture of pharmaceuticals, they found SDR technology displayed many advantages over traditional batch processes in terms of reaction time, inventory, product purity and particle size distribution. Qiu et al. [21] studied experimentally and numerically the synthesis of biodiesel in a two-disk spinning disk reactor and investigated the effects of disk speed, volumetric flowrate, temperature, disk design, etc. to the reactor performance. There are

also many applications of SDR in the preparation of nanoparticles, such as AgI, TiO_2, and $BaSO_4$ [22–24].

2.3 Microreactors

Microreactors gained lots of interest in last two decades due to their excellent mixing and heat transfer performances. There are many researches on microreactors and their application for chemical synthesis carried out at lab-scale as well as at industrial-scale. Many industrial units are based on micro-structured devices in the chemical and pharmaceutical industry. The first company who installed a production plant based on microreactors is Merck, Germany, in 1998, for a organometallic reaction based on a carbonyl compound and a metallo-organic reagent [25]. The yield of this reaction at pilot-scale (as shown in Figure I-6) is 20% better than in their former batch process.

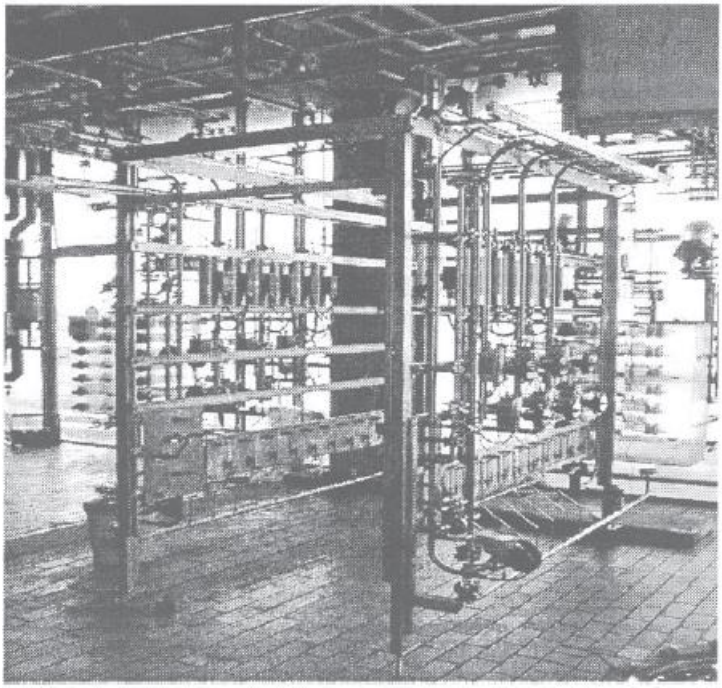

Figure I-6 : Pilot-scale production plant with microreactors (Merck, Germany) [25]

A microreactor is a device with at least one characteristic dimension below 1 mm. It has a high ratio of surface area (for heat exchange) to reaction volume due to the size reduction, its magnitude is 10000 $m^2.m^{-3}$ [26]. Consequently, the mass transfer and heat transfer are significantly improved in microreactors and the operating conditions like temperature are well controlled in the resulting confined fluid media. Highly exothermic reactions can be carried out safely in microreactors. However, the main drawbacks of microreactors are the low reaction

volume leading to low production capacity and fouling and clogging issues as microchannels are too small. Merck company designed wider channel with mixing elements for the reaction mentioned in the last paragraph, keeping good heat transfer performance and preventing the system from clogging [25]. It is applied at the pilot-scale production plant with parallel microreactors to ensure the desired production (as shown in Figure I-6).

Microreactors can be manufactured in different materials, including ceramics, polymers, stainless steel, glass and silicon [27]. There are many studies on the designing of microreactors with the purpose of better controlling the reaction parameters. Single phase reactions as well as multiphase reactions (gas-liquid, liquid-liquid, gas-liquid-solid) can be carried out in microreactors. Yao et al. [27] made a review of the recent microreactors structure and their applications on the synthesis of nanoparticles, organics, polymers and biosubstances in the last decades. Doku et al. [28] made a review of microreactor design principles and reagent contacting modes. Brian et al. [29] made a review about the organic synthesis in microreactors. Kolb and Hesselon [30] reviewed the application of micro-structured reactors for heterogeneously catalyzed gas phase reactions.

2.4 Static mixers

Static mixers consist of identical and immobile inserts which can be installed in a tube, column or reactor. The function of the inserts is to redistribute the fluid on the radial direction with respect to the main flow direction to significantly enhance radial mixing. The effectiveness of this redistribution depends on the design and the number of inserts, the fluid properties and the volumetric flowrate. Many commercial designs are available in the industry, some of them are shown in Figure I-8 [31].

Figure I-7: Inserts of different static mixers : (a) Kenics (Chemineer) ; (b) HEV (Chemineer) ; (c) Inlier series 45 (Lightnin) ; (d) Custody transfer mixer (Komax systems) [31]

Compared with conventional mixers, static mixers are generally cheaper because there is no moving part, it can reduce energy consumption as well as the cost of maintenance. Then the static mixers can homogenize the flow with a short residence time. They can also be built on different materials: plastics, metals, etc. Moreover, there are many geometric parameters in the inserts which can be adjusted to suit different applications.

As for the chemical synthesis, the advantage of the static mixers is first of all the good mixing of the fluid. In a tube, plug flow can be approached which can highly increase the reaction rate and the yield. Then the good radial mixing reduces the radial gradient of temperature, which also enhances heat transfer. There are many applications of static mixers for chemical synthesis in industry, most of them are polymerization, such as polystyrene, nylon, urethane and sulfur compound manufacture [32–35]. They are highly exothermic reactions which are difficult to control. If the heat is not removed quickly during the reaction, it will create a lot of byproducts due to the high temperature. There is also a big concern with safety. Moreover, polymerization can be carried out in fluid media of complex rheological behavior for which static mixers have performed better than other mixing technologies.

To conclude, static mixers are widely used in industry for chemical synthesis, they have many advantages such as plug flow behavior, improvement of mixing and heat transfer, etc. Most of the applications of static mixers are for polymerization synthesis. Of course, inserts generally generate a large pressure drop which is the main disadvantage of static mixers. Today, there are still many studies on static mixers to build new designs for different specific needs.

2.5 Heat-exchanger reactors

2.5.1 Generalities

Recently numerous technologies of compact heat-exchanger (HEX) reactors have been developed to respond to the needs of safer, cleaner, more effective and less energy-consuming processes. They integrate two basic concepts of process intensification which are the miniaturization of the units and the multi-functionalization of the apparatuses. They exhibit many advantages such as good heat transfer performances, better temperature control and reactive volume confinement. Indeed, this type of reactor firstly has a large specific heat exchange area (A/V) due to the size reduction. Then this size reduction causes the reduction of the total amount of mass and heat inside the reactor which is favorable for safety concerns, especially for highly exothermic reactions. However, in order to have a sufficient residence time for the chemical reactions, the flowrate is relatively small in these devices. This results in laminar flow operating conditions which does not favor transport phenomena. Consequently, complex designs are required in order to enhance mass and heat transfer and promote plug flow behavior by interrupting the thermal boundary layer and in return enhance the heat transfer compared to technologies based on straight tubes. Compact HEX reactors can be found in various materials, such as glass, metals or silicon carbide. The objective in their conception is to design a performant heat exchanger suitable to carry out reactions, i.e. providing efficient reactant mixing, high interfacial area for multiphase reactions, and sufficient residence time to fit the reaction kinetics.

Many studies on HEX reactors can be found in the literature. Indeed, milli-structured HEX reactors have recently attracted a lot of attention in the chemical industry, especially to carry out fast and exothermic reactions. Their applications in processes are becoming wider and wider. Anxionnaz et al. [36] made a review of different kinds of compact HEX reactors and presented their applications at pilot or industrial scale. Li et al. [37] made a review on the performance of different compact HEX reactors and summarized their structures, heat transfer enhancement mechanisms, advantages and limitations. They compared these different heat transfer enhancement technologies and analyzed their thermo-hydraulic performances on the basis of available correlations. Niedbalski et al. [38,39] studied experimentally the hydrodynamic behavior and numerically the thermal performances of gas-evolving reacting flows in chevron plate heat exchangers. They developed a reduced-order semi-empirical model in order to predict the thermal performances. Chen et al. [40,41] conducted experimental and numerical studies of

thermal-hydraulic performances in a zigzag-channel as well as in a straight-channel printed circuit heat exchanger, they found good agreement between experimental and numerical results. Kwon et al. [42] investigated experimentally the heat transfer coefficient of a mini-channel printed circuit heat exchanger with counter-flow configuration at different cryogenic heat transfer conditions, they furtherly proposed correlations for each heat transfer condition. Guo et al. [43] studied experimentally and numerically the flow distribution and heat exchange performance in a multi-functional HEX reactor comprising arborescent distributors and collector, they found the heat exchange capability (UA/V) was around 200 $kW.m^{-3}.°C^{-1}$, 20 times higher than traditional tank reactors. Théron et al. [44] characterized experimentally the thermal-hydraulic performance of a compact heat exchanger reactor. Their results showed the ratio between the reaction kinetics of sodium thiosulfate oxidation by hydrogen peroxide and the mixing time is over 100 and the heat exchange capability ranges from 5000 to 8000 $kW.m^{-3}.K^{-1}$. Zhang and Sethi [45] studied the synthesis of mixed alcohols in a stainless steel compact HEX reactor with 66 mL catalyst loading, demonstrated two to four times process intensification. Bakhtyari et al. [46] studied numerically a thermally integrated coupled membrane HEX reactor designed as a co-axial exchanger surrounded by a membrane. In a single device, they found optimal conditions to promote in the inner tube the exothermic dehydration of methanol to dimethyl ether (95.1% of conversion), in the outer tube the endothermic dehydrogenation of methanol to methyl formate and hydrogen (99.6% of conversion). The membrane allows the removal of the hydrogen from the second reactional media.

Most of the equipment manufacturers that have been interested in the design of compact HEX are companies that were formerly specialized in the construction of metal heat exchanger (Alfa Laval, Chart…) or that had an expertise in specific material handling for component manufacturing (glass and ceramics for Corning, silicon carbide for Boostec-Mersen…). In this part, some compact HEX reactors developed by these companies are presented. Most of them are designed as plate heat exchanger since this configuration allows flexibility in terms of residence time by modifying the number of plates.

2.5.2 Alfa Laval Plate Reactor

Alfa Laval has developed a series of ART® Plate Reactors which are used in the production of fine and specific chemicals, such as pharmaceuticals. The ART® Plate Reactors are versatile reactors that can be easily reconfigured to suit different reaction types, such as liquid/liquid

reactions, exothermic reactions, etc. They have the advantage of being easily openable for cleaning and inspection. The reactor shown in Figure I-8(a) is the ART® Plate Reactor 37 [47]. It consists of a series of stainless steel plates where cranked channels are etched for the purpose of enhancing mixing and heat transfer. This geometry can bring plug flow and corresponding residence time distributions. The ART PR37 reactor can handle maximum flowrate of about 30 $L.h^{-1}$ which corresponds to a residence time of 45 s per plate, with a temperature ranging from -40 ° C to 200 °C. The ART® Plate Reactor 49 reactor [48] (in Figure I-8(b)) is the extension of ART PR37 which accept flow rates up to 500 $L.h^{-1}$, with a residence time of 60 s per plate.

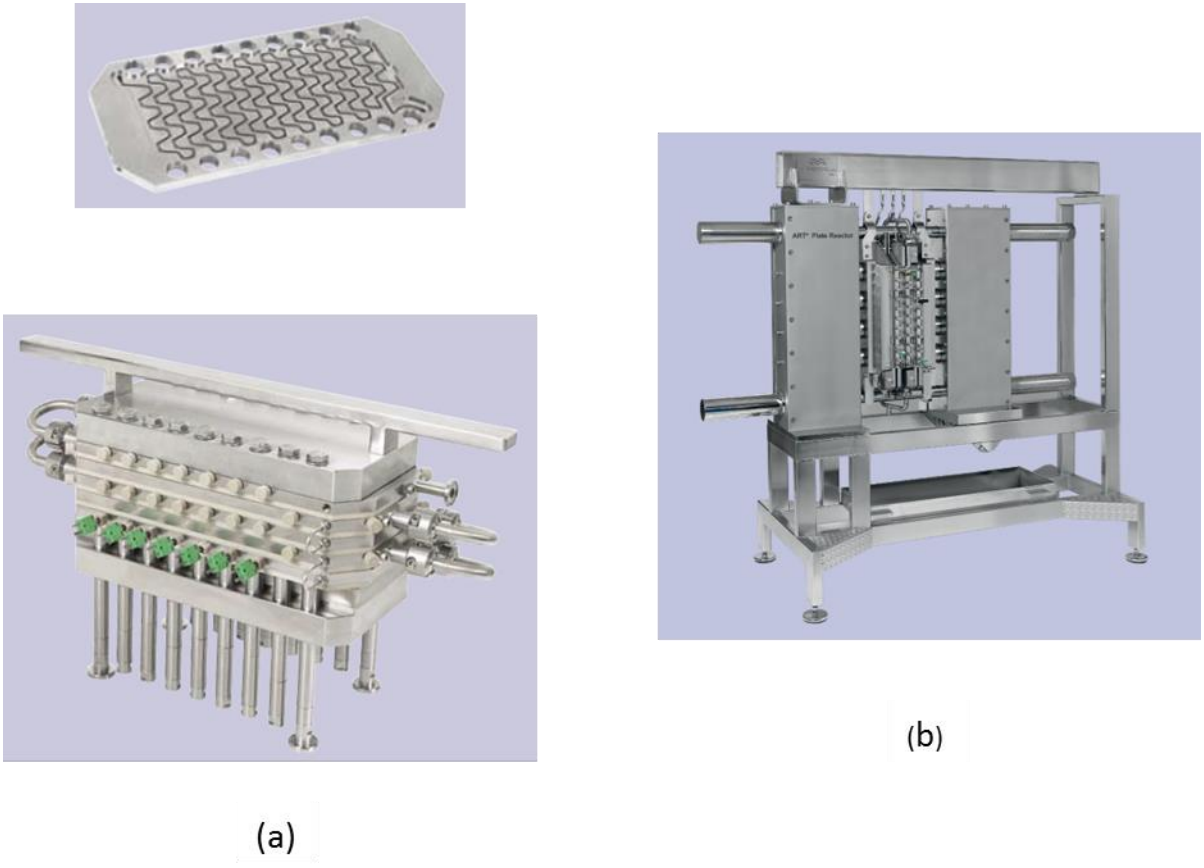

Figure I-8: Alfa Laval Plate Reactors: (a) ART PR37; (b) ART PR49

2.5.3 Corning Advanced-Flow™ Reactors

Corning has developed a range of Advanced-Flow™ Reactors at four different scales from G1 to G4 which correspond to a volume of fluid from 5 mL to 250 mL [49]. They can handle flow rates from 1 to 500 $L.h^{-1}$, with a temperature varying from -60 °C to 200 °C. Each module of the reactors is built like a sandwich where the heating or cooling fluid (utility fluid) is

introduced on both sides. The reactants are encapsulated between the two plates where the utility fluid circulates. The geometry of the channels where the reactions occur is very particular, depicting several unit cells of heart-like shape, which can provide very good performances in terms of mixing and mass and heat transfer. These reactors are commercially available in glass or silicon carbide. The G1-G3 reactors are shown in Figure I-9. Since the unit cell elements are of similar size in the four reactors, direct seamless scale-up is ensured from G1 to G4.

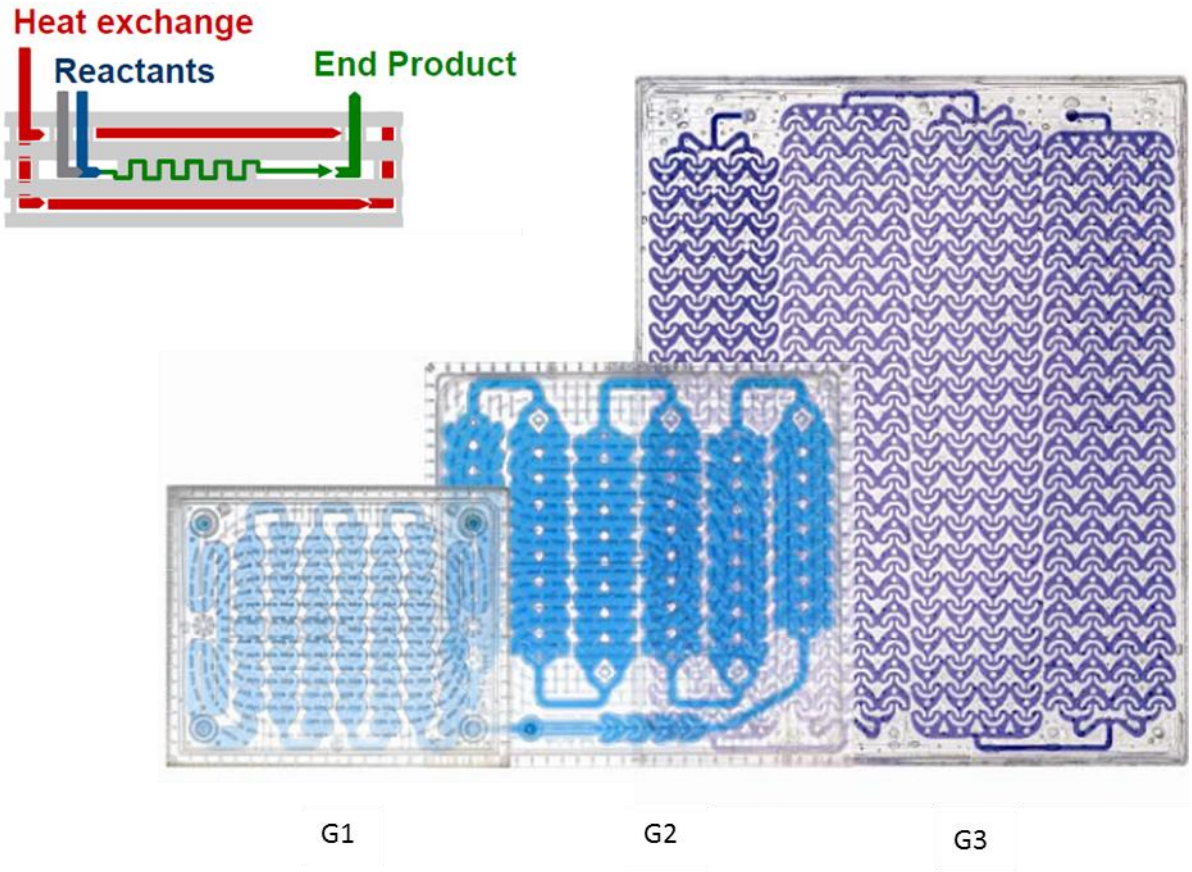

Figure I-9: Corning Advanced-Flow™ Reactors : G1-G3 [49]

2.5.4 Chart Shimtech reactor

Chart industries have developed a heat exchanger reactor named Shimtech by a diffusion welded plate assembly technology. The plates are made of stainless steel and one example of reactive plate is presented in Figure I-10 [50]. Specific geometry is engraved in the reactive plate resulting in several small structured channels in parallel to enhance mixing and heat transfer. In the reactor, each reactive plate is sandwiched between two cooling plates. This reactor can handle a flow rate up to 50 $L.h^{-1}$. A simplified scheme that illustrates the circulation of the different fluids is also shown in this figure.

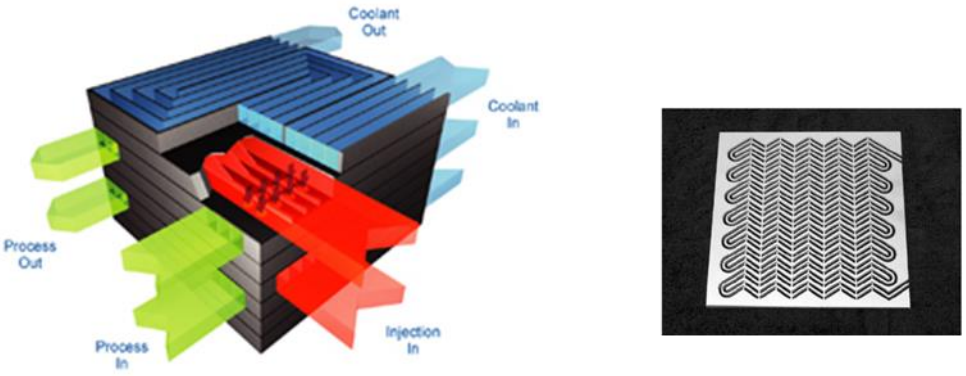

Figure I-10: Shimtech reactor of Chart industries [50]

2.5.5 Heat-exchanger reactor SiC/Al

The heat-exchanger reactor SiC/Al is a plate exchanger constructed by the company Boostec in partnership with the Laboratoire de Génie Chimique (LGC, Toulouse) and the Commissariat à l'Energie Atomique et aux Energies Alternatives (CEA, France). It consists of alternating silicon carbide (SiC) process plates and aluminum utility plates (in Figure I-11). The reactions take place in the process plates and in the utility plates the heat exchange fluid circulates. In each plate, zigzag channels of square cross-section are engraved, with a hydraulic diameter of 2 mm. The useful volume of a process plate is 9.5 mL. This reactor can handle a flow rate of 1 to 10 $L.h^{-1}$ which corresponds to a residence time of 3 - 30 s per plate. The thermal characterization of the reactor shows that the heat transfer performance is excellent [51].

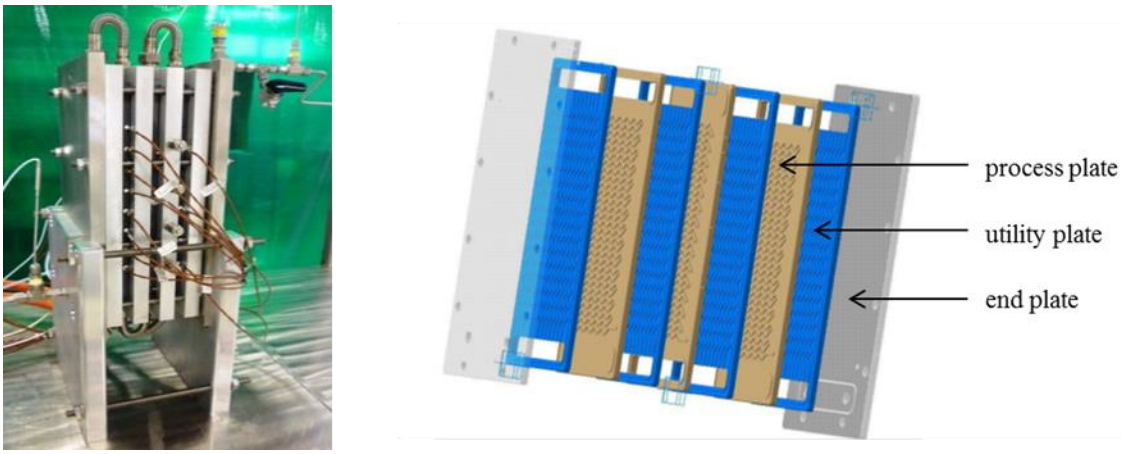

Figure I-11: Heat-exchanger reactor SiC/Al

Unlike the devices presented previously, this HEX reactor is not commercialized. Its specificity mainly lied in the use of SiC for the conception of a chemical engineering equipment. This

material is a hard ceramic, semiconductor, which presents very high chemical resistance and thermal conductivity (120 $W.m^{-2}.K^{-1}$). It is mainly used in the fields of microelectronics, aeronautics, spatial and automotive. The features make it as a choice for HEX reactor design. By the way, Boostec-Mersen now builds the Advanced-Flow ™ Reactors in SiC commercialized by Corning.

One of the advantages of the zigzag pattern is that it is characterized by numerous geometric parameters (angle of the bends, curvature, straight section length between bends, cross-sectional shape and size of the channel…) which can be modified to adapt the design to different needs. The HEX reactor presented in Figure I-11 and devices with similar design have been studied a lot at LGC in the last fifteen years. Their capabilities to handle some industrial applications have been assessed notably in the framework of collaborative projects involving the LGC and industrial partners [52–54]. Other studies have also been carried out to understand and model the influence of the operating conditions and geometric parameters of the zigzag channel on pressure drop, axial dispersion, mixing time, heat and interfacial mass transfer [26,55,56]. The works described in the present thesis are in continuation of these studies and will mainly concentrate on heat transfer performance of HEX reactors with zigzag channels. In the following section, the particular hydrodynamics in millimetric zigzag channels and their performances are presented in more details.

3. Millimetric zigzag channel

3.1 Flow characteristics

To optimize yield and selectivity, it is better to carry out a reaction in an ideal plug flow. In this flow, all the elements of fluid have the same residence time, the dead zone can be avoided and a good mixing can be achieved. This flow can avoid hot spots as well for concern of safety, especially for highly exothermic reactions. Therefore, plug flow is sought in compact HEX reactors.

3.1.1 Laminar flow regime

In order to have a sufficient residence time for the chemical reactions, the flowrate in compact HEX reactors is relatively small, normally in laminar regime. This flow regime in straight channels leads to parabolic velocity profile (Poiseuille flow) that does not favor plug flow

behavior (no velocity at the wall, maximal velocity at the channel center, no radial advection). It is obtained for Reynolds number (*Re*) below 2100:

$$Re = \frac{\rho d_h \overline{u}}{\mu} \quad \text{(I-1)}$$

where ρ, $\overline{u}$, μ are the density, mean velocity, and dynamic viscosity of the flow respectively. d_h is the hydraulic diameter of the channel, which is calculated by

$$d_h = \frac{4A}{P} \quad \text{(I-2)}$$

where *A* and *P* are the area and the perimeter of the cross-section.

The laminar flow regime is not favorable for heat transfer and mixing as well, so complex design are necessary in milli-structured HEX reactors in order to be performant. Wavy geometries are often used in milli-structured HEX reactors, as mentioned before. This kind of geometry can generate Dean vortices (secondary flow) as well as chaotic flow even with small Reynolds number, which bring radial fluid motion and hence enhance the mass transfer and heat transfer.

3.1.2 Secondary flow

The secondary flow (Dean flow) is firstly theorized by Dean [57]. It corresponds to fluid motion in curved channels perpendicular to the main direction of the flow. It is due to centripetal forces generated in the curves. This motion can be described as radial vortex. It creates radial mixing that reduces the thickness of the velocity, concentration and temperature boundary layers at the walls and interfaces, enhancing in return mixing, mass transfer and heat transfer.

This flow can be generated in wavy channels due to the presence of the bends. An example of a simulated secondary flow generated in a zigzag channel with square cross-section is presented in Figure I-12. This representation is obtained by projecting the velocity vectors perpendicularly to the main direction of the flow, i.e. over the cross-section of the channel. In this example, it can be clearly seen that there are 4 vortices.

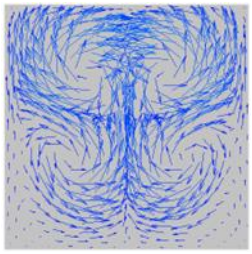

Figure I-12: Simulated secondary flow in zigzag channel with square cross-section

Many studies have been published concerning the secondary flow and its effect on mixing and heat transfer in wavy channels with different cross-sections. Wang and Liu [58] presented various secondary flow structures in slightly curved microchannels with square cross-section. Their results suggested that the secondary flow created by channel curvature can increase the Nusselt number significantly (ratio of convective to conductive heat transfer at a boundary) and the friction factor moderately. Manglik et al. [59] studied numerically the steady forced convection in wavy plate-fin channels at low Reynolds number and found the generation of secondary flow which enhanced the heat transfer as well as the pressure drop penalty. Sui et al. [60,61] performed numerical and experimental studies for laminar liquid-water flow and heat transfer in three-dimensional wavy microchannels with rectangular cross section. Their results showed that the heat transfer performance in wavy microchannels was much better than that of straight microchannels with the same cross section due to the generation of secondary flow and the pressure drop penalty could be much smaller than the heat transfer enhancement. Fletcher and his coworkers [62–68] have conducted a variety of numerical studies for steady laminar flow and heat transfer in wavy channels with different cross-sections, including trapezoidal, serpentine, and sinusoidal channels. They found the similar conclusion that Dean vortices can enhance heat transfer greatly with relatively small pressure drop penalty.

3.1.3 Chaotic flow

Zigzag channels can generate another effect for improving mixing and heat transfer which is called chaotic advection. It was firstly proposed by Aref in fluid mechanics in 1984 [69]. It describes unstable and aperiodic behavior in deterministic non-linear systems. This flow behavior can be achieved in two-dimensional unsteady flow or three-dimensional steady flow. The chaotic flow can be characterized by the Lagrangian method. Figure I-13 shows an example of the chaotic flow characterization in a zigzag channel with square cross-section obtained by Zheng et al. with CFD simulations [68]. They put the tracer particles in the cross-section at the entrance of a bend which is the straight line in Figure I-13 (a). After the numerical resolution,

they recorded the tracer particles in the cross-section after 1 bend, 4 bends and 12 bends for three Reynolds numbers (150, 200, 400). For a Reynolds number of 150 (in Figure I-13(a)-(c)), they observed moderate stretching and folding of the tracer particle line. For a Reynolds number of 200 (in Figure I-13(d)-(f)), they observed stronger stretching and folding. For a Reynolds number of 400 (in Figure I-13(i)), they found the tracer particles had almost covered the entire cross-sectional area after 12 bends. They interpreted it as chaotic advection. The enhancement of mixing by chaotic flow is stronger than by the secondary flow.

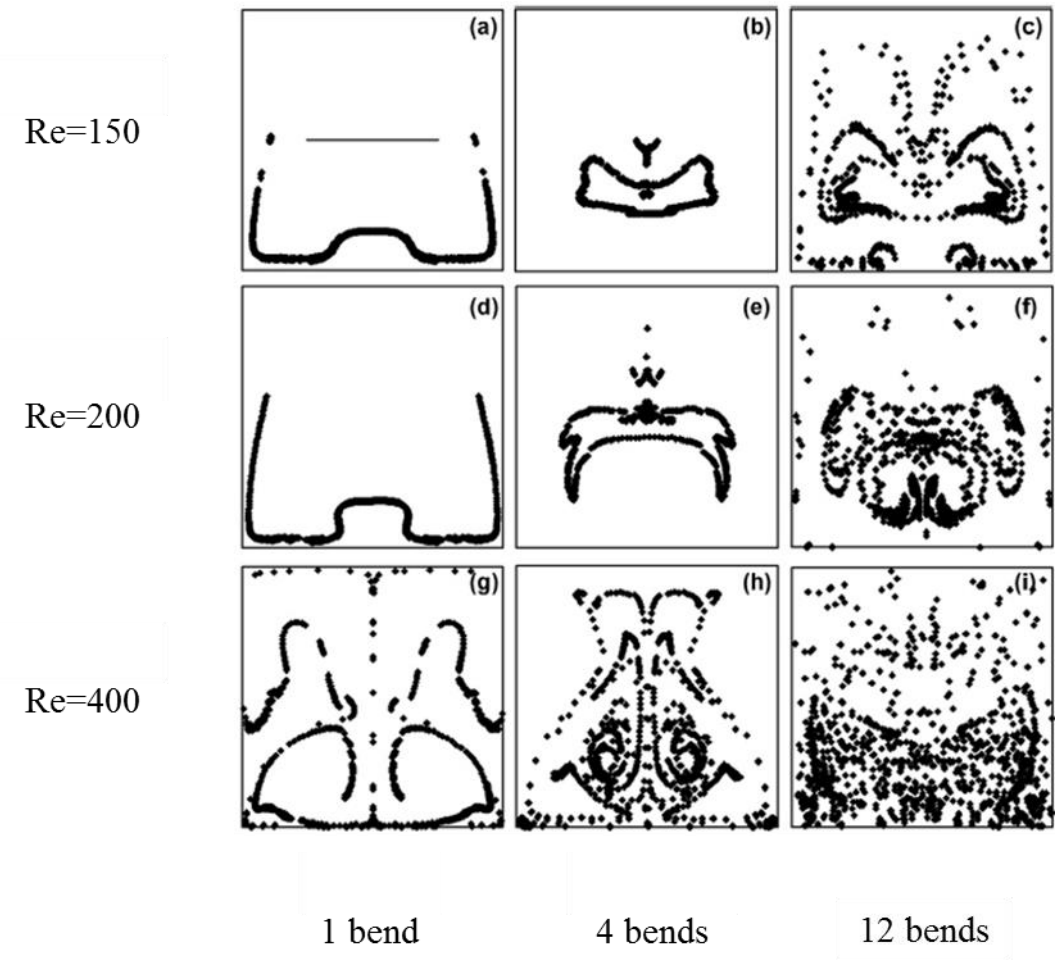

Figure I-13: Chaotic advection characterization in zigzag channel with square cross-section for Reynolds number of 150 ((a)-(c)), 200 ((d)-(f)), 400 (g)-(i)) at three cross-sections after 1 bend, 4 bends and 12 bends. The initial tracer particles is the straight line in (a) [68]

A lot of research on chaotic flow and its impact on mixing and heat transfer can be found in the literature. Liu et al. [70] presented a three-dimensional serpentine microchannel design as a means of implementing chaotic advection to enhance fluid mixing. Stroock et al. [71] presented a passive method based on staggered herringbone mixer to generate chaos for mixing streams

of steady pressure-driven flows in microchannels at low Reynolds number. Jiang et al. [72] investigated numerically and experimentally the mixing of helical flows in curved micro channels, their results showed that the hydrodynamic dispersion was substantially reduced compared to a straight channel, due to mass transfer enhancement originating from the chaotic flow. Kumar et Nigam [73] studied numerically the heat transfer in a chaotic configuration of circular cross-section under laminar regime, their results showed a 25-36% enhancement of heat transfer due to chaotic mixing while pressure drop increase was 5-6%. Castelain et al. [74,75] have conducted experimental studies of chaotic advection in a twisted duct with square cross-section, they characterized the chaotic flow and found that it was sensitive to the initial conditions. A coiled heat exchanger based on chaotic advection was designed and it showed 15-18% higher efficiency than a helically coiled tube heat exchanger. Acharya et al. [76] studied numerically and experimentally the heat transfer in an alternating axis coil. Their results showed 6-8% higher in-tube heat transfer coefficient due to chaotic mixing compared to a conventional constant axis coil, with a pressure loss increase of 1.5-2.5%.

3.2 Hydrodynamic performances

3.2.1 Residence time distribution and mixing

As mentioned before, plug flow is generally sought in continuous reactors. Péclet number *Pe* is often used to evaluate the gap to this ideal flow behavior in real continuous reactors. It is defined as follows:

$$Pe = \frac{L\bar{u}}{D_{ax}} \tag{I-3}$$

where L is the reactor length and D_{ax} is the axial dispersion coefficient. This coefficient represents the overall spreading of a component in a fluid flow along the main direction of the flow (i.e. axial direction) which is due to molecular diffusion and radial velocity profile. It is commonly considered that plug flow behavior can be assessed for $Pe > 50$. A representation by an equivalent number of stirred tanks in series N can also be used ($Pe \approx 2N - 1$). Unlike to Poiseuille flow conditions with parabolic velocity profile that does not favor plug flow, zigzag millimetric channels generate radial fluid motion and plug flow is easily obtained for fluid that are not too viscous by adjusting the zigzag geometry [77]. Radial mixing as well is enhanced. Mixing times of less than 1 s can be reached [77].

Axial dispersion coefficient can be estimated using Residence Time Distribution experiments or simulations. It consists of the injection of an inert tracer at the reactor entrance (solute or particles) in the main fluid flow, and the measurement of its concentration at the reactor outlet. The comparison between the inlet and the outlet concentration profiles allows the axial dispersion coefficient calculation using deconvolution methods. A numerical method where this coefficient is calculated from the solute concentration and velocity fields at the outlet without applying deconvolution methods has also been used successfully for millimetric channels [78].

Mixing times are generally obtained using colorimetric experiments or numerical particle tracking. Micro-mixing, that may influence very fast reactions, can also be characterized using chemical methods such as Villermaux-Dushman reaction scheme [79].

3.2.2 Pressure drop

Pressure drop is an important parameter in chemical process as it is related directly to the consuming power by the pump which is an economic concern. In HEX reactors, the wavy channels are often used to enhance heat transfer and mass transfer. However, the bends in wavy channels increases the pressure drop as well compared to straight channels. So when talking about the mass transfer and heat transfer enhancement, it is better to take the pressure drop into account for an overall evaluation factor [80].

When it comes to pressure drop, the Fanning friction factor cannot be skipped which is defined as:

$$f = \frac{\tau}{\rho\frac{u^2}{2}} \tag{I-4}$$

which is the ratio between the local shear stress (τ) and the local flow kinetic energy density. In a tube with circular cross-section of radius *r*, the shear stress can be calculated as

$$\tau = \frac{\Delta p * \pi r^2}{2\pi r L} = \frac{\Delta p r}{2L} \tag{I-5}$$

where $2\pi rL$ is the wall area, L is the length of the tube. With the two equations above, the pressure loss in a tube with circular cross-section can be calculated using the following equation. It can be extended to other cross-sectional shape using the hydraulic diameter.

$$\Delta p = f\frac{\rho u^2 L}{r} = 2f\rho u^2 \frac{L}{d_h} \quad \text{(I-6)}$$

In a tube with circular cross-section, the Fanning friction factor in fully developed laminar flow can be calculated by [81]:

$$f = \frac{16}{Re} \quad \text{(I-7)}$$

while in a tube with square cross-section, the Fanning friction factor in fully developed laminar flow can be calculated by [82]:

$$f = \frac{14.227}{Re} \quad \text{(I-8)}$$

Experimentally, the pressure drop is estimated using pressure sensors or differential pressure transmitters. Numerically, it is obtained from the resolution of Navier-Stokes equations, using the adequate models.

3.3 Thermal performances

Most of the chemical reactions depend on the temperature, highly or lightly. The temperature in the reactor can influence the reaction which furtherly affects the conversion and selectivity. Besides, for the high exothermic reactions, it is very important to remove the heat timely for safety concern. For releasing the heat generated by the reactions (or offering heat for endothermic reactions), conventional reactors are equipped with serpentines (internal or external) or double-shells where circulates the cooling fluid or hot fluid for endothermic reactions. In large reactors the heat transfer efficiency is not very good and additional external heat exchangers may be used. The idea of heat-exchange reactors is to combine the reaction and efficient heat transfer in the same place (in the reactor). So normally in HEX reactors, the temperature is better controlled, the conversion and the selectivity are higher than conventional reactors.

The miniaturization of the equipment can enhance heat transfer mainly because the specific heat exchange area (heat exchange area divided by volume A_H/V) increases by reducing the size of the equipment. The thermal characteristics of industrial HEX reactors presented in Part 2.5 are in the table below, and compared with other reactors. Heat exchanger reactors have large heat exchange capacity per volume, which allows to carry out highly exothermic chemical reactions in safe operating conditions.

Table I-1: Comparison of thermal characteristics for different types of reactors [26]

Reactors	**Micro-HEX reactor**	**Boostec SiC/Al HEX reactor**	**Chart Shimtec reactor**	**Corning advanced flow reactor**	**Tubular reactor**	**Stirred tank**
Specific area (A_H/V) $m^2.m^{-3}$	10000	2000	2000	2750	400	2,5
Heat exchange coefficient (U) $W.m^{-2}.K^{-1}$	25000	5000	1250	600	500	400
Heat exchange capacity per volume (UA_H/V) $kW.m^{-3}.K^{-1}$	250000	10000	2500	1650	200	1

For characterizing the thermal performance of the heat exchanger reactors, there are some physical quantities needed to be presented. For a heat exchanger, the heat exchange flux (q) can be evaluated by:

$$q = \dot{m} C_P \Delta T \tag{I-9}$$

where $\dot{m}$ is the mass flow rate and C_P is the specific heat of the fluid. ΔT is the difference between the inlet and the oulet temperatures of the fluid. One of the most important quantity, the overall heat exchange coefficient (U), can be calculated by:

$$U = \frac{q}{A_H \Delta T_{ml}} \tag{I-10}$$

where A_H is the heat exchange area, ΔT_{ml} is the logarithmic mean temperature difference. This overall coefficient corresponds to the inverse of a sum of thermal resistances that describes the heat transfer capacity by convection and advection of the different fluids and materials that contribute to the heat flux. The heat exchange coefficient in a fluid (h) is related to the fluid property, the velocity, etc. It is generally expressed in dimensionless form through the Nusselt number (Nu), which is defined as:

$$Nu = \frac{hd_h}{k} \quad \text{(I-11)}$$

where k is the thermal conductivity.

For straight channels, there are many correlations available in publications to calculate the Nusselt number. Here two correlations are just presented. In laminar regime (Re<2100), the Nusselt number can be calculated with Schlunder correlation [83]:

$$Nu = (3.66^3 + 1.61^3 \frac{RePrd_h}{L})^{1/3} \quad \text{(I-12)}$$

where L is the channel length, Pr is the Prandtl number defined as:

$$Pr = \frac{C_p \mu}{k} \quad \text{(I-13)}$$

The Schlunder correlation is valid when $L/d_h RePr$ is between 0.0001 and 10. In transient and turbulent regime, the Nusselt number can be calculated with Gnielinski correlations [84]:

$$Nu = \frac{hd_h}{k} = 0.012\ (Re^{0.87} - 280)\ Pr^{0.4}\ [1 + (\frac{d_h}{L})^{\frac{2}{3}}]\ (\frac{Pr}{Pr_w})^{0.11} \quad \text{(I-14)}$$

This correlation is valid for Pr between 1.5 and 500 and Re between 2300 and 10^6.

For innovative HEX reactors, correlations are not available in literature and the characterization of their thermal performances is required to allow the modelling and the scaling-up of these devices. This characterization is based on temperature measurements to calculate the heat fluxes and the temperature differences. Then the thermal characteristics like heat transfer coefficient (U and h), Nusselt number (Nu), etc. can be calculated. CFD can be used as far as the hydrodynamic and thermal models are adapted. This is a key point in millimetric channels since the transient flow regime (between laminar and fully-turbulent) is often observed in such geometry. This flow regime is complex and available models in common CFD codes can fail to represent it. Experimentally, there are many methods to measure the temperature. In terms of liquid flows, the methods often used are thermoelectric devices, platinum resistance thermometers and infrared thermography.

Thermocouples are the thermoelectric devices the most used in the research field or industry because of their low cost, simplicity, size and robustness. They can monitor temperatures between -270 °C and 3000 °C. The basis of thermocouples is the Seebeck effect: the junction between two metals generates a voltage that is a function of temperature. There are 8

standardized thermocouple types with different temperature ranges and sensitivities which are presented in Table I-2 [85]. Thermocouples provide high speed of response, however their measurements are not very accurate. They also have limited spatial resolution, e.g. some places may be difficult to reach in a fluid flow, and the probes may cause interactions with the flow (intrusive method).

Table I-2: Standardized thermocouples

Thermocouple type	**Temperature range (°C)**	**Output (µV/°C)**	**Cost**	**Stability**
T	-262 to 850	15 at -200 °C 60 at 350 °C	Low	Low
J	-196 to 700	26 at -190 °C 63 at 800°C	Low	Low
E	-268 to 800	68 at 100 °C 81 at 500 °C 77 at 900 °C	Low	Low to mid
K	-250 to 1100	40 from 250 to 1000 °C 35 at 1000 °C	Low	Low
N	0 to 1250	37 at 1000 °C	Low	Mid to high
B	100 to 1750	5 at 1000 °C	High	High
S	0 to 1500	6 from 0 to 100 °C	High	High
R	0 to 1600	10 at 1000 °C	High	High

The resistance temperature devices (RTD) are other detectors commonly used to measure the temperature. The basis is that the resistance of a conductor is related to the temperature as the motion of free electrons and of atomic lattice vibration depends on the temperature. Materials like copper, gold, nickel, platinum can be used for the construction of RTD, among which the platinum is the most used because it has a big resistivity and a linear resistance-temperature relationship compared to other metals. The platinum resistance thermometers (PRT) can monitor temperatures between -260 and 962 °C. The most common PRT type is PT100 which

has a resistance of 100 ohms at 0 °C and 138.4 ohms at 100 °C. For a PT100, a change of temperature of 1 °C will cause a 0.384 ohm change in resistance, so a small error in measurement of the resistance can cause a large error in the measurement of the temperature. There are different circuit configurations but the four-wire configuration gives the best performance and can eliminate lead wire resistance uncertainties. One problem of the PRT is self-heating, the current through the sensor causes some heating which tend to report an artificially higher temperature. Attention should be paid to minimize the current and ensure good thermal contact with its environment to reduce the measurement errors. Also, the size of the probe is relatively large and it is difficult to measure the temperature of liquid flows in millimetric channels. Finally, this method is also intrusive and the probe can create significant disturbances in the fluid flow.

Infrared thermography (IRT) is a contact-free technique for temperature measurements, based on the emission of thermal radiation of an object which depends on the temperature. In the last decades, IRT has become a powerful means of thermo-dynamic analysis to measure convective heat fluxes as well as to investigate the surface flow field behavior over complicated body shapes. Leblay et al. [86] applied IRT to measure heat transfer coefficient of water in a round tube and in a multiport-flat tube. Freund et al. [87] developed a method for the measurement of local convective heat transfer coefficient from the outside of a heat-transferring wall based on IRT. IRT has advantages like high spatial resolutions of surface temperatures and immediate response. However, IRT is limited to outside surfaces, so it is difficult to apply it to fluid flow temperature measurement as inertial effects and temperature diffusion in the outside surface significantly reduce the accuracy of the method.

At lab scale, laser‑induced fluorescence thermometry can also be used. It is based on the temperature dependence of fluorescence emission of organic dyes and allows to measure the temperature in liquid flows. During the last two decades, different approaches to implement have been developed. The simplest technique uses a single dye and a single spectral band to measure the temperature. Nakajima et al. [88] and Lemoine et al. [89] used rhodamine B to measure the temperature in turbulent heat transfer. Sakakibara et al. [90] measured the temperature in thermally stratified pipe flow with rhodamine B. Coolen et al. [91] performed temperature measurements with rhodamine B in a natural convection flow. For this technique, the problem is that any disturbance of fluorescence signal can influence the measurement of temperature since the temperature is directly deduced from the fluorescence intensity. For

example the temporal variation of laser intensity or a change of dye concentration affects significantly the measurement. The flow itself can influence the fluorescence signal as well, like in multiphase flows, the interfaces of droplets and bubbles can change light propagation.

To limit the impact of these disturbances the ratiometric technique has been developed. In this technique, two detection bands are used and the temperature can be deduced from the ratio of the fluorescence intensity of these two bands. In some studies, one dye with two bands (2 colors/1 dye) having different temperature sensitivities are utilized. Bruchhausen et al. [92] studied a one-phase flow by using the two-colors/single-dye technique with rhodamine B. Castanet et al. [93] measured the temperature field within droplets with the same technique using pyrromethene 597-C8. However, the most popular method uses two dyes with two detection bands which is called two-colors/two-dyes (2c/2d) technique. In this approach, a temperature-sensitive dye is associated with another little temperature-sensitive dye. Sakakibara and Adrian [94,95] conducted temperature measurements in a stable thermally stratified layer with the couple of dyes Rhodamine B/Rhodamine 110 and furtherly applied this technique to the measurement of temperature field in turbulent Rayleigh-Bénard convection flow. Chaze et al. [96] utilized the couple of dyes fluorescein disodium/sulforhodamine 640 and obtained single-shot images of the temperature inside droplets. In some other studies, two dyes with opposite temperature sensitivities are utilized to obtain higher sensitivities to the temperature. Sutton et al. [97] performed an improved temperature-sensitive LIF measurement in aqueous fluid flows using the couple of dyes fluorescein disodium/kiton red (also called sulforhodamine B). Behshad et al. [98] reported an in situ whole-field measurements of the temperature field in aqueous ammonium chloride solution during uni-directional solidification using the same couple of dyes.

The LIF technique for fluid temperature measurement is used less often than thermocouples or resistance thermometers use because it requires expensive and large equipment (laser, cameras, etc.). However, it is interesting for local temperature measurements in small devices because it is non-intrusive and provides immediate response which can be adapted to unsteady flows. In this thesis, the laser‑induced fluorescence thermometry with two dyes and two detection bands is developed for the temperature measurement in milli-structured heat-exchanger reactors which will be presented in Chapter IV. The two-color/two dye approach with opposite temperature sensitivities are utilized in order to have high sensitivity for the temperature measurement.

4. Conclusion

The concept of process intensification emerged 40 years ago and many technologies have been developed to intensify the process during the last two decades. These technologies can generally be divided into two parts: single unit operation intensification and intensification among different units. One method for unit operation intensification is the miniaturization of equipment which is very popular at this time, like the milli-structured and micro-structured devices. One method for intensification among different unit operations is the multifunctionality of the apparatus which has drawn great attention as well.

Several intensified reactors are then presented which are static mixers, spinning disk reactors, rotating packed bed reactors and microreactors. The intensification strategy is different among these different reactors. For static mixers, it is the immobile inserts that can redistribute the fluid in the radial direction. The spinning disk and rotating packed bed reactors use the centrifugal force to intensify the process. As for microreators, it is the miniaturization that enhances the mass transfer and heat transfer providing high surface-to-volume ratio.

The heat-exchanger (HEX) reactors are presented in more details since they are the study object of this thesis. They combine two process intensification methods: the miniaturization and the multifunctionality. Several industrial HEX reactors are presented. The hydrodynamic performance of heat exchanger reactors are discussed, in terms of flow patterns, residence time, mixing and pressure loss. The thermal performance is presented as well. Several temperature measurement methods in liquid flows are introduced with the purpose of characterizing the thermal performance. The laser-induced fluorescence thermometry is presented in the last part which is utilized in this thesis to measure the local temperature in HEX reactors. This work concentrates on the heat transfer performance of millimetric zigzag channels which can be used for the design of compact HEX reactors. Experimental and numerical methods for the characterization are presented in the following Chapters.

Chapter II: Experimental method for the heat transfer study

In this chapter, the experimental method is utilized to study the heat transfer performance of a compact heat-exchanger reactor which is designed by the Laboratoire de Génie Chimique (LGC). It consists of a plate heat exchanger where the process fluid (the reaction may occur) circulates in a zigzag millimetric channel engraved in the plate. In the present work, several prototypes have been built to characterize the heat transfer coefficients in different millimetric channels. Two kinds of channel configuration are investigated which are zigzag channel and straight channel. For zigzag channels, the influence of fluid properties on heat transfer is also studied by working with water and a more viscous fluid (glycerol solution). The overall heat transfer coefficient of the heat exchanger reactor prototypes with zigzag channels and that with straight channels is characterized experimentally by measuring the inlet and outlet temperature of the two exchange fluids. The heat transfer coefficient in zigzag channels is then deduced and a correlation for Nusselt number estimated in zigzag channels is proposed.

1. Materials and methods

1.1 Experimental prototypes

In this work, six prototypes have been designed and constructed in LGC for the study of heat transfer in compact heat exchanger reactors. They consist of three plates: a plate made of aluminum sandwiched between two plates where channels are engraved for fluid circulation (Figure II-1). These two plates will be differentiated as “process plate” and “utility plate” according to the design of the channel engraved. They are pasted to the aluminum plate using double-sided adhesives cut to fit the channel designs. The adhesives have been realized by Atelier Graphique Saunière (France). The aluminum plate is of 1 mm thickness with a high thermal conductivity (k = 237 $W.m^{-1}.K^{-1}$) and its thermal resistance is very low ($e/k = 4.2 \times 10^{-6}$ $m^2.K.W^{-1}$). Its surface has been anodized to obtain the black color which can allow the safe use of a laser for the temperature field measurement by LIF, this will be presented in Chapter IV. The process plate and utility plate are made of PolyMethylMethAcrylate (PMMA) with 10 mm thickness. This hard polymeric material has been chosen because it is cheap and can be easily engraved by milling. It is transparent which is convenient for flow observation. The transparence is also necessary for the temperature field measurement by LIF presented in chapter IV. Moreover, its thermal conductivity is very low which can largely avoid heat loss (k = 0.19 $W\ m^{-1}\ K^{-1}$, e/k = 0.05 $m^2.K.W^{-1}$). Finally PMMA presents a linear coefficient of thermal

expansion with $\alpha = 7\times10^{-5}$ K^{-1}. Using Eq. II-1, less than 0.3% of dimensional change is estimated when working between 20°C and 60°C which is the temperatures range during the experiments. Therefore geometry changes due to temperature can be neglected.

$$\frac{\Delta l}{l} = \alpha \Delta T \qquad \text{(II-1)}$$

l is the dimension, T is the temperature. One prototype with a zigzag channel engraved in the process plate is presented in Figure II-1.

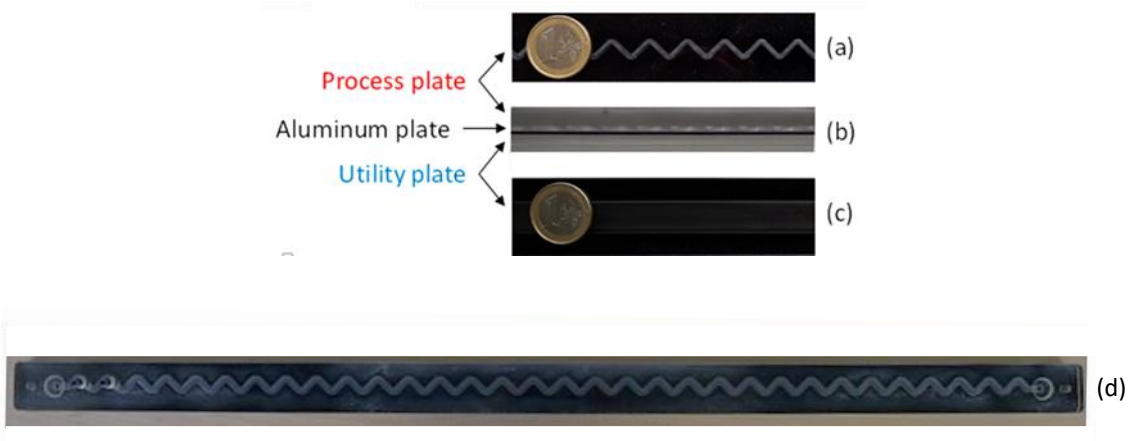

Figure II-1: Prototype composed of a PMMA process plate with a zigzag channel engraved (a) and a PMMA utility plate with a rectangular straight channel engraved (c) separated by an aluminum plate (middle in (b)). Top view of total length with of 65 cm long and 3 cm width (d).

In this work, two kinds of channel configuration are investigated (engraved in the process plate): straight channels (as references) and zigzag channels with three different square cross-sections (d_h = 2 mm, 3 mm, 4 mm) and a total straight length of nearly 0.6 m. The zigzag channels consist of periodic straight sections and bends as shown in Figure II-2, where the ratio of the mean curvature radius of the bends (at the channel center) to the hydraulic diameter R_c/d_h is kept constant, which gives the curvature radius (R_c) of 1.5 mm, 2.25 mm and 3 mm respectively. The straight section length between two bends is fixed at 7 mm, the angle (θ) between two straight sections is kept at 90°. This geometry pattern has been used to build compact heat exchangers-reactors designed by LGC, Boostec (France) and the Commissariat à l'Energie Atomique et aux Energies Alternatives (CEA, France). Such devices made of silicon carbide or stainless steel have been successfully used to carry out highly exothermic reactions [99–101].

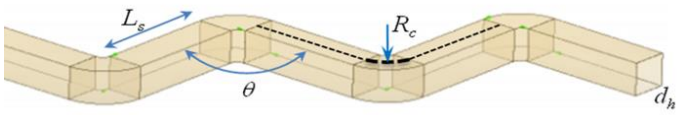

Figure II-2: Schematic of the zigzag channel: d_h = 2 - 4 mm, L_s = 7 mm, R_c = 1.5 - 3 mm, θ = 90°

In the utility plate, a straight channel with a cross-section of 12×6 mm² is engraved. Its geometry is unique for all the prototypes, whatever the process channel design is, and has been chosen so that:

- its width (12 mm) and length are slightly higher than the total width and length of all the zigzag channels in process plate. The process channel pattern that presents the largest width, 10.7 mm, is obtained for the zigzag channel of 4 mm width. The utility and process channels are face to face and centered in the PMMA plates. This way, the utility channel sufficiently covers the zigzag channel or straight channel in the process plate both in the flow direction and radial direction (Figure II-3).
- its depth (6 mm) allows a flowrate up to ten times higher than the process fluid flowrate for water. With this cross-section, the Reynolds number of utility fluid is higher than 10 000 in the experiment, which is in turbulent flow regime. Therefore, heat transfer is not mainly limited by the utility side and common Nusselt number correlations for straight channel can be used to estimate the heat transfer coefficient.

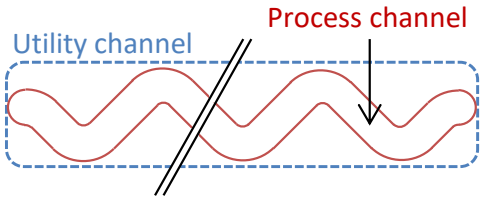

Figure II-3: Illustration of the prototype top view for the zigzag process channel of 4 mm width.

1.2 Experimental setup

The experimental setup is shown in Figure II-4. For each prototype, the process channel is connected to a gear pump (0 - 100 $L.h^{-1}$) and the utility channel is connected to a centrifugal pump (0 - 1000 $L.h^{-1}$), with two different mass flowmeters. 4 thermocouples are used to measure the inlet and outlet temperature of these two channels. The temperature measurement are

recorded by an acquisition system based on LabVIEW software (National Instruments, US) which can also control the gear pump easily.

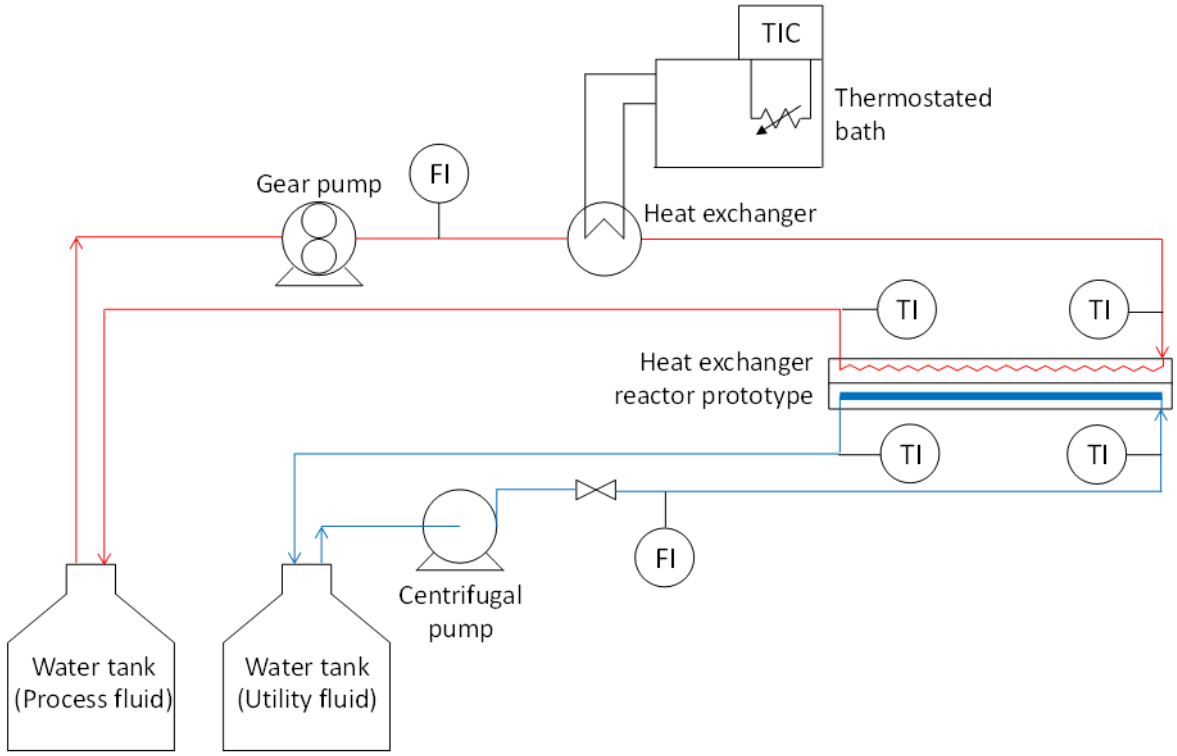

Figure II-4: Experimental set-up for the characterization of heat transfer coefficients

In the experiment, hot fluid at about 50 °C (60 °C for small flowrates) is introduced in the process channel of the prototype. Hot fluid is produced by heating the fluid at ambient temperature with a heat exchanger where the hot exchange water is heated by a thermostatic bath. In the prototype, it is cooled by cold water at ambient temperature introduced in the utility channel. The two fluids circulate co-currently, the inlet and outlet temperature of these two fluids are measured. The prototype is surrounded by an insulation foam during the experiment in order to decrease the thermal loss. In the process plate, the range of flowrate varies with the channel cross-section and reaches a maximum of 60 $L.h^{-1}$. Two process fluids are studied during the experiment: water and glycerol solution (mixed with water). Glycerol is a colorless, odorless, viscous liquid which does not deform the PMMA. The glycerol solution used is 74% in mass fraction. The physicochemical properties of water and glycerol solution at 20 °C are presented in the following table. It presents a Newtonian rheological behavior. In the utility plate, three flowrates (Q_u) are studied which are 300 $L.h^{-1}$, 400 $L.h^{-1}$ and 500 $L.h^{-1}$.

Table II-1: Physical properties of water and 74% glycerol solution at 20 °C

Process fluids	ρ (kg.m^{-3})	C_p (J.kg^{-1}.K^{-1})	μ (mPa.s)	k (W.m^{-1}K^{-1})	Pr
Water	1000	4180	1	0.6	7
Glycerol solution	1192	2842	32.6	0.337	286

The flowrate in process channel and utility channel for three prototypes is presented in Table II-2. The corresponding velocity and Reynolds number are also presented.

Table II-2: Flowrate in process channel and utility channel for three prototypes with corresponding velocity and Reynolds number

	Process channel			**Utility channel**
	d_h = 2 mm	d_h = 3 mm	d_h = 4 mm	d_h = 8 mm
Water	Q_p = 1.5 – 15 L.h^{-1} u_p = 0.1 – 1 m.s^{-1} Re_p = 280 – 4000	Q_p = 2.8 – 34 L.h^{-1} u_p = 0.09 – 1 m.s^{-1} Re_p = 430 – 6200	Q_p = 5 – 60 L.h^{-1} u_p = 0.09 – 1 m.s^{-1} Re_p = 640 – 7200	Q_u = 300 – 500 L.h^{-1} u_u = 1.1 – 1.9 m.s^{-1} Re_u = 10^4 – 2×10^4
Glycerol solution	Q_p = 1.2 – 11 L.h^{-1} u_p = 0.08 – 0.7 m.s^{-1} Re_p = 20 – 350	Q_p = 2.4 – 28 L.h^{-1} u_p = 0.07 – 0.9 m.s^{-1} Re_p = 25 – 420	Q_p = 2.4 – 31 L.h^{-1} u_p = 0.04 – 0.4 m.s^{-1} Re_p = 15 – 220	

1.3 Method for heat transfer coefficient calculation

As the utility fluid flowrate is around ten times higher than the process fluid flowrate, the difference between inlet and outlet temperature of process fluid is ten times bigger than that of utility fluid. Therefore, the process fluid is taken into consideration for the calculation of heat fluxes (heat loss and heat exchanged with the utility fluid). From the temperature difference (ΔT_p) of the process fluid, the heat flux exchanged between the two fluids (q) can be calculated using equation II-2. The thermal losses (q_l) have been previously estimated by introducing just the process fluid (equation II-2 with q = 0), with no flow in the utility channel.

$$q = \dot{m}_p C_{P,p} \Delta T_p - q_l \quad \text{(II-2)}$$

Where $\dot{m}_p$ is the mass flow rate and $C_{P,p}$ is the specific heat of the process fluid. The overall heat transfer coefficient (U) of the prototype can be calculated with the equation I-10, with

$$\Delta T_{ml} = \frac{(T_{p,in} - T_{u,in}) - (T_{p,out} - T_{u,out})}{ln\frac{(T_{p,in} - T_{u,in})}{(T_{p,out} - T_{u,out})}} \quad \text{(II-3)}$$

For the sandwiched prototype, the overall conductance is:

$$\frac{1}{UA_H} = \frac{1}{h_p A_{H,p}} + \frac{e_{Al}}{k_{Al} A_H} + \frac{1}{h_u A_{H,u}} \quad \text{(II-4)}$$

where h_p and h_u are the convection heat transfer coefficient of the process fluid and utility fluid, $A_{H,p}$ and $A_{H,u}$ are the heat transfer areas in the process plate and the utility plate. They are calculated by:

$$A_{H,p} = w_p L_p \quad \text{(II-5)}$$

$$A_{H,u} = w_u L_u \quad \text{(II-6)}$$

where w_p, w_u and L_p, L_u are the channel width and channel length of process channel and utility channel. For the zigzag channel, channel length corresponds to the developed length of the geometry and it is longer than the channel length of utility. A_H is considered equal to $A_{H,p}$ in this work. The heat transfer coefficient h_u of the utility fluid ($Re > 10^4$ in the experiment) can be deduced from the correlation of Nusselt proposed by Gnielinski, reminded below:

$$Nu = \frac{hd_h}{k} = 0.012\ (Re^{0.87} - 280)\ Pr^{0.4}\ [1 + (\frac{d_h}{L})^{\frac{2}{3}}]\ (\frac{Pr}{Pr_w})^{0.11} \quad \text{(II-7)}$$

Pr_u is close to 4 in the experiment. Assuming the temperature of the wall is that of the process fluid (it is lower in fact), Pr_w is estimated to be around 6. So in the calculation, it is assumed that $(\frac{Pr_u}{Pr_w})^{0.11} = 1$.

the heat transfer coefficient of the process fluid h_p can then be deduced from equation II-4. The Nusselt number Nu_p can be furtherly obtained with $Nu = hd_h/k$.

The physicochemical properties (density ρ, specific heat capacity C_p, Prandtl number Pr) of water at different temperatures can be obtained by the following equations [102]:

$$\rho[\mathrm{kg.m^{-3}}] = 330 + 5.92 \times T - 1.63 \times 10^{-2} T^2 + 1.33 \times 10^{-5} T^3 \quad \text{(II-8)}$$

$$C_p[\mathrm{J.kg^{-1}.K^{-1}}] = 10^4 - 5.14 \times 10^2 T + 1.49 \times T^2 - 1.43 \times 10^{-3} T^3 \quad \text{(II-9)}$$

$$Pr = 900 - 7.79T + 2.26 \times 10^{-2} T^2 - 2.2 \times 10^{-5} T^3 \quad \text{(II-10)}$$

$$k[\mathrm{W.m^{-1}.K^{-1}}] = -12.2 + 1.18 \times 10^{-1} T - 3.66 \times 10^{-4} T^2 + 3.81 \times 10^{-7} T^3 \quad \text{(II-11)}$$

The viscosity can be calculated with the three equations above (II-9, II-10, II-11):

$$\mu = \frac{Prk}{C_p} \quad \text{(II-12)}$$

The physicochemical properties of the water-glycerol solution as a function of temperature are obtained by different methods. The density and viscosity are measured at the LGC (presented in Appendix A). The density is measured by a density meter (Anton Paar, DMA 38), the viscosity is measured by Kinexus ultra+ rheometer (Malvern Instruments). The heat capacity of the mixture is calculated by the heat capacity of each component multiplying its mass fraction. The heat capacity of glycerol at different temperature can be calculated by [103] :

$$C_P = 988.0 + 4.71T \quad \text{(II-13)}$$

The thermal conductivity of glycerol-water mixture between 20 °C and 60 °C varies little with the temperature with the value of around 0.337 $W.m^{-1}.K^{-1}$ [104].

For the calculation of all physicochemical properties, the mean temperature is considered which is the average value between inlet and outlet temperatures of the fluid.

The calculation of one experimental case in the prototype with the zigzag channel of 4 mm width in process plate is presented here. The flowrates of process fluid and utility fluid are 10.2 $L.h^{-1}$ and 300 $L.h^{-1}$, the inlet and outlet temperatures of the process fluid and the utility fluid are measured at 59.1 °C ($T_{p,in}$), 45.2 °C ($T_{p,out}$), 36.6 °C ($T_{u,in}$) and 37.6 °C ($T_{u,out}$) respectively. The inlet temperature of the utility fluid is 36.6 °C, higher than ambient temperature, because the utility fluid circulates in closed loop and is heated all the time during the experiment, so does the process fluid. The heat exchange flux stabilized after nearly one hour and half. The zigzag channel length is 0.747 m, the utility channel length is 0.588 m. The thermal loss has been previously estimated by just introducing the process fluid and measuring the inlet and outlet temperatures (58.8 °C and 58 °C respectively). With all these data, the overall heat transfer coefficient *U*, the heat transfer coefficient h_u and the Nusselt number Nu_p of the process fluid can be calculated.

The heat loss in this case is:

$q_l = \dot{m}_p C_{P,p} \Delta T_p$= 10.2÷ 3600 ×4184×(58.8-58) = 9 W

The heat exchange flux between the two fluids is:

$q = \dot{m}_p C_{P,p} \Delta T_p - q_l$ = 10.2÷ 3600 ×4184×(59.1-45.2) - 9 = 156 W

The mean logarithmic temperature difference ΔT_{ml} is:

ΔT_{ml} = [(59.1-36.6) - (45.2-37.6)] ÷ ln[(59.1-36.6) ÷ (45.2-37.6)] = 13.7 °C

The overall heat transfer coefficient *U* of the prototype is:

$U = \frac{q}{A_H \Delta T_{ml}}$ = 156 ÷ (0.004×0.747) ÷13.7 = 3796 W.m^{-2}.K^{-1}

The Nusselt number of utility fluid is calculated by the Gnielinski correlation:

$$Nu_u = 0.012 \left(Re_u{}^{0.87} - 280\right) Pr_u{}^{0.4} \left[1 + \left(\frac{d_{h_u}}{L_u}\right)^{\frac{2}{3}}\right] \left(\frac{Pr_u}{Pr_w}\right)^{0.11}$$

= 0.012×(13600$^{0.87}$-280)×4.5$^{0.4}$× [1 + (0.008 ÷ 0.588)$^{2/3}$] ×1 = 85.2

The heat transfer coefficient of utility fluid h_u then is:

$h_u = \frac{Nu_u k_u}{d_{h,u}}$ = 85.2×0.622÷0.008 = 6624 W.m^{-2}.K^{-1}

From equation II-4, the heat transfer coefficient of process fluid h_p is:

$$h_p = 1 \div \left[A_{H,p} \left(\frac{1}{U A_H} - \frac{e_{Al}}{k_{Al} A_H} - \frac{1}{h_u A_{H,u}}\right)\right]$$

$= 1 \div \left(\frac{1}{U} - \frac{e_{Al}}{k_{Al}} - \frac{A_{H,p}}{h_u A_{H,u}}\right)$ ($A_{H,p} = A_H$, as considered)

= 1 ÷ [(1÷3796 – 0.001÷237 – (0.004×0.747) ÷6624÷(0.012×0.588)] = 5121 W.m^{-2}.K^{-1}

The Nusselt number is then:

$Nu_p = \frac{h_p d_{h,p}}{k_p}$ = 5121×0.004÷6.3 = 32.3

The same calculation is done for six prototypes with different operating conditions.

2. Heat transfer performance of prototypes (zigzag and straight channels)

2.1 Overall heat transfer coefficient

The overall heat transfer coefficient *U* as a function of process fluid flowrate (water) at different utility fluid flowrates is presented in Figure II-5. In Figure II-5 (a), *U* increases with increasing flowrate in zigzag channels. It seems that the curves tend to asymptotic values, typical of the fact that the thermal resistance of the process side becomes negligible for high process flowrates. The asymptotic value can be obtained by the simplification of equation II-4 :

$$\lim_{Q_p \to \infty} U = \frac{1}{\frac{e_{Al}}{k_{Al}} + \frac{A_H}{h_u A_{H,u}}} \tag{II-14}$$

The same trends can be seen in the straight channels as shown in Figure II-5 (b). However, the increase to the asymptotic value is less obvious in the range of flowrate studied because the process side thermal resistance is higher in the straight channel than in the zigzag channel under the same flow condition. Indeed, by comparing both figures, it is observed that *U* in the prototypes with zigzag channels is around 2 times larger than that with straight channels for the same flowrates. It indicates that the presence of bends in the zigzag channel can enhance the heat transfer compared with straight channels, in particular at low flowrates, where the overall heat transfer coefficient can even be 4 times higher in zigzag channels than in straight channels. Among the different channel cross-sections, *U* increases with the decrease of cross-section width both in zigzag channels and in straight channels. As for the influence of process flowrate to *U*, *U* increases with increasing utility flowrate, although it has little influence at low process flowrate (heat transfer limited by the process side).

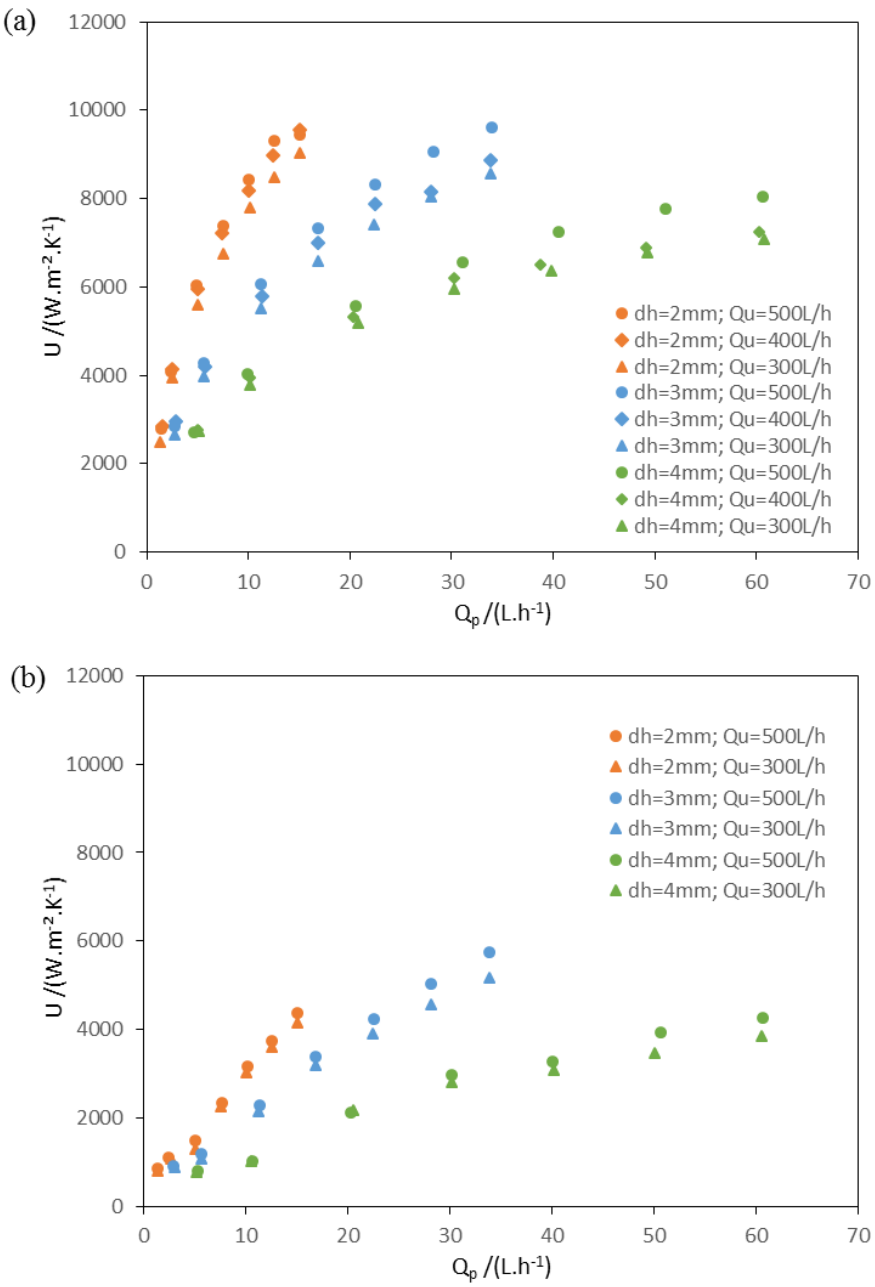

Figure II-5: Overall heat transfer coefficient as a function of process fluid flowrate (water) in (a) zigzag channels and (b) straight channels at three utility fluid flowrates. The legend gives the hydraulic diameter of process channel (d_h) and the utility fluid flowrate (Q_u).

2.2 Heat transfer coefficient in zigzag channels

To further illustrate the influence of the bends in zigzag channel to the heat transfer, the heat transfer coefficient of process fluid (water) h_p in zigzag channel and straight channel is compared. h_p in zigzag channels as a function of Reynolds numbers at different utility flowrates

is presented in Figure II-6. As expected, h_p is independent of the utility flowrate. It increases with increasing Reynolds number for the same channel. As for the influence of channel geometry, h_p increases with the decrease of cross-section length at same Reynolds number.

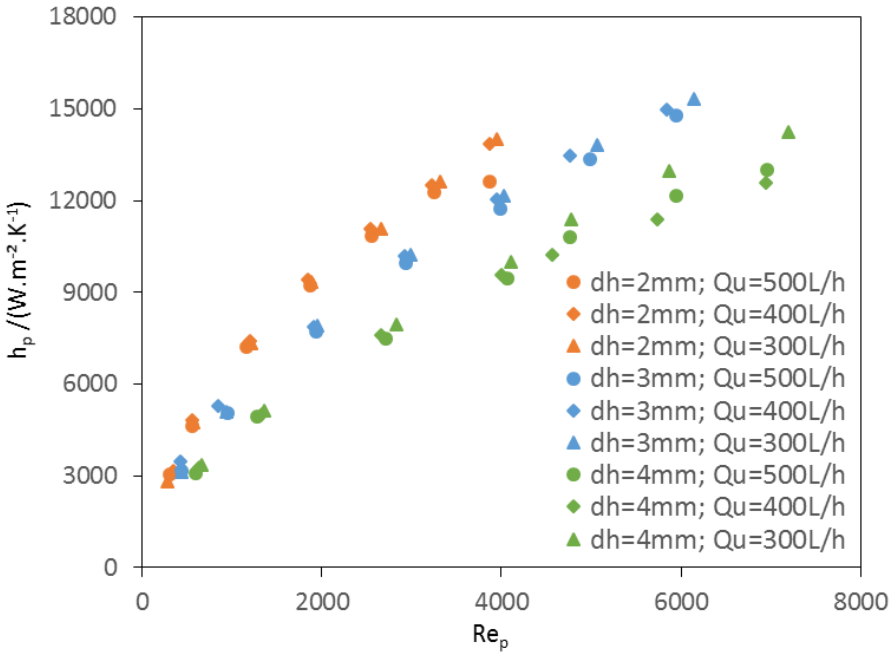

Figure II-6: Heat transfer coefficient of process fluid (water) as a function of Reynolds number in zigzag channels. The legend gives the hydraulic diameter of process channel (d_h) and the utility fluid flowrate (Q_u).

To further show the heat transfer enhancement in zigzag channel compared to straight channels, the ratio $h_{p,zigzag}/h_{p,straight}$ is calculated and presented in Figure II-7. In Figure II-7, $h_{p,zigzag}/h_{p,straight}$ decreases with increasing Reynolds number. It should approach 1 at infinite Reynolds number since in turbulent flow the influence of the bends to heat transfer decreases. $h_{p,zigzag}/h_{p,straight}$ is between 2 and 5 for the Reynolds number range studied, the maximum value is at the Reynolds number nearly 1000. h_p in zigzag channel is much larger than that in straight channel. That is because the presence of the bends can generate secondary flow and decrease the thermal boundary layer thickness. The influence of bends in zigzag channel on the flow and heat transfer is studied in details in Chapter III with a numeric method based on Computational Fluid Dynamics (CFD) simulation.

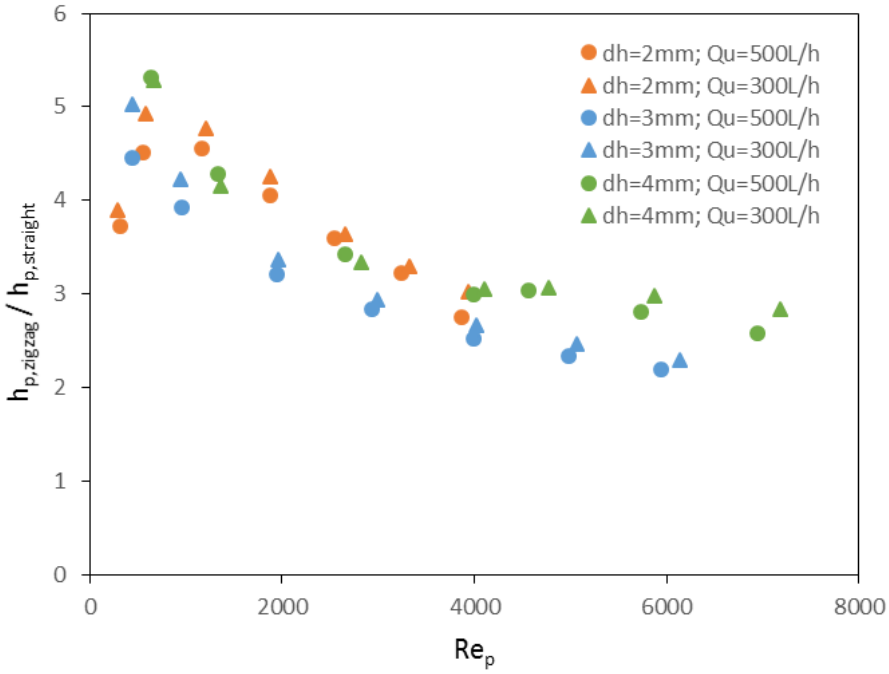

Figure II-7: $h_{p,zigzag}/h_{p,straight}$ as a function of Reynolds number at two utility flowrates. The legend gives the hydraulic diameter of process channel (d_h) and the utility fluid flowrate (Q_u).

3. Influence of fluid properties on heat transfer in prototypes with zigzag channels

3.1 Overall heat transfer coefficient

The overall heat transfer coefficient U as a function of process fluid flowrate and Reynolds number for two fluids (water and glycerol solution) in the prototypes with zigzag channels is presented in Figure II-8. In Figure II-8 (a), U with water as process fluid is much higher than that with glycerol solution at the same flowrate, generally 3 times. That is because the glycerol solution is much more viscous than water, resulting in a very small Reynolds number for the same flowrate (as shown in Figure II-8 (b)), which does not favor the heat transfer. In terms of channel size influence, U increases with the decreasing channel cross-section length for both fluids. In Figure II-8 (b), the evolution of U with glycerol solution as a function of Reynolds number almost follows that with water, except for the channel cross-section of 2 mm, U is a little larger than that with water at same Reynolds number.

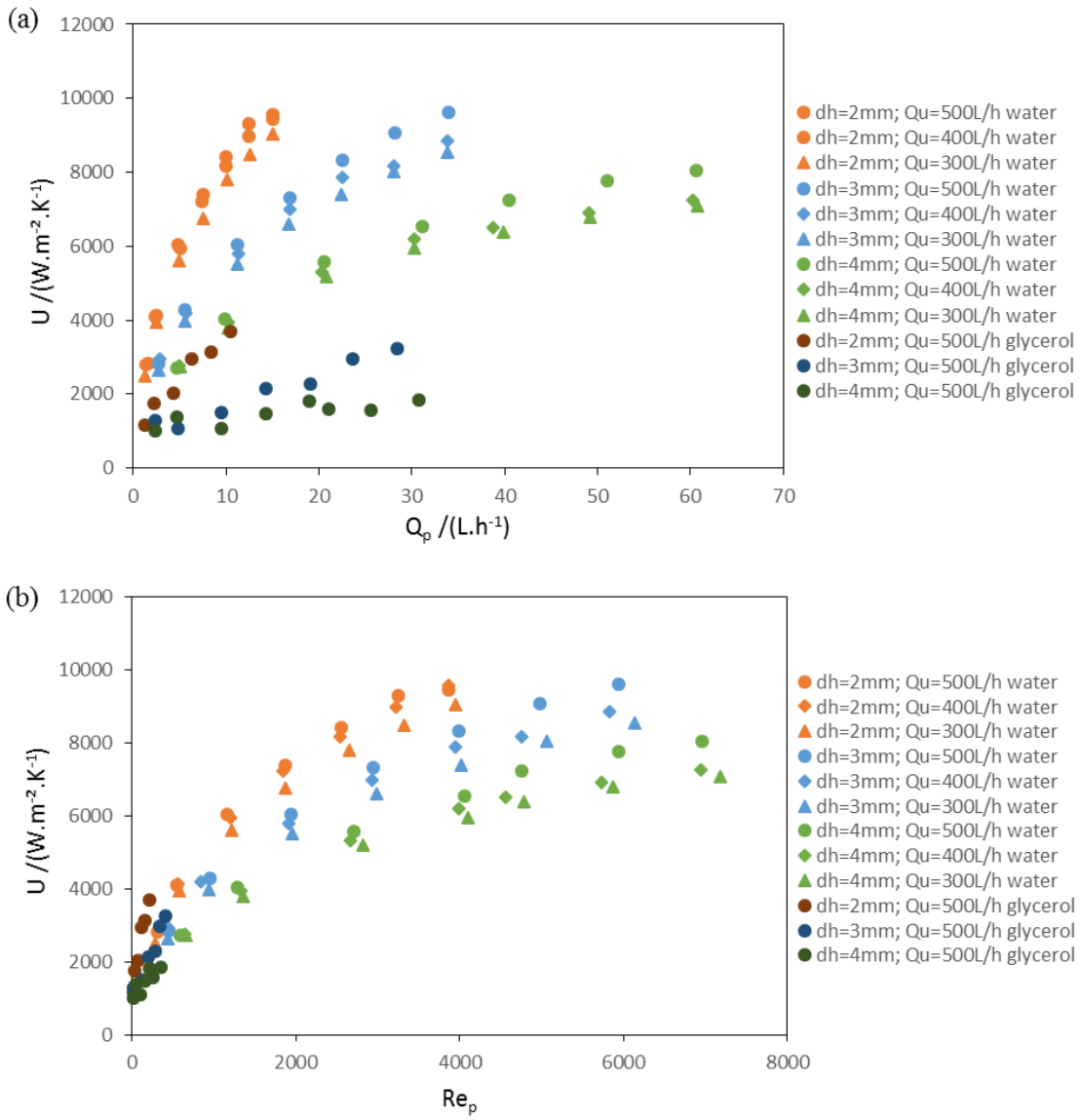

Figure II-8: Overall heat transfer coefficient for two process fluids in prototype with zigzag channels as a function of (a) flowrate, (b) Reynolds number. The legend gives the hydraulic diameter of process channel (d_h), the utility fluid flowrate (Q_u) and the process fluid. Glycerol represents the glycerol solution of 74% in mass fraction.

3.2 Heat transfer coefficient in zigzag channels

The heat transfer coefficient in zigzag channel as a function of Reynolds number for two fluids is presented in Figure II-9. The similar trend can be seen compared to overall heat transfer coefficient (Figure II-8 (b)), that is the evolution of h_p with glycerol solution generally follows that with water. For the same Reynolds number, when the channel cross-section decreases, h_p increases for both fluids.

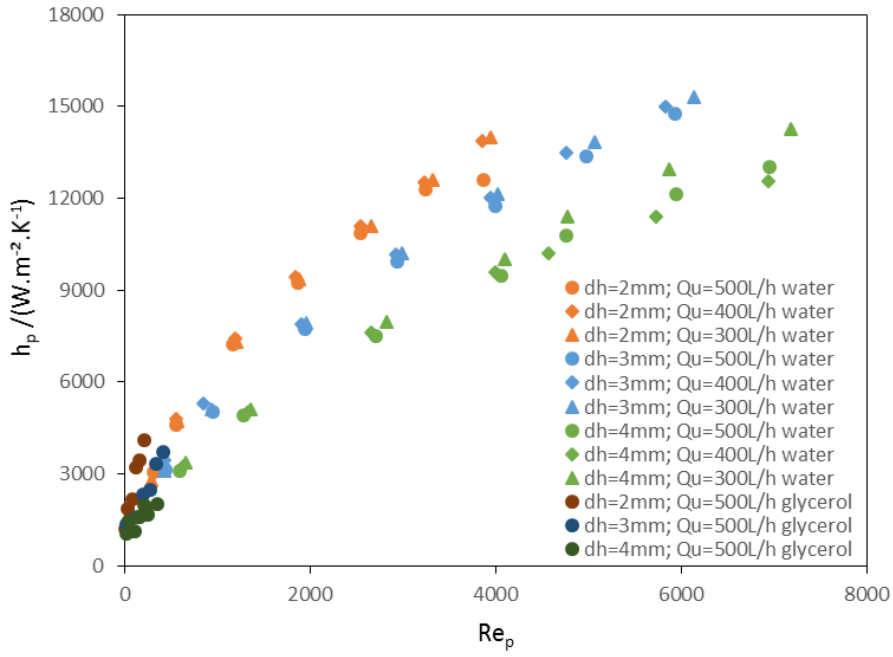

Figure II-9: Heat transfer coefficient in zigzag channels as a function of Reynolds number. The legend gives the hydraulic diameter of process channel (d_h), the utility fluid flowrate (Q_u) and the process fluid. Glycerol represents the glycerol solution of 74% in mass fraction.

3.3 Global heat transfer performances of HEX reactors with millimetric channels

The experimental results in the different prototypes are analyzed in terms of common performance criteria provided in Table I-1 to compare different technologies, they are the ratio of the heat exchange area to the volume and the heat exchange capacity per volume unit. A typical configuration of plate heat exchanger reactor is considered for the following comparison: the process plate (zigzag or straight) is surrounded by two utility plates and separated by two aluminum plates. In this case, the heat exchange area is two times of that discussed before (with two heat exchange walls in fact). The thermal characteristic result for such devices with two utility plates is presented in Table II-3. From this table, it can be clearly seen that the heat transfer performance of zigzag configuration is much better than that of straight configuration as process channel. As for the influence of channel cross-section length, the heat transfer coefficient range is similar among the three channels for both configurations. The intensification effect by size reduction is due to the increase of the ratio A_H/V in fact. The thermal performances with zigzag configuration as process channel are of the same order of magnitude compared with industrial compact heat exchangers reactors, with overall heat exchange capacity per unit volume between 1 500 and 10 000 kW.m^{-3}.K^{-1} (as shown in Table I-1).

Table II-3: Thermal characteristics of HEX reactors with millimetric channels

	Zigzag channels			Straight channels		
d_h (mm)	2	3	4	2	3	4
Specific area A_H/V ($m^2.m^{-3}$)	1000	667	500	1000	667	500
Heat exchange coefficient h_P (*) ($W.m^{-2}.K^{-1}$)	2800 – 14000	3100 – 15500	3100 – 14300	800 – 4900	900 – 6800	800 – 5000
Heat exchange capacity per volume $h_P A_H/V$ ($kW.m^{-3}.K^{-1}$)	2800 – 14000	2060 – 10300	1 550 – 7150	800 – 4900	600 – 4530	400 – 2500
Overall heat exchange coefficient U (**) ($W.m^{-2}.K^{-1}$)	2 500 – 9000	2600 – 8800	2 700 – 7100	800 – 4200	900 – 5200	780 – 3900
Overall heat exchange capacity per volume UA_H/V ($kW.m^{-3}.K^{-1}$)	2500 – 9000	1700 – 5900	1300 – 3600	800 – 4200	600 – 3470	390 – 2000

(*) process fluid is water, velocity range is 0.1 – 1 $m.s^{-1}$

(**) flowrate is 300 $L.h^{-1}$ in each plate with two utility plates, 2 aluminum plates with thickness of 1 mm

4. Dimensionless correlation for heat transfer coefficient in zigzag channels

Here the dimensionless quantity Nusselt number is presented and a correlation for its estimation is proposed since one important objective of this work is to establish correlations for the scale-up of HEX reactors. With the heat transfer coefficient h_p, the Nusselt number of process fluid Nu_p in zigzag channel is calculated and presented in Figure II-10. Nu_p increases with increasing Reynolds numbers for both fluids in the three channels. When the cross-section length increases, Nu_p with water increases moderately at same Reynolds number. The increase between the cross-section of 3 mm and 4 mm is less significant than that between the cross-section of 3 mm and

2 mm for Nu_p with water. The influence of channel cross-section length on Nu_p with glycerol solution is not so evident.

Therefore, the hydraulic diameter must be taken into account for Nusselt number correlation, in addition to the Reynolds number. Since the ratio (d_h/R_c) is constant in the prototypes studied, so it is not taken into consideration in Nusselt number correlation. Although this ratio is usually used to characterize Dean number (*De*) in fluid hydrodynamics for the analysis of flow and heat transfer in curved channels, *De* is expressed as follows:

$$De = Re\sqrt{\frac{d_h}{R_c}} \tag{II-15}$$

Instead, the ratio of hydraulic diameter to the straight section length between bends (d_h/L_s) is considered in the Nusselt number correlation. It varies from 0.28 to 0.57 for the geometries studied. The influence of this ratio on the flow and heat transfer in zigzag channels will be discussed in detail in Chapter III with the numeric method based on CFD simulation.

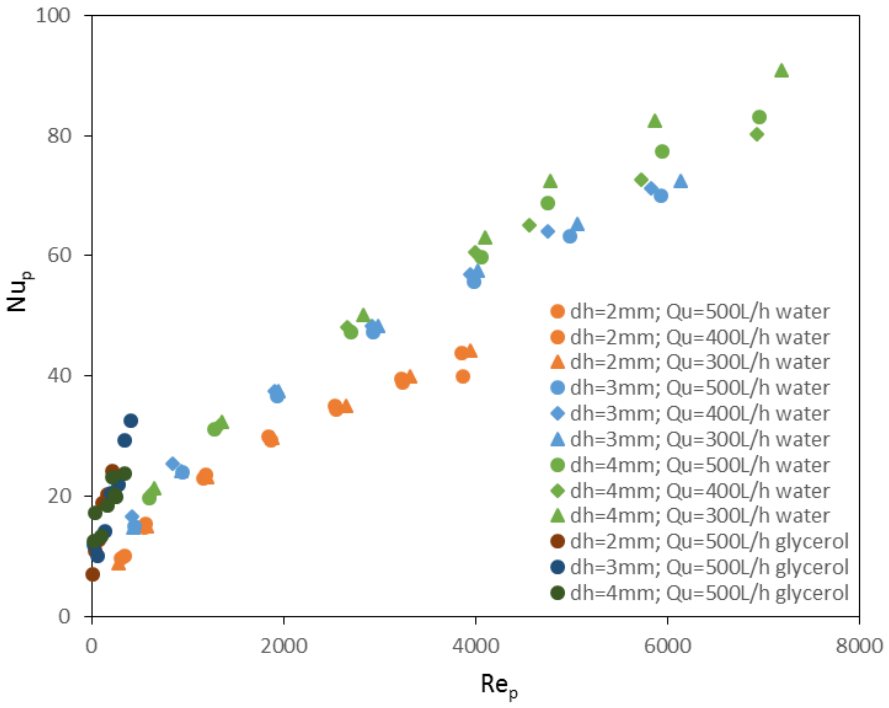

Figure II-10: Nusselt number as a function of Reynolds number in zigzag channels. The legend gives the hydraulic diameter of process channel (d_h), the utility fluid flowrate (Q_u) and the process fluid. Glycerol represents the glycerol solution of 74% in mass fraction.

Finally, regarding the influence of fluid property, Nu_p with glycerol solution is larger than that with water for the same channel and same Reynolds number. It should also be taken into account in Nusselt number correlation, which is often presented through Prandtl number (Pr).

Concerning these influences presented above: channel geometry (d_h/L_s), Reynolds number (Re) and fluid property (Pr), a correlation for Nusselt number can be established with the experimental data, using a parametric identification method which minimizes the relative error between the experimental values and the values calculated by the correlation. It is presented as:

$$Nu_p = 0.2(Re^{0.67} + 8.9)Pr^{0.3}(\frac{d_h}{L_s})^{0.4} \quad \text{(II-16)}$$

This correlation is similar to the simplified Gnielinski correlation with straight tube for transient and turbulent flow (equation II-7). $(Re^{0.67} + 8.9)$ tends to be equal to $(Re^{0.67})$ for high Reynolds number. Therefore the proposed correlation formulation tends to those generally proposed for turbulent flow regime in straight tubes (Dittus-Boëlter and McAdams correlations). Comparison has been made between Nu_p calculated with the correlation and experimental values, as shown in Figure II-11. In this figure, all data of Nu_p with water fall in the 20% error. There are several points for glycerol solution off the 20% error lines, maybe due to the experimental errors, since it is much more viscous and the flowrate is smaller, it takes more time to achieve the heat transfer equilibrium. Generally, the result shows a good agreement between the experimental data and the values calculated by the proposed correlation, with an average error of 8% and a maximal error of 44.6%.

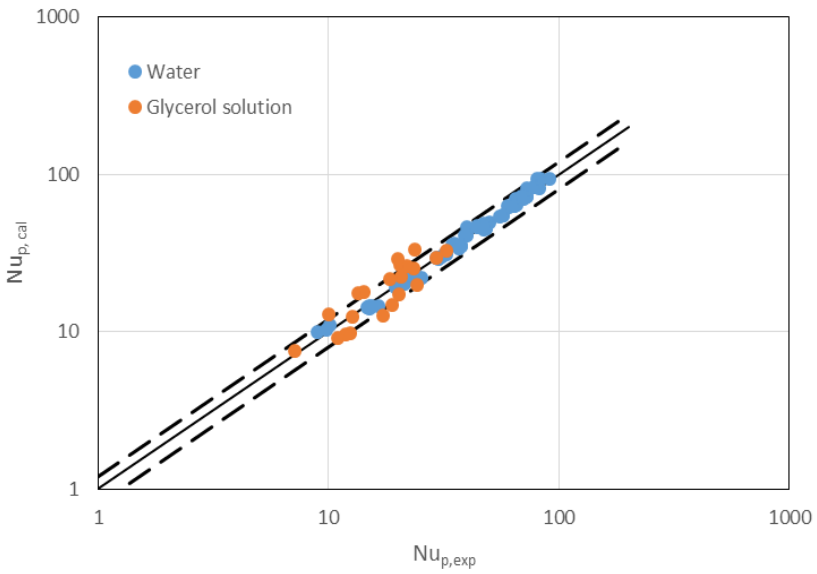

Figure II-11: Comparison between experimental Nusselt number and that calculated by the correlation in zigzag channels, dashed lines represent 20% error.

5. Conclusion

In this chapter, the heat transfer performance of compact heat exchanger reactor prototypes are experimentally characterized, in terms of overall heat transfer coefficient and heat transfer coefficient of the process side. The Reynolds number studied ranges from 16 to 7 500, covering laminar regime and transient regime. The Nusselt number is furtherly calculated and a correlation is proposed with the experimental data which should be very useful for the scale-up of HEX reactors.

For the HEX reactor prototypes, two kinds of process channel configuration are investigated: straight channels and zigzag channels with 3 different square cross-sections (d_h = 2mm, 3mm, 4 mm). The zigzag channels consist of periodic bends and straight sections. With water as process fluid, it is found that the heat transfer coefficient in zigzag channel is much larger than that in straight channel, with a ratio between 2 and 5 in the range of Reynolds number studied, demonstrating the heat transfer enhancement of zigzag channels compared with straight channels.

In order to study the influence of fluid property on the heat transfer in zigzag channels, another more viscous fluid is used in this work: a glycerol solution with a mass fraction of 74%. It presents a viscosity around 30 times higher than water at 20 °C. Its Reynolds number ranges

from 16 to 415 in the experiment, which is totally in laminar regime. It is found that the evolution of heat transfer coefficient with glycerol solution as a function of Reynolds number is similar to that with water.

A correlation of Nusselt number in zigzag channels is then proposed with the consideration of fluid properties (*Pr*), channel geometries (d_h/L_s), and fluid flowrates (*Re*). This correlation does not fit very well with the experimental data of glycerol solution compared with water, maybe due to experimental errors, since it takes more time to achieve the thermal equilibrium. Concerning the influence of channel geometry on Nusselt number, it is found that the ratio of channel hydraulic diameter divided by straight section length between two bends ($\frac{d_h}{L_s}$) plays an important role. In order to furtherly study this influence ($\frac{d_h}{L_s}$) on the heat transfer, a numerical method based on CFD simulation is then used, which is presented in the next chapter. It has the advantages like simple modification of the channel geometry, access to local information (velocity and temperature fields) in the channel. Numerical method is more efficient, since experimentally for changing this ratio ($\frac{d_h}{L_s}$), we need to construct many prototypes which takes time and is more expensive.

Chapter III: Numerical method for heat transfer study

In Chapter II, we characterized experimentally overall heat transfer coefficient and heat transfer coefficient of process fluid in 6 prototypes with zigzag channels as well as with straight channels (d_h = 2, 3, 4 mm). A correlation of Nusselt number in zigzag channels was proposed for two process fluids (water, *Pr*~4, and glycerol solution, *Pr*~200) in a large range of Reynolds number (10 – 7500). In terms of zigzag channels, we found a direct relation between the Nusselt number and the ratio of channel hydraulic diameter to the straight section length between two bends ($\frac{d_h}{L_s}$) for the channel geometries studied. In order to further study the influence of this ratio on the heat transfer, in this Chapter a numerical method based on the software ANSYS CFX is applied.

ANSYS CFX is a commercial software specialized in engineering simulation domain based on the finite element method. This software can simulate many physical phenomena, such as computational fluid dynamics (CFD), electronics, semiconductors and so on. In this Chapter, the CFD code is used to study the flow and heat transfer in zigzag channels with the cross-section of 2 mm, a straight channel with same cross-section is also studied as references.

1. Numerical method

1.1 Equations and solution method

The simulation is based on the resolution of equations for the conservation of mass, momentum and energy which deduces the velocity, temperature and the pressure of all the simulation domain. For an incompressible fluid and a steady state, these equations can be written as follows:

Continuity equation:

$$\nabla \cdot (\rho \boldsymbol{u}) = 0 \tag{III-1}$$

Momentum equation (Navier-Stokes):

$$\nabla \cdot \left(\rho \boldsymbol{u} \otimes \boldsymbol{u}\right) = -\nabla p + \nabla \cdot \left(\mu(\nabla \boldsymbol{u} + \nabla \boldsymbol{u}^T)\right) \tag{III-2}$$

Energy equation:

$$\nabla \cdot (\rho \boldsymbol{u} H) = \nabla \cdot (\lambda \nabla T) \tag{III-3}$$

$\boldsymbol{u}$ is the velocity vector, p the pressure, H the enthalpy and T the temperature. The fluid physicochemical properties, such as density ρ, dynamic viscosity μ and thermal conductivity λ, are assumed to be constant (at 25 °C), which make the Prandtl number constant as well (Pr = 6.13). No phase change is considered.

At the inlet, the fluid temperature is constant (equal to 20 °C) and fully-developed flow is assumed. The Poiseuille velocity profile at the inlet is approximated using the expressions suggested by Shah and London [81]:

$$u_{y,z} = \bar{u}\ \left(\frac{2.2+1}{2.2}\right)^2 (1 - \left(abs\left(\frac{2y}{d_h}\right)\right))^{2.2}\ (1 - \left(abs\left(\frac{2z}{d_h}\right)\right))^{2.2} \quad \text{(III-4)}$$

where y, z are the coordinates in the inlet cross-section. At the outlet, zero static gauge pressure is set. At the walls, the no-slip condition and constant heat flux (H2) boundary condition are applied. The value of heat flux is 1×10^5 W.m^{-2}, it comes from one simulation at constant temperature (80 °C) boundary condition at the wall, with inlet temperature of 20 °C and inlet mean velocity of 0.1 m.s^{-1} in the zigzag channel with straight section length of 7 mm.

The simulations were carried out by solving the system of equations with the finite volume CFD code ANSYS CFX 16. All the calculations were performed at steady state in the laminar flow regime. The convective terms were discretized using a second-order bounded differencing scheme. The system was deemed to having reached a converged state when all the locally-scaled residuals fell below 10^{-6}.

1.2 Computational domain and meshing method

For all the geometries studied, the computational domain consists of a three-dimensional zigzag channel with square cross-section of 2 mm and a total length of roughly 0.1 m. Depending on the straight section length L_s, the number of bends varies from one geometry to another (in total 7 geometries). Table III-1 summarizes the number of bends N_{bend} and units N_{unit} for each case. A unit consists of two straight sections and two bends (Figure III-1(b)). All the geometries start and end with a straight section. However, to avoid the potential effects near the outlet which may influence the results, the last straight section is not taken into account in post-processing calculations. Therefore the total length of the channel L considered in the rest of this chapter corresponds to a number of entire units.

Table III-1: Number of bends and units in the zigzag channels with different straight section lengths (d_h = 2 mm)

Geometry	'a'	'b'	'c'	'd'	'e'	'f'	'g'
L_s (mm)	2	3.5	4.5	5.5	7	9	12
N_{bend}	22	16	14	12	10	8	6
N_{unit}	11	8	7	6	5	4	3
L/(m)	0.096	0.094	0.096	0.094	0.094	0.091	0.086

A swept hexahedral mesh is used for the computational domain to provide an efficient and accurate resolution. In the cross-section, the mesh was constructed to be finer near the wall than at the center, as shown in Figure III-1(a), since the fluid velocity and temperature gradients are much higher there. Along the axial direction, the mesh was constructed to be uniform, as shown in Figure III-1(b). A mesh is defined by three numbers of divisions:

- along the channel depth and width, N_d, corresponding to a discretized length equal to d_h;
- along the straight section, N_s, corresponding to a discretized length equal to L_s;
- along the curved section in the bend, N_c, corresponding to a discretized length in the center of the channel equal to L_c.

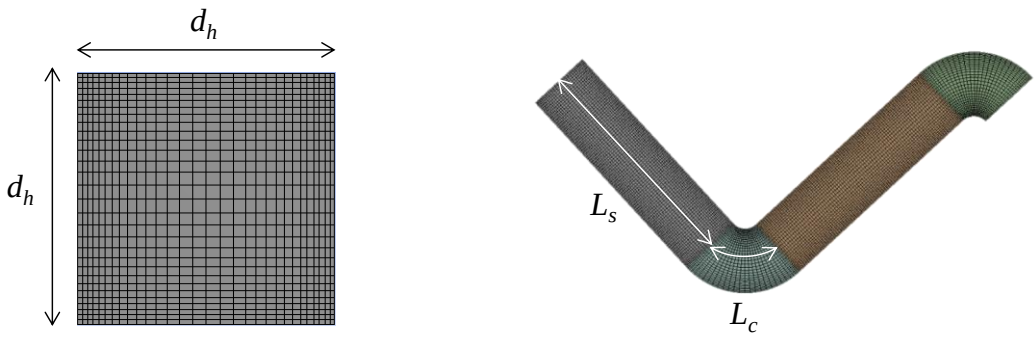

(a) (b)

Figure III-1: Illustration of the mesh for one repeating unit on (a) the cross-section and (b) the wall. d_h = 2 mm, L_s = 2-12 mm, L_c = 2.4 mm.

2. Results and discussion

2.1 Parameters of interest: definitions

From the computed velocity, pressure and temperature fields, parameters of interest are calculated during post-processing. A coordinate reference that follows the main direction of the fluid is used. x is the axial coordinate, normal to the cross-section. At the channel inlet, $x = 0$; at the channel outlet, $x = L$. y and z are the coordinates along the channel width and depth, respectively. By convention, a bar above a parameter refers to an area or peripheral average value. The subscript m is used to refer to a mean value over the axial length. A represents the cross-sectional area of the channel and P the cross-section perimeter length. The heat transfer coefficient at axial location x is defined as:

$$h(x) = \frac{q_w}{\overline{T}_w(x) - \overline{T}_b(x)} \tag{III-5}$$

where q_w is the wall heat flux, $\overline{T}_w$ is the peripheral mean wall temperature and $\overline{T}_b$ is the bulk fluid temperature. The peripheral mean wall temperature is calculated as:

$$\overline{T}_w(x) = \frac{1}{P}\int_{P_x} T_w \; dl \tag{III-6}$$

where P_x refers to the cross-section perimeter at axial location x. The bulk fluid temperature is calculated using Eq. III-7. A_x refers to the cross-sectional area at axial location x. $\boldsymbol{n}$ is the normal vector of the cross-section towards the main direction of the flow.

$$\overline{T}_b(x) = \frac{1}{A\overline{u}}\int_{A_x} (\boldsymbol{u}\cdot\boldsymbol{n}) T \, da \tag{III-7}$$

The local Nusselt number Nu is defined as:

$$Nu(x) = \frac{h(x)d_h}{k} \tag{III-8}$$

The average Nusselt number Nu_m between inlet and axial location *x* is defined as:

$$Nu_m(x) = \frac{1}{x}\int_0^x Nu \; dX \tag{III-9}$$

The local Fanning friction factor f is defined as:

$$f(x) = -\frac{1}{2}\frac{d_h}{\rho\overline{u}^2}\frac{d\overline{p}}{dX}\Big|_{X=x} \tag{III-10}$$

where $\bar{u}$ is the mean fluid velocity, constant along the channel, and $\bar{p}$ is the cross-sectional area average pressure, calculated by:

$$\overline{p}(x) = \frac{1}{A}\int_{A_x} p \; da \tag{III-11}$$

The average Fanning friction factor f_m between inlet and axial location *x* is defined as:

$$f_m(x) = \frac{1}{x}\int_0^x f \; dX \tag{III-12}$$

The results will be discussed in terms of the Reynolds number *Re* defined as:

$$Re = \frac{\rho d_h \overline{u}}{\mu} \tag{III-13}$$

2.2 Grid independence studies

Grid independence studies were carried out to make sure that the size of the grid did not influence the resulting solution for all the simulations carried out. The local Nusselt number Nu and local Fanning friction factor f were assessed for different mesh densities. Grid independence studies for geometry 'f' at *Re* = 560 and geometry 'b' at *Re* = 224 are presented. The variation of the local Nusselt number for different meshes, whose characteristics are given in Table III-2, is shown in Figure III-2. For geometry 'f' at *Re* = 560, from mesh (2) to mesh (3), the local Nusselt number hardly varies and the global average Nusselt number (Nu_m) varies by only 0.35%. Therefore mesh (2) is adequate for this case study with 7.6 million volume elements (N_e) in the computational domain. For geometry 'b' at *Re* = 224, Nu_m varies by 0.54% while N_e is significantly increased. These two cases have been considered to illustrate the grid independence study because they present two different levels of complexity in terms of local

thermal behaviors as can be seen in Figure III-2. This will be discussed further in section 2.3 of this chapter.

Table III-2: Characteristics of the meshes used for geometry ‘f’ at *Re* = 560 and geometry ‘b’ for *Re* = 224

	Geometry ‘f’ (L_s = 12 mm) *Re* = 560			Geometry ‘b’ (L_s = 3.5 mm) *Re* = 224	
Mesh	(1)	(2)	(3)	(1)	(2)
N_d	40	60	80	40	60
N_s	120	180	240	120	180
N_c	40	60	80	40	60
N_e (million)	2.2	7.6	18	4.3	14.5
Nu_m	20.19	19.84	19.77	20.19	19.84

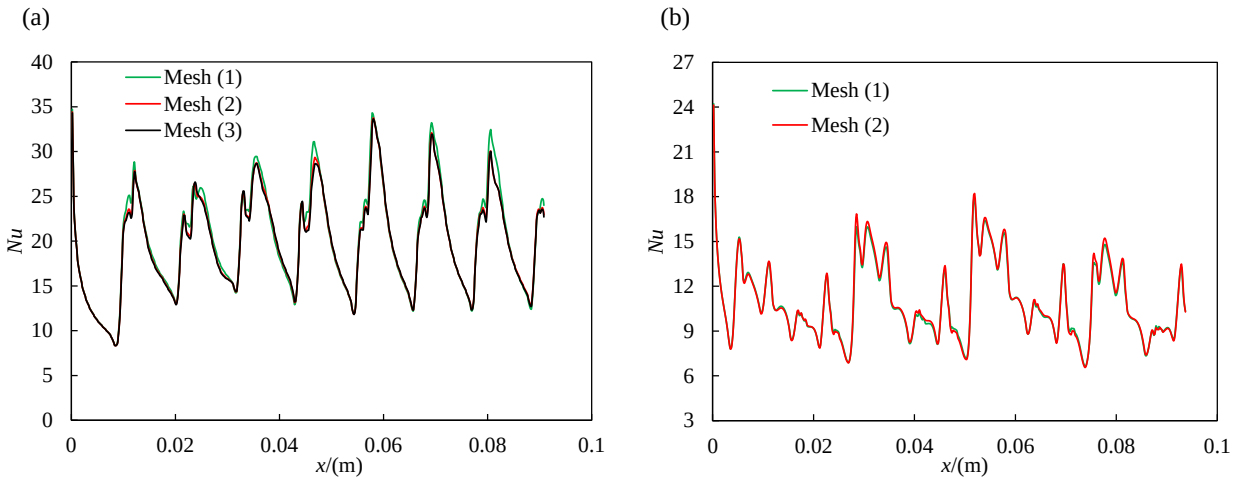

Figure III-2: Mesh influence on the local Nusselt number in (a) geometry ‘f’ for *Re* = 560 and (b) geometry ‘b’ for *Re* = 224

2.3 Local results

2.3.1 Analysis of the temperature field

The hot point (maximum temperature) and cold point (minimum temperature) at different axial cross-sections in the geometry ‘e’ and in straight channel with the same cross-section for *Re* = 112-336 are presented in Figure III-3. The bulk temperature in the two channels are presented

as well, in fact the value is the same in two channels, so the difference is not made in this figure. It can be observed that the difference of hot point and cold point in zigzag channel are smaller than in straight channel, suggesting the temperature field in zigzag channel is more homogeneous than in straight channel. In addition, this temperature difference decreases with increasing Reynolds number for both channels, which means that the temperature field is more homogeneous for high Reynolds number. To further compare the local temperature in zigzag channel and straight channel, the temperature fields of one cross-section at x = 0.075 m in these two channels (corresponding to the outlet of the 8^{th} bend for zigzag channel) for Re = 224 are presented in Figure III-4 (a) and (b). As expected, the temperature field over a cross-section in the zigzag channel is more homogeneous than in the straight channel. In the straight channel, characterized by a laminar Poiseuille flow (Figure III-4(c)), the heating of the successive concentric flow layers occurs by thermal diffusion. In the zigzag channel, the Dean vortices generated by the bends (Figure III-4(d)) create radial mixing which improves temperature homogenization over the channel cross-section.

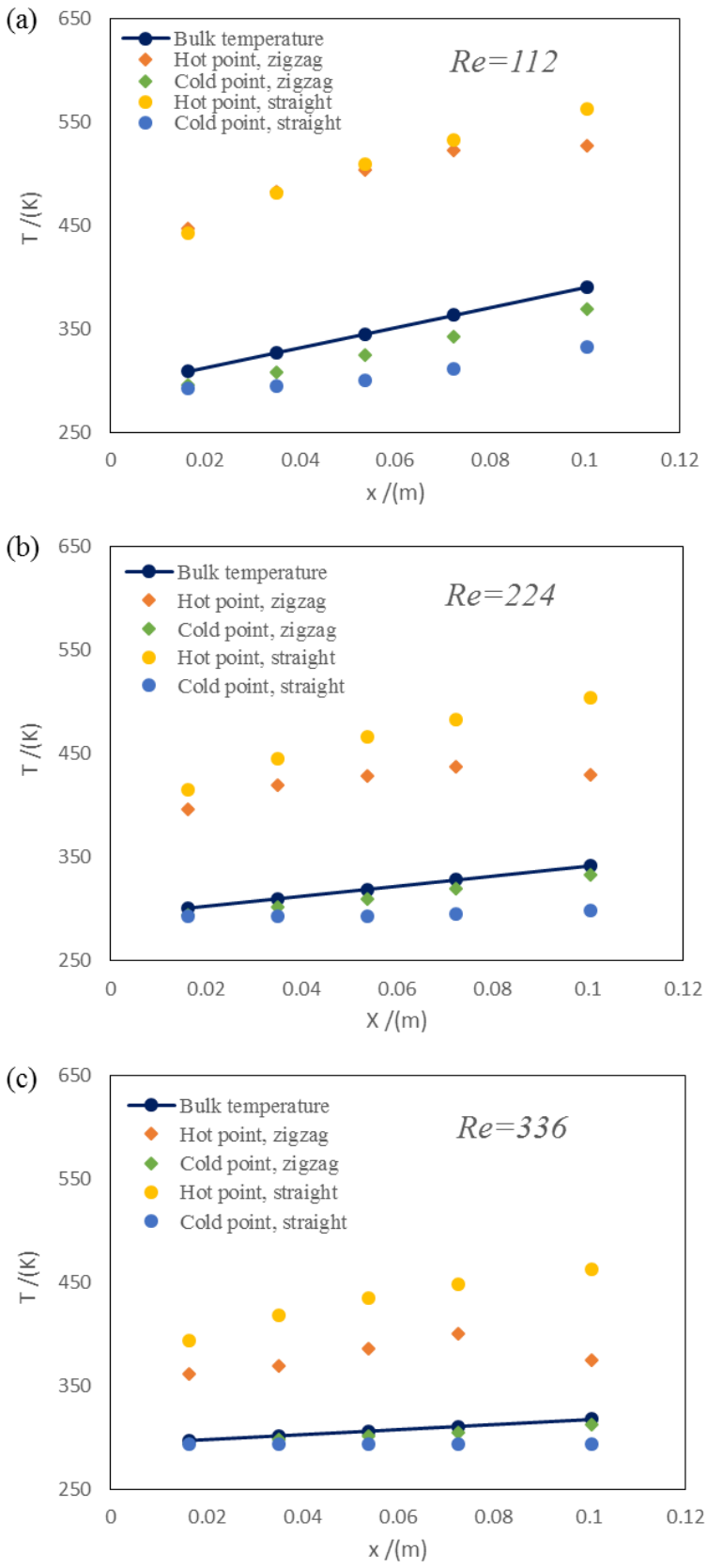

Figure III-3: Hot point and cold point at different axial cross-sections in the zigzag channel ‘e’ and in the straight channel for *Re*: (a) 112, (b) 224, (c) 336

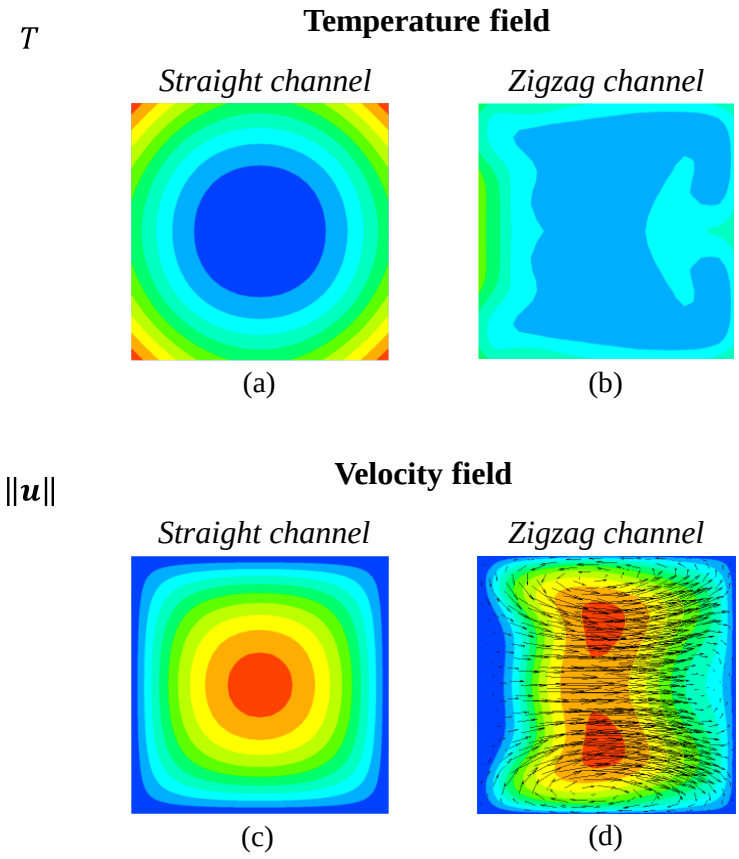

Figure III-4: Temperature and velocity fields over the cross-section at x = 0.075 m in (a, c) the straight channel and in (b, d) the zigzag channel 'e' for Re = 224. The black arrow is the tangential velocity.

For further comparison, the value of the relative maximum temperature difference (T_{max} - T_{min})/$\bar{T}$ and the relative standard temperature deviation $\sigma_T/\bar{T}$ (equation III-14) over the cross-section at x = 0.075 m for both channels are calculated at different Reynolds numbers and shown in Figure III-5.

$$\frac{\sigma_T}{\bar{T}} = \frac{\sqrt{\frac{1}{A}\int_{A_x}(T-\bar{T})^2 da}}{\bar{T}} \qquad \text{(III-14)}$$

(T_{max} - T_{min})/$\bar{T}$ and $\sigma_T/\bar{T}$ decrease both in the zigzag channel and the straight channel with increasing Reynolds number. (T_{max} - T_{min})/$\bar{T}$ and $\sigma_T/\bar{T}$ in the zigzag channel are significantly smaller than in the straight channel, indicating the temperature in the zigzag channel is more homogeneous as mentioned previously. For the design of compact heat exchangers-reactors, this is very favorable when exo- or endothermic reactions are carried out since it avoids extreme

temperatures and therefore leads to better control of reactant conversion, limits the formation of by-products and the device operates under safer conditions.

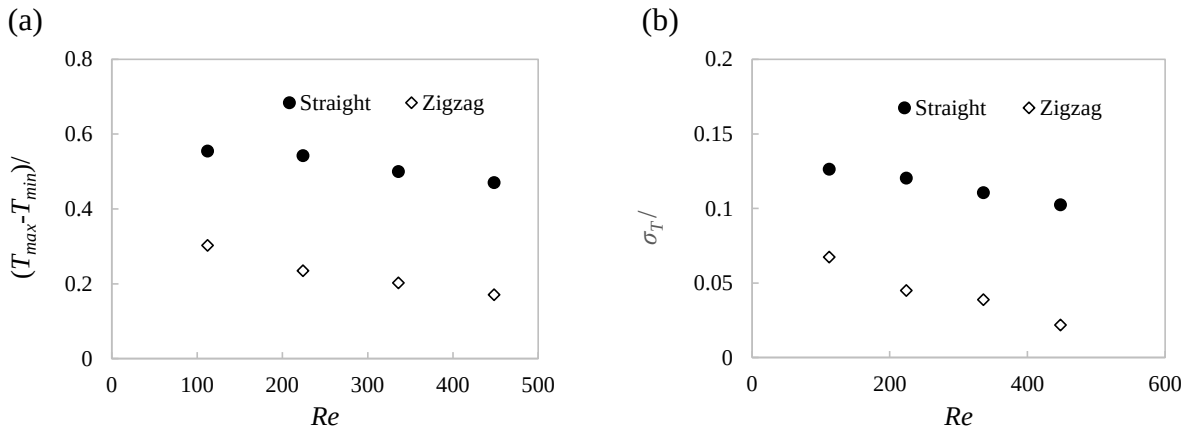

Figure III-5: (a) Relative maximum temperature difference and (b) relative standard temperature deviation over the cross-section at x = 0.075 m in the straight channel and the zigzag channel ‘e’ versus Reynolds number

2.3.2 Evolution of *Nu* and *f* versus *Re*

The results obtained in the zigzag channel ‘e’ are used to illustrate the flow and heat transfer (d_h/L_s = 0.29) and are compared with the results for the straight channel. The local Nusselt number *Nu* and Fanning friction factor f from the channel entrance to the exit of the 5th unit in the zigzag channel for *Re* = 112 - 448 are shown in Figure III-6. The profiles in the straight channel are also presented. In the straight channel, the local Nusselt number decreases along the channel (Figure III-6(a-d)). This is typical of the thermal boundary layer development in laminar flow as a constant fluid temperature has been set at the channel inlet in the simulations. The asymptotic value of *Nu* obtained in the simulations at high x is consistent with the theory. Indeed Nusselt number of 3.091 should be reached for hydrodynamically and thermally fully-developed laminar flow in the case of square channels with (H2) thermal boundary condition for all *Re* [82]. The local Fanning friction factor in the straight channel is constant since a fully-developed laminar flow has been set at the channel entrance (Figure III-6(e-h)). The slight increase observed in the very first millimeters is due to the approximate laminar velocity profiles set at the inlet. The values of f fit with the theory that gives f = (14.227/*Re*) for fully-developed laminar flow [82].

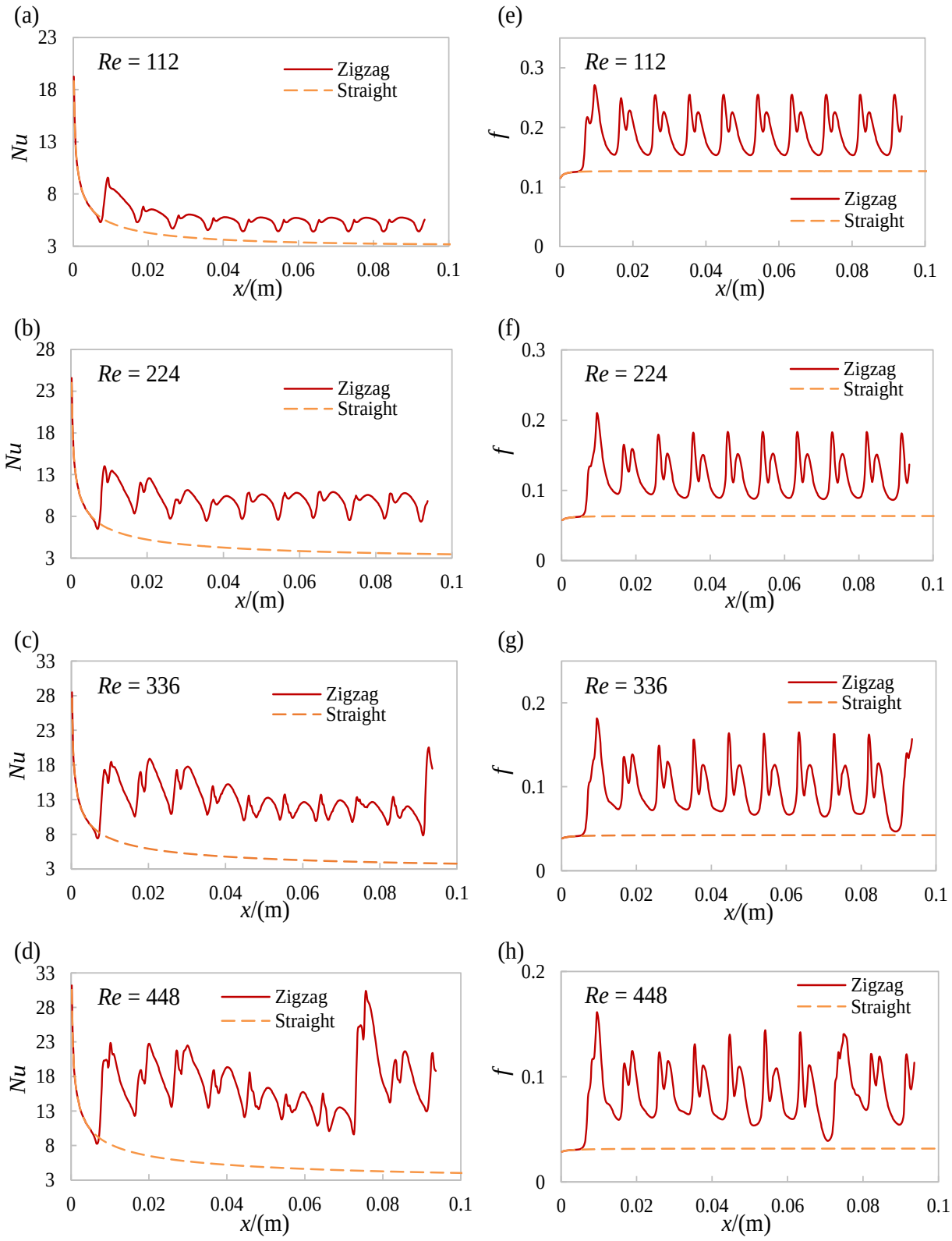

Figure III-6: (a-d) Local Nusselt number and (e-h) Fanning friction factor profiles in the straight channel and zigzag channel 'e' for Re = 112-448, d_h/L_s = 0.29.

In the zigzag channel, the evolution of *Nu* and *f* in the entrance zone perfectly fits with those observed in the straight channel as the zigzag channel starts with a straight section. Then, oscillations appear that correspond to the periodicity of the geometry studied. Both *Nu* and *f* start to increase just before the bends and decrease in the straight sections. It can be observed that *Nu* and *f* in the zigzag channel are significantly higher globally than those in the straight channel, suggesting as expected that the bends enhance heat transfer but cause additional pressure loss. *Nu* increases with *Re* in the zigzag channel, while it is roughly constant in the straight channel. For both channel configurations, *f* decreases as *Re* increases. In the zigzag channel it is particularly observable that the oscillations in *Nu* and *f* are regular at low Reynolds number from the 4th bend (Figure III-6 (a,b,e,f)), having a constant amplitude. From that bend, the flow can be considered as both hydrodynamically and thermally developed. The fluid behaves in the same way in each bend and each straight section. However, at higher Reynolds number (Figure III-6 (c,d,g,h)), the amplitude of the oscillations becomes irregular whatever the axial location. Regarding *Nu*, the amplitude tends to decrease along the channel until a significant jump is observed. The jump is observed earlier as Reynolds number increases. This irregular behavior in wavy channels has already been observed and has been interpreted as chaotic flow [68,105], in this paper it is named as non-periodic flow.

To understand the transition from periodic flow to non-periodic flow, the velocity fields in both cases are studied. Velocity fields and relative tangential velocity vectors at different cross-sections between two bends for *Re* = 224 and 448 are shown in Figure III-7 and Figure III-8. The relative tangential velocity is defined as the tangential velocity divided by the mean fluid velocity. For both Reynolds numbers, at the entrance of a bend, the high velocity zone is close to the inner side of that bend (corresponding to the outer side of the previous bend) and then moves towards the outer side due to centrifugal effects (Figure III-7(a) and Figure III-8(a)). In cross-section (b), the relative tangential velocity vectors are mainly towards the inner side of the bend under the effect of centrifugal forces created by the previous bend. For the following cross-sections (c-h), Dean vortices appear, and the number of vortices varies from two to four. Their intensity becomes stronger in the bend and decreases along the straight channel. The direction of the relative tangential velocity changes and shifts towards the inner side of the next bend as shown in cross-section (i). However, it has to be underlined that in cross-section (h), for *Re* = 224 (Figure III-7), the tangential movement has almost vanished while the Dean vortices are still perceptible for *Re* = 448 (Figure III-8). By comparing the cross-section (b) and (i), the relative tangential velocity field is almost the same at the entrances of the two bends for

Re = 224 (Figure III-7). The only change is the direction, suggesting the flow behavior in the next bend returns to that of the previous bend. For *Re* = 448, the flow behavior in the coming bend does not return to that of the previous bend, as the instability created in this bend is still significant (Figure III-8(i)). This flow regime is more irregular and unstable, different from that at a Reynolds number of 224 where the fluid spends more time in the straight section.

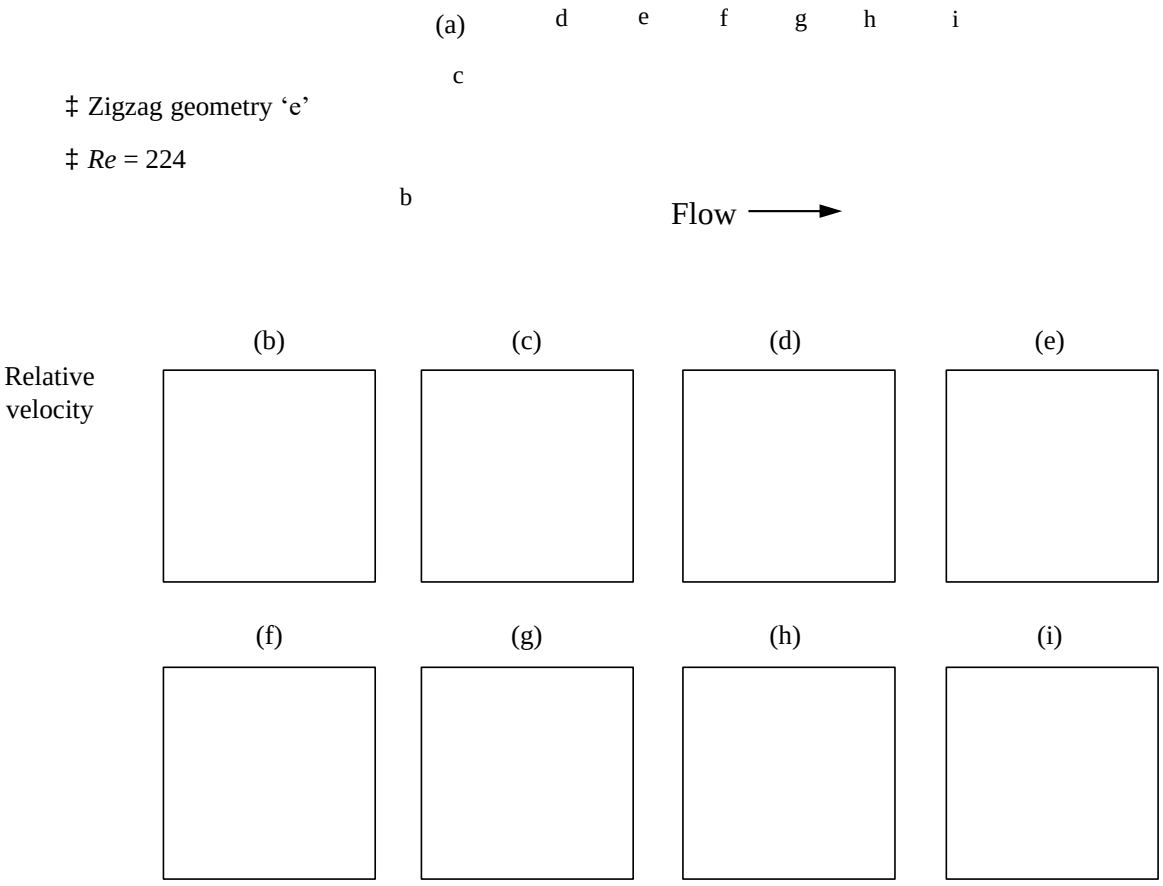

Figure III-7: (a) Velocity fields and (b-i) relative tangential velocity vectors at different cross-sections between two bends at *Re* = 224 in zigzag channel ‘e’. The top side in (b-i) corresponds to the outer side of the bend studied.

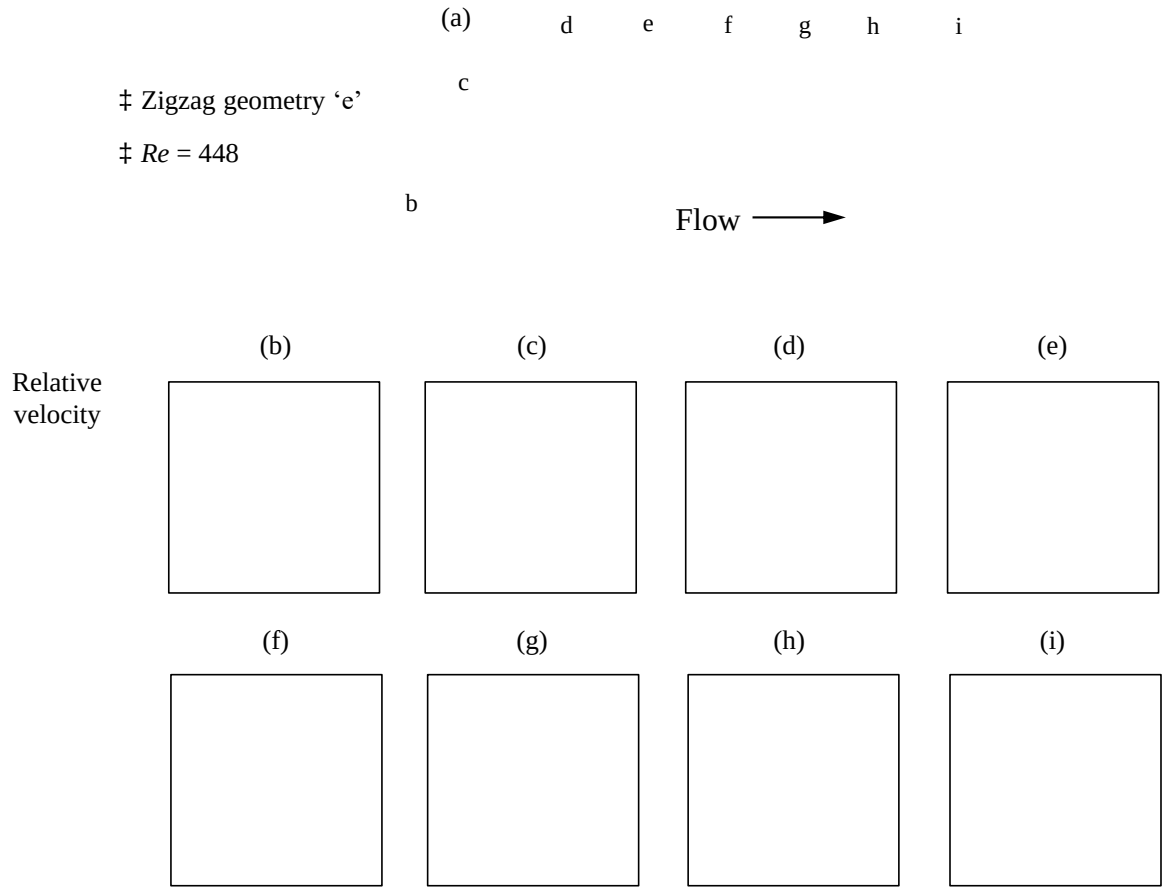

Figure III-8: (a) Velocity fields and (b-i) relative tangential velocity vectors at different cross-sections between two bends at Re = 448 in zigzag channel ‘e’. The top side in (b-i) corresponds to the outer side of the bend studied.

2.3.3 Evolution of Nu and f versus L_s

Different zigzag channels with straight section lengths ranging from 3.5 mm to 12 mm are studied at Re = 224. The local Nusselt number Nu and friction factor f from the channel entrance to the exit of the last unit of the zigzag channel are shown in Figure III-9(a-j). The local Nusselt number and friction factor in a straight channel with the same cross-section at the same Reynolds number are also presented as a reference. It is observed that the transition between periodic flow (Figure III-9(d-e, i-j)) and non-periodic flow (Figure III-9(a-c, f-h)) occurs as the straight section length is decreased. By analogy with the previous part, where the non-periodic flow occurs by increasing the fluid velocity, it is confirmed that reducing the residence time between two bends favors the occurrence of a non-periodic flow regime.

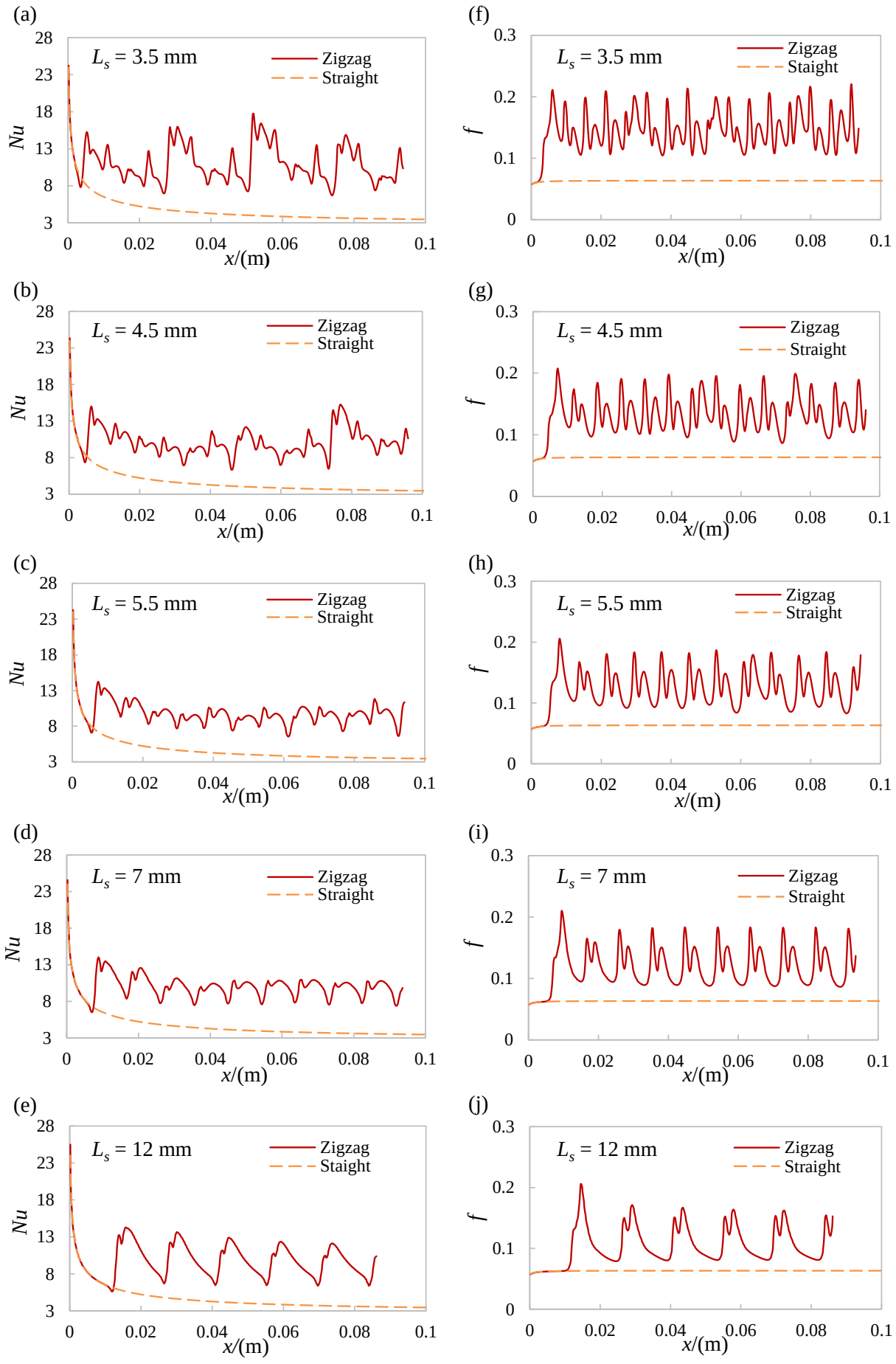
(a)
L_s = 3.5 mm
Zigzag
Straight
Nu
x/(m)
(b)
L_s = 4.5 mm
Zigzag
Straight
Nu
x/(m)
(c)
L_s = 5.5 mm
Zigzag
Straight
Nu
x/(m)
(d)
L_s = 7 mm
Zigzag
Straight
Nu
x/(m)
(e)
L_s = 12 mm
Zigzag
Staight
Nu
x/(m)
(f)
L_s = 3.5 mm
Zigzag
Staight
f
x/(m)
(g)
L_s = 4.5 mm
Zigzag
Straight
f
x/(m)
(h)
L_s = 5.5 mm
Zigzag
Straight
f
x/(m)
(i)
L_s = 7 mm
Zigzag
Straight
f
x/(m)
(j)
L_s = 12 mm
Zigzag
Straight
f
x/(m)

Figure III-9: (a-e) Local Nusselt number and (f-j) Fanning friction factor profiles in the straight channel and the zigzag channel with L_s = 3.5-12 mm at Re = 224.

2.3.4 Fourier analysis for non-periodic flow detection

A fast Fourier analysis was used to analyze the local Nusselt number and the friction factor in the zigzag channels. It converts the signal of Nusselt number and friction factor from the spatial domain to the frequency domain. The fast Fourier transform analysis is applied to ($Nu - Nu_m(L)$) and ($f - f_m(L)$). $Nu_m(L)$ and $f_m(L)$ represent the global Nusselt number and friction factor, respectively, calculated by averaging the local values from the channel inlet (x = 0) to the outlet ($x = L$). Here two cases are presented with the straight section length L_s equal to 7 mm and 3.5 mm at Re = 224 as shown in Figure III-10. For zigzag channels 'e' with L_s = 7 mm, the Fourier transform spectrum of Nusselt number contains a unique primary frequency f_1 and its harmonic frequencies $2f_1$, $3f_1$, $4f_1$, etc. (Figure III-10(a)). f_1 is equal to the frequency of the bend in the channel given by:

$$f_1 = \frac{\overline{u}}{L_s + L_c} \tag{III-15}$$

It is equal to 10.69 Hz for zigzag channels 'e' with Re = 224.

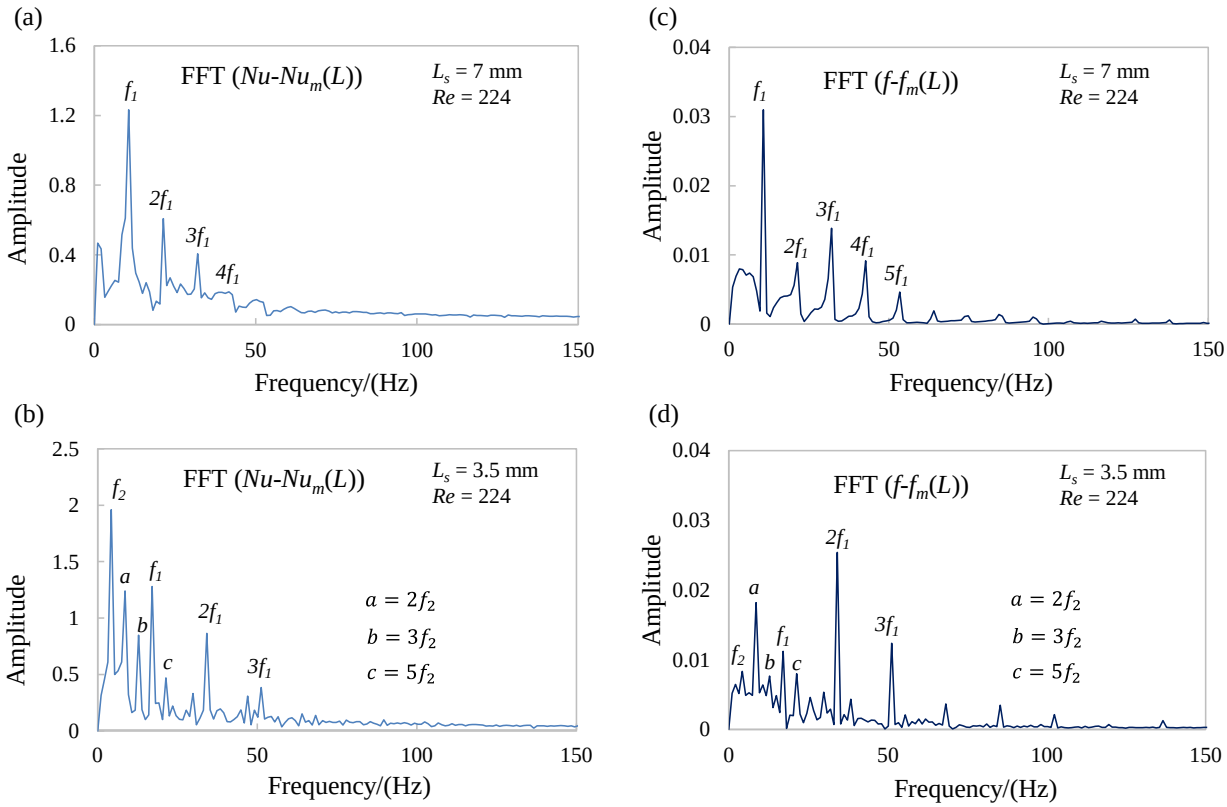

Figure III-10: Fast Fourier transform analysis for Nusselt number and friction factor in zigzag channels with straight section lengths of (a,c) 7 mm and (b,d) 3.5 mm at *Re* = 224.

The same observation can be made in the spectrum of the friction factor where the basic frequency is the same (Figure III-10(b)). These results show that the flow is in a periodic regime with a single oscillation frequency. For zigzag channels 'b' with L_s = 3.5 mm (Figure III-10(b,d)), another basic frequency f_2 (4.27 Hz) appears in addition to the primary frequency f_1 (17.08 Hz) in the spectra of Nusselt number and friction factor. The ratio f_2/f_1 is a quarter. All the other spectral peaks are the harmonic frequencies of these two basic frequencies f_1 and f_2. The flow is no longer in the periodic regime but non-periodic. This analysis methodology has been widely used for flow transition scenario studies although classically it is applied to velocity, not to Nusselt number or friction factor [106–110].

With the help of fast Fourier transform analysis, the flow pattern periodic or non-periodic for different channel configurations at different Reynolds numbers can be distinguished. A map is plotted to show the flow regime as a function of Reynolds number and normalized straight section length L_s/d_h (Figure III-11). For the data marked with a full triangle in the figure, the

simulation converged but the grid independence was not achieved. A transient solver has been tested to simulate the condition where Re = 560 and L_s = 7 mm as transient laminar flow was observed in analogous geometries [111]. In the present case, the transient simulations converge towards a steady solution but the converged solution still depends on the mesh grid size. Reducing the mesh size is impractical. In the map, a boundary line between periodic and non-periodic flow can be observed. As mentioned before, the non-periodic flow regime can be achieved by decreasing the straight section length between two bends or by increasing the fluid velocity.

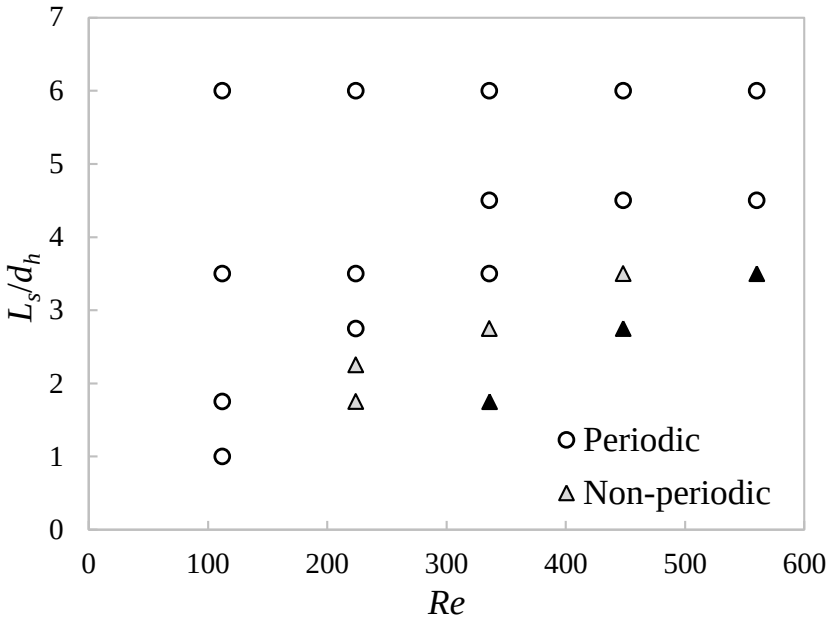

Figure III-11: Map of periodic flow and non-periodic flow in the zigzag channels studied for Re = 112-560.

2.4 Global results

2.4.1 Average Nusselt number and friction factor

The average Nusselt number Nu_m and friction factor f_m in the different zigzag channels at different Reynolds numbers were also studied. Two cases of average Nusselt number at Re = 224 are presented in Figure III-12: one is in the steady periodic regime with a straight section length of 12 mm, whilst the other is in the non-periodic regime with a straight section length of 3.5 mm. The average Nusselt number in the straight channel is also presented. In both regimes, it can be seen that the Nusselt number quickly becomes stable while, in the straight channel, it decreases along the simulated length. The average Nusselt number stabilizes after several bends,

indicating the thermal boundary layer has been fully-developed for both flow regimes within a zigzag channel length of few centimeters.

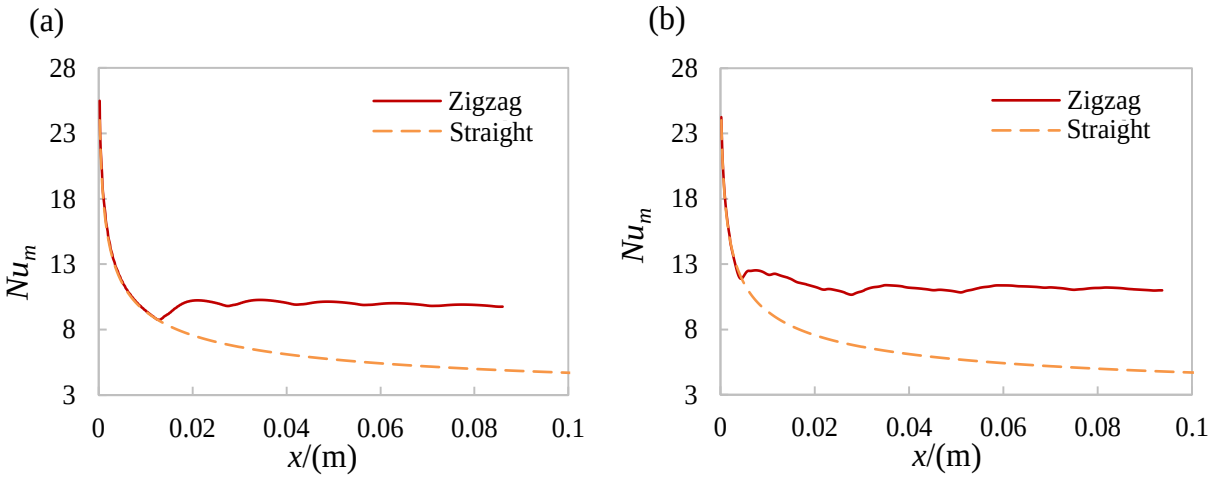

Figure III-12: Average Nusselt number in straight channel and zigzag channel at *Re* = 224: (a) L_s = 12 mm; (b) L_s = 3.5 mm.

The average Nusselt number and friction factor at axial coordinate x = 0.086 m (channel length of geometry 'g') was chosen as a representation of the global average Nusselt number and friction factor for all the zigzag channels studied, where the thermal boundary layer is considered as fully-developed (denoted by an infinity superscript). The Nusselt number and friction factor are plotted as a function of L_s/d_h, as presented in Figure III-13. In Figure III-13(a), the Nusselt number increases with increasing Reynolds number for all the channel geometries. Its variation for different L_s/d_h seems to be random at the same Reynolds number, indicating the influence of the straight section length on the heat transfer is not obvious in the zigzag channel. This is contrary to the experimental result presented in Chapter II where it is found there is a direct relation between Nusselt number and the ratio (L_s/d_h). However, it has to be noticed that the range of the Reynolds number numerically investigated (Re < 600) is much lower than that studied in the experiment (Re < 8 000). Even in the experiments, the influence of the ratio L_s/d_h on the Nusselt number is small at low Reynolds number (in Figure II-10). Concerning the friction factor, it decreases with increasing L_s/d_h or Reynolds number, as shown in Figure III-13(b), since the number of singularities (i.e. bends) increases with decreasing straight section length between two bends for a fixed channel developed length.

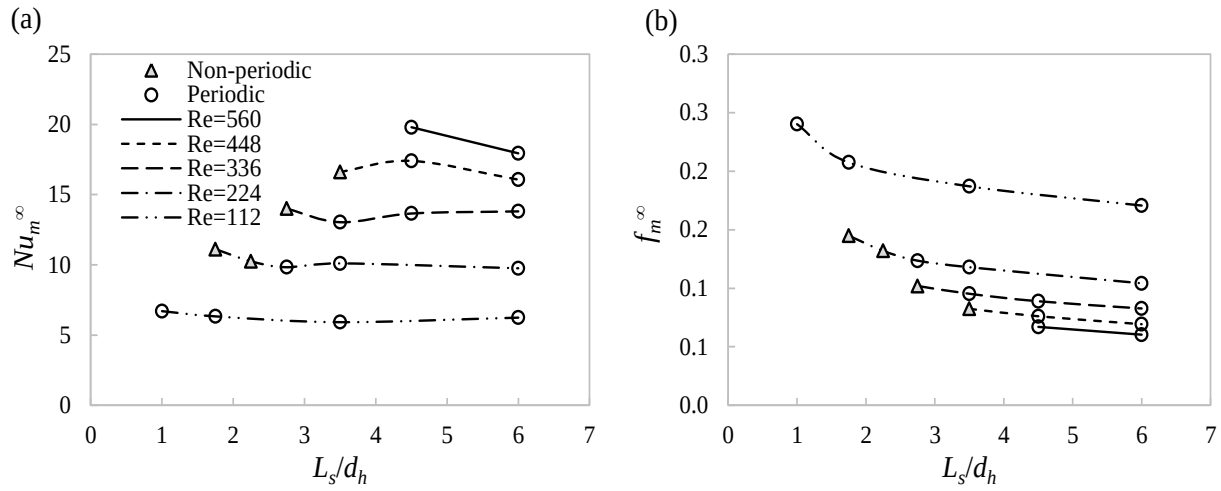

Figure III-13: Fully-developed average Nusselt number (a) and friction factor (b) in the zigzag channels.

2.4.2 Heat transfer enhancement

As discussed above, the zigzag channel configuration enhances heat transfer compared with the straight channel with the same cross-section. This heat transfer enhancement is accompanied by higher pressure drop which has been noted. The heat transfer enhancement factor is defined as:

$$e_{Nu} = \frac{{Nu_m}^\infty}{{Nu_0}^\infty} \tag{III-16}$$

where ${Nu_0}^\infty$ is the Nusselt number in a straight channel. As mentioned before, for hydraulically and thermally developed laminar flow, ${Nu_0}^\infty = 3.091$ for a square channel with H2 thermal boundary condition [82]. e_{Nu} for the studied zigzag configurations at different Reynolds numbers is plotted in Figure III-14. It is observed that the presence of the bends improves the heat transfer significantly, notably at high fluid velocity. e_{Nu} increases with increasing Reynolds number for the different zigzag configurations. Its variation is random in terms of L_s/d_h, indicating the impact of non-periodic flow on heat transfer enhancement is not obvious for the conditions simulated. Here the pressure drop penalty is not taken into account.

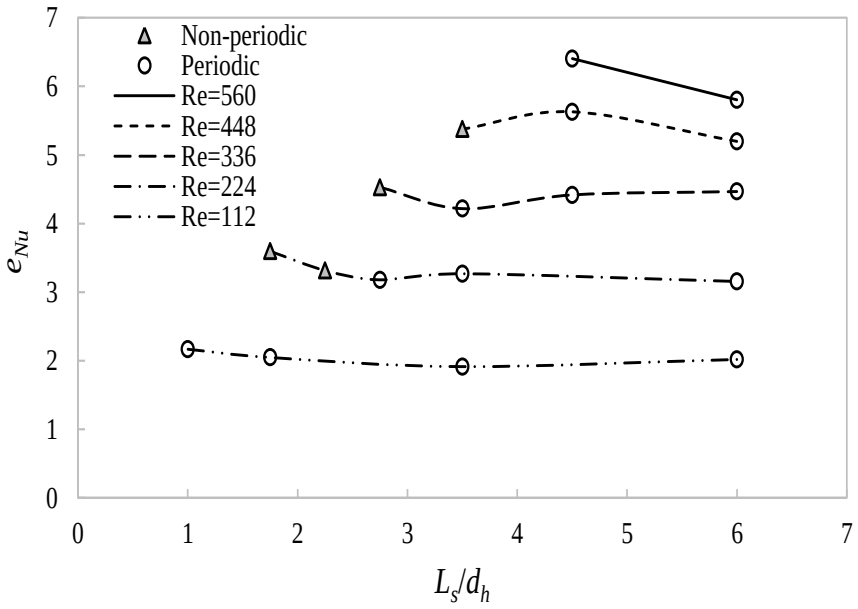

Figure III-14: Heat transfer enhancement in the zigzag channels studied.

2.4.3 Thermo-hydraulic performance factor

Another factor *PF* (thermo-hydraulic performance) is then defined which considers the pressure drop penalty. This factor takes the straight tube as the reference and is very useful for comparing different heat transfer technologies. It is the ratio of the heat exchange capacity (global heat transfer coefficient *h* multiplying heat exchange area A_H) in the considered technology to that in a straight tube divided by the ratio of the flow friction power in the technology $\mathcal{P}$ to that in a straight tube $\mathcal{P}_0$:

$$PF = \frac{(h_m A_H / h_0 A_{H,0})}{(\mathcal{P}/\mathcal{P}_0)} \quad \text{(III-17)}$$

The flow friction power depends on the pressure drop Δp in the channel and the volumetric flowrate *Q*:

$$\mathcal{P} = \Delta p \cdot Q \quad \text{(III-18)}$$

Webb and Eckert have proposed different ways to compare the relative performance of heat exchangers with rough surface tubes compared with heat exchangers with smooth surface tubes [112]. They proposed a list of parameters of interest depending on user constraints (for instance the ratio of the surface areas while constant flow friction power and volumetric flowrate are imposed). By analogy, in the present study, each zigzag channel is compared with a straight channel of the same cross-section assuming that:

- both configurations must provide the same heat exchange capacity in order to heat or cool a fluid from a fixed temperature to a desired one (equation III-19);

- the fluid flowrate is imposed (equation III-20).

$$h_m{}^{\infty} A_H = h_0{}^{\infty} A_{H,0} \quad \text{(III-19)}$$

$$Q = Q_0 \quad \text{(III-20)}$$

Therefore, from equations III-19) and III-20, the performance factor can be expressed as follows:

$$PF = \frac{\Delta p_0}{\Delta p} \quad \text{(III-21)}$$

In other words, the performance factor considered in the present study compares the pressure drop in a straight channel with that in a zigzag channel with the same cross-section and flow rate. In order to obtain the same heat exchange capacity, the length of both channels will be different. The pressure drop can be expressed as a function of the mean fluid velocity, the Fanning friction factor, the hydraulic diameter and the channel length:

$$\Delta p = 2\rho \overline{u}^2 f^{\infty} \frac{L}{d_h} \quad \text{(III-22)}$$

For same flowrate and hydraulic diameter, the performance factor simplifies to:

$$PF = \frac{f_0{}^{\infty} L_0}{f^{\infty} L} \quad \text{(III-23)}$$

where L_0 is the straight channel length and $f_0{}^{\infty}$ the Fanning friction factor for fully-developed laminar flow in square straight channel [82]:

$$f_0{}^{\infty} = \frac{14.227}{Re} \quad \text{(III-24)}$$

Considering the same cross-section in the zigzag and straight channels, the ratio of channel lengths is equal to the ratio of heat exchange areas. From equation III-19, the following expression is then obtained:

$$\frac{L_0}{L} = \frac{A_{H,0}}{A_H} = \frac{h_m{}^{\infty}}{h_0{}^{\infty}} = \frac{Nu_m{}^{\infty}}{Nu_0{}^{\infty}} \quad \text{(III-25)}$$

From equations III-23, III-24, III-25, the performance factor can finally be expressed as follows:

$$PF = \frac{14.227}{Re}\frac{{Nu_m}^{\infty}}{f^{\infty}{Nu_0}^{\infty}} \quad \text{(III-26)}$$

PF for the channel configurations studied at different Reynolds numbers is presented in Figure III-15. For all the cases studied, *PF* is greater than one, suggesting that the bends significantly enhance the thermo-hydraulic performances of the channel. That means the zigzag channel brings less significant pressure drop compared with the heat transfer enhancement. *PF* increases with increasing Reynolds number or L_s/d_h. The increase with Reynolds number is particularly important at low *Re*. From *Re* = 336, the increase becomes moderate with increasing Reynolds number. Concerning the impact of the straight section, decreasing its length to reach non-periodic flow regime is not interesting in terms of thermo-hydraulic performances in the cases studied. Finally, it has to be noted that by increasing L_s/d_h, the zigzag design will get closer to the straight channel. Therefore, the different curves should converge towards *PF* = 1 for very high L_s/d_h, depicting a bell-shaped curve with an optimal range of L_s/d_h values depending on *Re*. The observed plateaus for *Re* = 448 and *Re* = 560 suggest that this optimum is between L_s/d_h = 4.5 and 6 for these conditions.

Figure III-15: Thermo-hydraulic performance factor in the zigzag channels studied.

3. Comparison between simulation and experimental results

Here the simulation results of the geometry ‘e’ is compared with the experimental results in Chapter II in terms of Nusselt number. *Nu* in zigzag channel at two small Reynolds numbers (285, 576) in the experiment is introduced. As the Prandtl number *Pr* in the simulation (6.13)

and experiment (between 3.2 and 4.3) is different, it is presented as $Nu/Pr^{0.33}$ for the comparison. The power factor of Pr is 0.33 as suggested by Sieder and Tate correlation in laminar flow or Colburn correlation in turbulent flow [113]. $Nu/Pr^{0.33}$ is plotted as a function of Re as shown in Figure III-16. It is observed that the simulation results fit well with the experimental data which validates the simulation results.

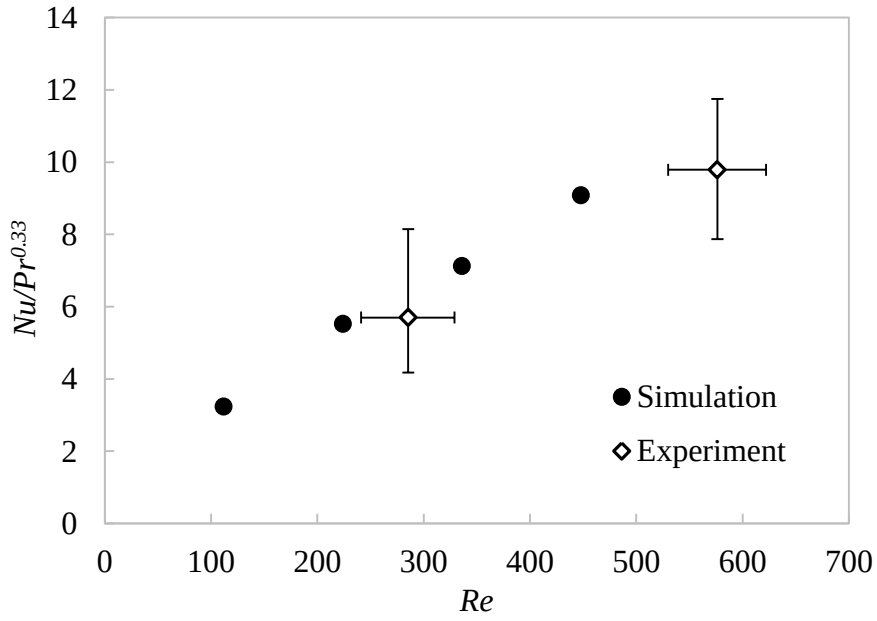

Figure III-16: Comparison of $Nu/Pr^{0.33}$ from simulation and experiment for the zigzag channel 'e'. The experimental error is estimated from the accuracy of the sensors (±0.2 $kg.h^{-1}$ for the process fluid flowrate, ±3 $kg.h^{-1}$ for the utility fluid flowrate, ±0.3 °C for the temperatures).

In Chapter II, a correlation of Nusselt number in zigzag channel is proposed which takes the fluid properties and channel geometries into account. For furtherly comparing the simulation and experimental results, the simulation data of Nusselt number for all the geometries studied is compared with the values calculated by this correlation (equation II-16). They are plotted in Figure III-17, with the experimental data of Nusselt number for water and glycerol solution in Chapter II. Two simulations (one case for each channel) for similar geometry 'e' with the cross-section length of 3 mm and 4 mm have also been conducted. The results are presented in this figure as well. This can be another way to validate the simulation results. In this figure, most

simulation data fall into the 20% error line, indicating the simulation results are in agreement with the experimental ones.

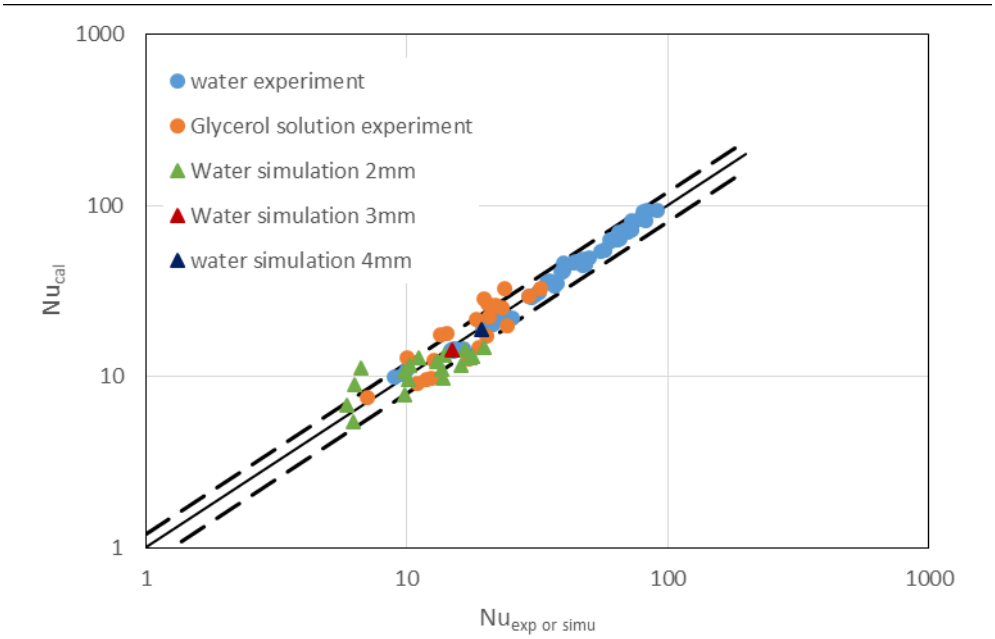

Figure III-17: Comparison of characterized Nusselt number (by simulation and experiment) and calculated by the proposed correlation in zigzag channels, dashed lines are with 20% error.

4. Conclusions

A numerical method based on the software ANSYS CFX has been developed to study the flow and heat transfer in millimetric zigzag channels with square cross-section of 2 mm. The simulations are carried out for the steady laminar flow regime with Reynolds numbers ranging from 112 to 560 and a Prandtl number of 6.13. The channel geometry in terms of straight section length between two bends from 2 mm to 12 mm has been investigated. The flow and heat transfer in a straight channel with the same cross-section is also studied as a reference. The numerical method is validated by comparing the results with the experimental data for Nusselt number obtained in Chapter II.

The results show that local Nusselt numbers and Fanning friction factors vary along the zigzag channels in form of oscillating curves. The amplitude of the oscillations is constant with periodic flow but varies in the case of non-periodic flow. Based on Fourier analysis, a map has been provided which allows to distinguish the conditions in terms of Reynolds number and straight section length that gives a periodic flow or a non-periodic flow. Non-periodic flow is

obtained by increasing the fluid velocity or by decreasing the straight section length. For Re = 560 and L_s/d_h = 3.5, the flow instability created by the bends was too great for steady laminar flow to develop. The heat transfer enhancement and thermo-hydraulic performance factor are quantitatively discussed, showing the zigzag channel enhances the heat transfer strongly and increases pressure drop less significantly compared with the straight channel. It appeared that non-periodic flow is not particularly interesting in terms of thermo-hydraulic performances. All these data should be very useful for the design of high-performance heat exchangers-reactors. The impact of other geometric parameters, such as the hydraulic diameter, the curvature radius of the bends and their angle should be furtherly studied.

In the simulation, problems of convergence or mesh independence have been met when Reynolds number increases (in laminar regime) or when the straight section length between two bends decreases. In addition, it is much more complicated to carry out the simulation in transient regime since there is not a satisfying thermal-hydrodynamic model available for this flow regime. In order to overcome these limitations of simulation, an experimental method based on laser-induced fluorescence thermometry is developed and described in the next chapter for the measurement of local temperature, which is not limited by the Reynolds number. Temperature measurement is very important for chemical process, as the temperature can directly influence the yield and selectivity. There is also a safety concern for highly exothermic reactions.

Chapter IV: Characterization of temperature field by laser-induced fluorescence

In the previous chapter, a numerical method based on the software ANSYS CFX has been used to study the flow and heat transfer in the zigzag channels. The local results like temperature field, velocity field and pressure can be obtained by the resolution of the CFD code. However, as mentioned in that chapter, the simulation is limited by the Reynolds number, especially for the transient regime where classical models available fail to accurately represent this flow regime. So in this chapter, an experimental method based on laser-induced fluorescence thermometry is developed to measure local temperature in millimetric zigzag channels. The two-color/two dye approach with opposite temperature sensitivities are utilized in order to have high sensitivity for the temperature measurement. As mentioned in Chapter I, this method is particularly interesting for small devices because it is non-intrusive and does not disturb the flow. It provides immediate response which can also be adapted to unsteady flows.

The experiment is carried out in three heat-exchanger reactor prototypes with zigzag channels, which have been studied in Chapter II. The temperature measurement at different longitudinal positions and different height levels inside the zigzag channels are conducted. The temperature field is deduced from the fluorescence signal. The mean temperature is calculated and then compared to that calculated by a heat transfer model with the purpose of evaluating the reliability of this method.

1. Principle of laser-induced fluorescence thermometry with two dyes

1.1 Fluorescence signal equation

According to Chaze et al. [96], the fluorescence signal dF_λ emitted at a wavelength λ in an elementary volume dV of liquid can be expressed as:

$$dF_\lambda = \eta \frac{\Omega}{4\pi} \varepsilon_0 \phi_\lambda \frac{I_0}{(1+\frac{I_0}{I_{sat}})} C dV \quad \text{(IV-1)}$$

where η is the transmission efficiency of the fluorescence light of the detector, Ω is the solid angle of the collection, ε_0 is the molar absorptivity of the fluorescent molecules at the excitation wavelength of the laser beam, ϕ_λ is the fluorescence quantum yield, I_0 is the laser intensity, I_{sat}

is the saturation intensity of the fluorescent dye, C is the molar concentration of the dye. In this equation, ε_0, ϕ_λ, I_{sat} are dependent on the temperature. ϕ_λ decreases with the temperature due to collisional quenching while I_{sat} increases with the temperature [96].

1.2 Temperature measurement based on two dyes

The analysis of the spectra of absorption and fluorescence emission of different dyes is necessary for choosing the couple of dyes. First of all, the dyes should display different sensitivities to temperature in terms of emission spectra. Fluorescein disodium (FL) is chosen as one of the dye in this thesis because of its high sensitivity (fluorescence intensity increases significantly with increasing temperature). Moreover, it retains the temperature sensitivity regardless of the laser irradiance while some fluorescent dyes lose some of their temperature sensitivity at high laser irradiance, like rhodamine B [96]. Sulforhodamine B sodium (SRB) is another dye used in this work which has a negative temperature sensitivity compared to FL (as shown in Figure IV-1, KR in the legend is SRB). The use of two dyes with opposite temperature sensitivity can improve the accuracy of the measurement as presented in Chapter I. Moreover the absorption and emission spectra of SRB are red-shifted which can reduce the spectra conflicts in the two-dyes approach, problem mentioned by Coppeta and Roger [114].

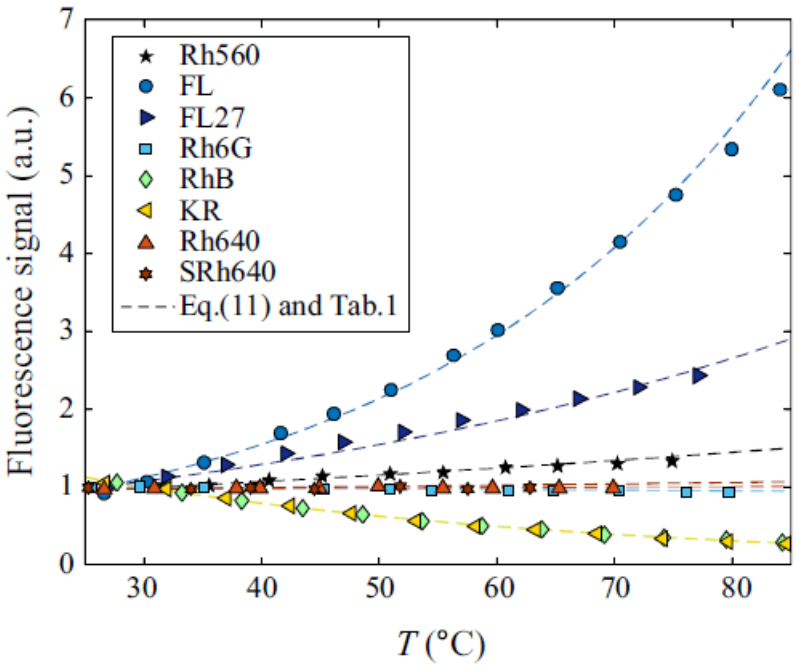

Figure IV-1: Variation in the fluorescence signal as a function of the temperature for different dyes where KR is SRB in the legend [115]

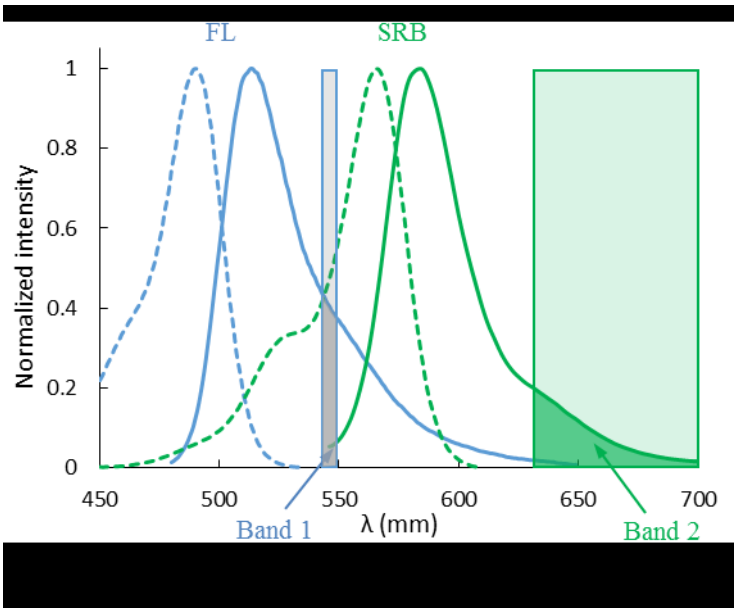

Figure IV-2: Detection bands used for the 2cLIF technique with the dye couple FL/SRB

To avoid the use of a light source with a large spectral emission band that may also cause spectra conflicts and complicate data analysis, the two dyes should have a common spectral band of absorption. The optimal wavelength to excite both dyes should be in the range 470 – 520 nm (in Figure IV-2). However, a laser that emits at 532 nm has been used because of its availability at the LGC. Therefore, as described afterwards, the concentration of FL in the experiment is much higher than that of SRB because of its relatively low intensity of absorption at such wavelength. Finally, the detection bands (2 colors) may be adequately chosen to improve the accuracy of the method. The two detection bands used in the experiment are (as showed in Figure IV-2):

- Band 1 [543-549 nm]: FL has a predominant contribution in this band. SRB has some contribution as well, but as its concentration is very low compared to FL, its contribution can be neglected. Fluorescence is partially absorbed by SRB (ε=80000 $M^{-1}.m^{-1}$).

- Band 2 [>633 nm]: The emission of SRB is predominant. The emission of FL is not totally negligible and its contribution depends on the respective concentration of the dyes.

Neglecting the emission and absorption by SRB in band 1 and the emission of FL in band 2, the ratio *R* of the fluorescence signals in these two detection bands can be determined, based on equation IV-2.

$$R = \frac{dF_1}{dF_2} \propto \frac{\varepsilon_{0,FL}}{\varepsilon_{0,SRB}} \frac{C_{FL}}{C_{SRB}} R_{sat} \quad \text{(IV-2)}$$

where $R_{sat} = \frac{1+I_0/I_{sat,SRB}}{1+I_0/I_{sat,FL}}$. The quantities like η and ε_0 do not depend on dyes, they are only related to the laser. Experiments are carried out in the partially saturation regime of excitation ($I_0 \approx I_{sat}$), giving R_{sat} ≈1 where $I_{sat,SRB}$ is close to $I_{sat,FL}$ [115]. Chaze et al. [96] verified experimentally that *R* does not vary significantly with I_0 including in the partially saturated domain of excitation.

In this work, a reference temperature (T_0) is needed for the temperature measurement and the fluorescence ratio *R* at one temperature will be normalized to that at the reference temperature. Based on the normalized ratio, the temperature calibration at one plan of one zigzag channel can be directly applied to other plans and other channel geometries. This can avoid the repeating work of temperature calibration at each plan observed and each prototype studied. The normalized method can also get rid of potential disturbance effects on the fluorescence signal such as prototype surface defaults, optical reflection at different locations in the channels, etc. In the experiment, the calibration is carried out at one plan in the zigzag channel of 4 mm width. The normalized fluorescence ratio at one temperature *T* can be expressed as:

$$R_{normalized} = \frac{R}{R_0} = \frac{\varepsilon_{0,FL}(T)}{\varepsilon_{0,SRB}(T)} \frac{\varepsilon_{0,SRB}(T_0)}{\varepsilon_{0,FL}(T_0)} = \mathrm{f}(T) \quad \text{(IV-3)}$$

where f is the calibration function, the temperature then can be deduced by:

$$T = f^{-1}\left(\frac{R}{R_0}\right) \quad \text{(IV-4)}$$

In this work, the reference temperature T_0 is chosen at 24.9 °C.

2. Materials

2. 1 Chemicals

The chemicals used in this experiment are: fluorescein sodium technical (FL, VWR International SAS, CAS: 518-47-8); sulforhodamine B sodium salt (SRB, Alfa Aesar, CAS:

3520-42-1); carbonate buffer (pH=10, Acros Organics BVBA). The dye solutions are prepared with demineralized water.

In the experiment, 5µmol.L^{-1} of SRB solution and 0.2 mmol.L^{-1} of FL solution (400 mL demineralized water + 100 mL carbonate buffer) are prepared. The two solutions (500 mL for each) are mixed together during the experiment, their pH is measured at about 10 which makes sure that all the fluorescent molecules are in basic form.

2.2 Experimental prototypes and channel geometries

The prototypes are the three with zigzag channels which have been studied in Chapter II. All their information like materials, geometry parameters of the channels, etc. can be found in part 1.1 in Chapter II. The geometry parameters of zigzag channels in the process plates and of the straight channels (same for three prototypes) in utility plates are summarized in Table IV-1

Table IV-1: Geometry parameters of zigzag channels in process plates and straight channels in utility plates (*L* is total developed channel length)

	d_h (mm)	R_c (mm)	(°)	L_s (mm)	L (mm)
Zigzag channel	2	1.5	90	7	778
Zigzag channel	3	2.25	90	7	759
Zigzag channel	4	3	90	7	747
Straight channel	8 (12×6 mm²)	-	-	-	588

2.3 Experimental setup

The experimental setup is the same as presented in part 1.2 of Chapter II. For each prototype, the process plate is connected to a magnetic drive pump (0 - 100 L.h^{-1}) and the utility plate is connected to a centrifugal pump (0 - 1000 L.h^{-1}). The process fluid (fluorescence solution) is heated by a thermostated bath through a heat exchanger before entering the prototype. 4 thermocouples are used to measure the inlet and outlet temperature of the two plates.

A pulsed Nd:YAG laser at 532 nm (Litron Lasers, Nano L 120-20 PIV, pulse energy E= 60 mJ, pulse duration dt = 6 ns) is used in this work for the excitation of the fluorescent molecules. The laser beam is about 500 µm of width. The pulsation frequency of the laser is 10 Hz. The fluorescence is detected by two CCD cameras (PC, 1376x1040 pixels, 10 Hz, 12 bits) which are placed above the prototype and synchronized with the laser. The two cameras are equipped

with two different interference filters to separately obtain the fluorescence signals emitted in the two bands of interest as shown in Figure IV-3. The optical detection system is based on a binocular microscope (Leica, M651) with an objective lens which can detect the fluorescence signal. There are two tubes over the objective lens to support the two cameras. The fluorescence signals detected by the cameras are registered by a computer with the software Camware from PCO company (German). The cameras and the computer are from the regional research federation FERMAT (Midi-Pyrénées).

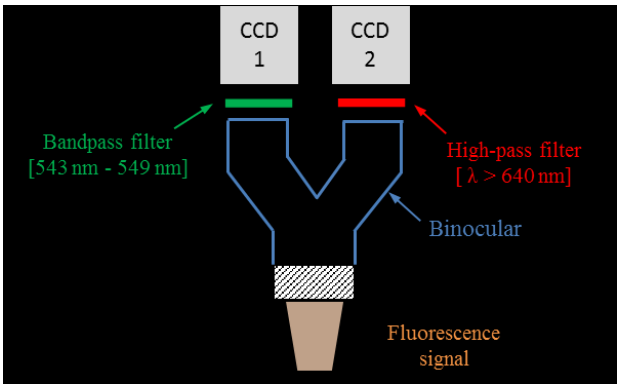

Figure IV-3: Optical detection system

The optical system is schematized in Figure IV-4. An optical barrier consisting of a laser diode is placed after the prototype, at the same level as the zigzag channel in the process plate. The height of the prototype and its transverse position can be adjusted during the experiment while the laser beam and detection system are fixed. With the moving system, the fluorescence signal at different longitudinal positions and different height levels inside the zigzag channel can be detected. With this optical system, the observed plan is parallel to the top face of the prototype.

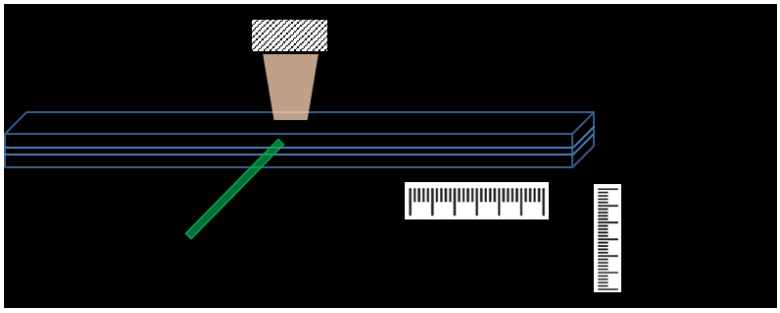

Figure IV-4: Optical system for the visualization of fluorescence emission in the zigzag channel

3. Method

3.1 Temperature calibration experiment

The calibration is carried out near (about 0.01m) the entrance of process plate with zigzag channel of 4 mm width. The zone observed is in the middle of the channel (2 mm from the below edge). The flow rate of the fluorescent solution is 4 $L.h^{-1}$ with no fluid introduced in the utility channel. The inlet and outlet temperatures of the process fluid are measured by thermocouples. During the experiment, the maximum difference between inlet and outlet temperatures is 0.5 °C, the inlet temperature therefore can be considered as the temperature of the zone observed. For the calibration experiment, the fluorescent solution enters the process channel at the temperature ranging from 17 °C to 60 °C (as shown in Table IV-2), where 24.9 °C is taken as the reference temperature since it is close to room temperature which is easier to keep for all the fluorescence experiment. For each temperature, 100 fluorescence images are taken and registered once thermal equilibrium is reached.

Table IV-2: Inlet temperatures of fluorescent solution for the calibration experiment

***T* (°C)**	17.5	24.9	30.3	36.7	42.7	49.5	52.5	55.9	58.8

3.2 Temperature measurement in heat transfer experiment

In heat transfer experiment, the fluorescent solution is heated at about 60 °C before entering the process channel. Two flowrates of fluorescence solution are studied for the three prototypes, corresponding to Reynolds number of around 500 and 650. In the utility channel, water at ambient temperature is introduced with a flowrate of 300 $L.h^{-1}$. The two fluids circulate cocurrently. For each prototype, measurements at three longitudinal positions of zigzag channel are carried out. For each position, the fluorescence of one to three plans corresponding to different heights is detected, depending on the channel width. All the plans measured are presented in Table IV-3. For all the measurements, 500 images are taken and registered once heat transfer equilibrium is reached (overall heat transfer coefficient is constant with time).

Table IV-3: Plans measured during heat transfer for three zigzag channels with two Reynolds numbers (plan heights are relative to the bottom edge of the channel)

Zigzag channel 4 mm						
Re	503			695		
Locations (m)	0.034	0.069	0.138	0.045	0.092	0.175
Plans						
High plan	3 mm	3 mm	3 mm	3 mm	3 mm	3 mm
Medium plan	2 mm	2 mm	2 mm	2 mm	2 mm	2 mm
Low plan	1 mm	1 mm	1 mm	1 mm	1 mm	1 mm

Zigzag channel 3 mm						
Re	494			685		
Locations (m)	0.029	0.050	0.103	0.030	0.071	0.134
Plans						
High plan	2.25 mm	2.25 mm	2 mm	2 mm	2 mm	2 mm
Medium plan	1.5 mm	1.5 mm	1.5 mm	1.5mm	1.5 mm	1.5 mm
Low plan	0.75 mm	0.75 mm	1 mm	1 mm	1 mm	1 mm

Zigzag channel 2 mm						
Re	461			631		
Locations (m)	0.0237	0.0425	0.1075	0.0331	0.0518	0.1075
Plans						
Medium plan	1 mm	1 mm	1 mm	1 mm	1 mm	1 mm

The fluorescence signal of all the plans measured at reference temperature (24.9 °C) is also detected and 100 images are registered, with just passing the fluorescent solution in process plate and inlet temperature of 24.9 °C (without heat transfer).

3.3 Image processing

3.3.1 Image registration between two cameras

Two images observed simultaneously by two cameras in the zigzag channel of 4 mm width are shown in Figure IV-5. It can be seen that the zone observed by the two cameras is not the same. It is due to the slight angular offset of the two optical axes of the binocular microscope which slightly deviate the light trajectory. Therefore a mathematical method is first implemented to superimpose the two images (by translation and rotation) to obtain a common observation area (code developed and launched in Matlab). A matrix is obtained by calculating the affine transform function between these two images which uses the normalized cross-correlation to adjust each pair of control points of the two images. The effects of the image vignetting and the background noise to the grey scale of the image are taken into account, since the zone observed by two cameras is different. With this matrix, the fluorescence signal ratio (in terms of grey level ratio) between the two cameras at each pixel can be calculated.

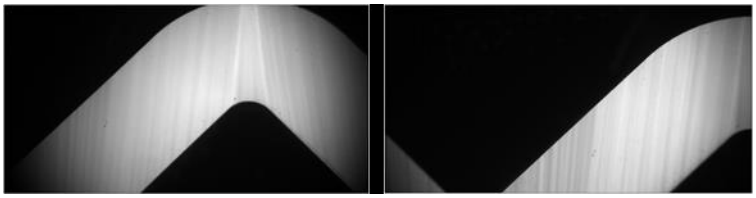

Figure IV-5: Fluorescence images simultaneously observed by two cameras in the zigzag channel of 4 mm width

3.3.2 Image registration between an experiment and that at the reference temperature

In the experiment, as the prototype moves slightly with time, the zone observed moves a little actually. Thus, another image registration is needed as the fluorescence signal ratio will be normalized with that at the reference temperature (24.9 °C). For a given plan, the zone observed for each experiment (calibration or heat transfer) are repositioned to that at 24.9 °C by another matrix which is obtained by calculating the affine transform functions between the image taken at the reference temperature and that taken at other temperature for the temperature calibration (and that taken in heat transfer for heat transfer experiment). With this matrix (different for each case), the fluorescence signal ratio can be normalized to that at the reference temperature.

4. Results

4.1 Temperature calibration

4.1.1 Calibration equation

The fluorescence ratio *R* is calculated by dividing its grey level of the two images taken by two cameras. This is done for all the pixels of the common zone, and for all the calibration experiments at different temperature. The ratio *R* obtained at other temperature is normalized to that obtained at the reference temperature (24.9 C°). A calibration equation for each pixel then can be obtained with a series of normalized ratio values and the corresponding temperature, using an exponential regression of the normalized ratio as a function of the temperature:

$$R_{normalized} = \frac{R}{R_0} = \mathrm{f}(T) = a \cdot \mathrm{e}^{bT} \qquad \text{(IV-5)}$$

The coefficients *a* and *b* are calculated for all the pixels (i = 0-1376, j = 0-736). The calibration curve at the pixel (1000, 500) is presented in Figure IV-6. The coefficients of calibration calculated at this pixel are: a=0.4499, b=0.0323. It can be seen that the calibration equation fits well with the experimental data.

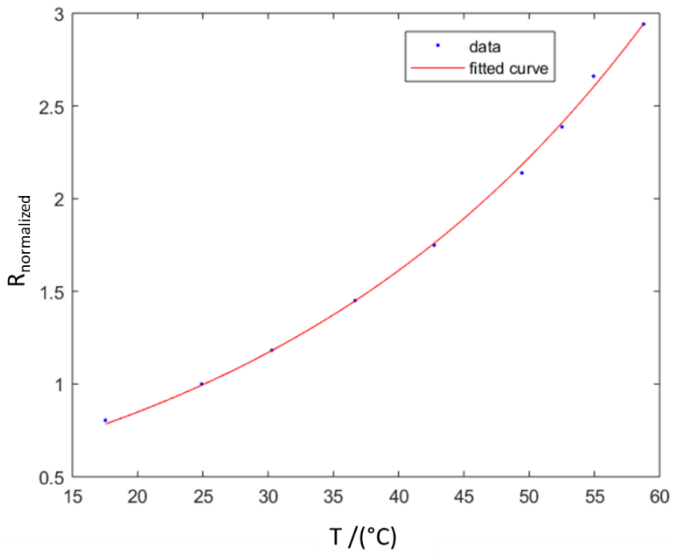

Figure IV-6 : Calibration curve at the pixel (1000, 500)

Then, a calibration equation expressed with coefficients of median values (a_m, b_m) is applied to all the pixels for simplifying the calculation, where a_m = 0.4441 and b_m = 0.0326. The distributions of *a* and *b* are shown in Figure IV-7. It can be seen that the distributions of coefficients *a* and *b* are narrow, with a range of ±0.05 for *a* and ±0.003 for *b* and a standard error of 0.28 for a and of 0.006 for b. So it should be well approximated to use the calibration equation with the median values for all the temperature calculation. The calibration equation based on coefficients of median values is presented in equation IV-6. This equation is applied to the calculation of all the temperature measurement for the three prototypes.

a b

Figure IV-7: Distribution of coefficients a and b in calibration equation for all pixels

$$R_{normalized} = \mathrm{f}(T) = 0.4441 \cdot \mathrm{e}^{0.0326T} \quad \text{(IV-6)}$$

4.1.2 Calibration verification

The temperature measurement at a high plan (3 mm) between the 5th and 6th bend (0.059 m from the entrance) in the zigzag channel of 4 mm width is carried out with only introducing the fluorescent solution in the process channel at three temperatures (without heat transfer): 24.9 °C, 36.4°C, 49.2 °C, which can be considered as the temperature at the zone observed as the difference of inlet and outlet temperatures is small (3 °C for 49.2 °C). 100 images of fluorescence signal are registered once steady state is reached. The fluorescence signal ratio *R* for the three temperature is calculated. *R* at 36.4°C and 49.2 °C is normalized with that obtained at 24.9 °C (the reference temperature). The temperature field at these two temperatures is furtherly deduced using the calibration equation (as shown in Figure IV-8), the flow goes from right to left in the figure. As expected, the temperature field of the zone observed is fairly homogeneous for these two temperatures. The mean temperature calculated from these two fields are 37.0 °C and 50.1 °C with standard deviations of 0.2°C and 0.3°C. The differences between the temperature measured by LIF technique and measured by the thermocouple (at the inlet) are 0.6°C for 36.4°C and 0.9°C for 49.2 °C, showing the good reliability of the calibration equation.

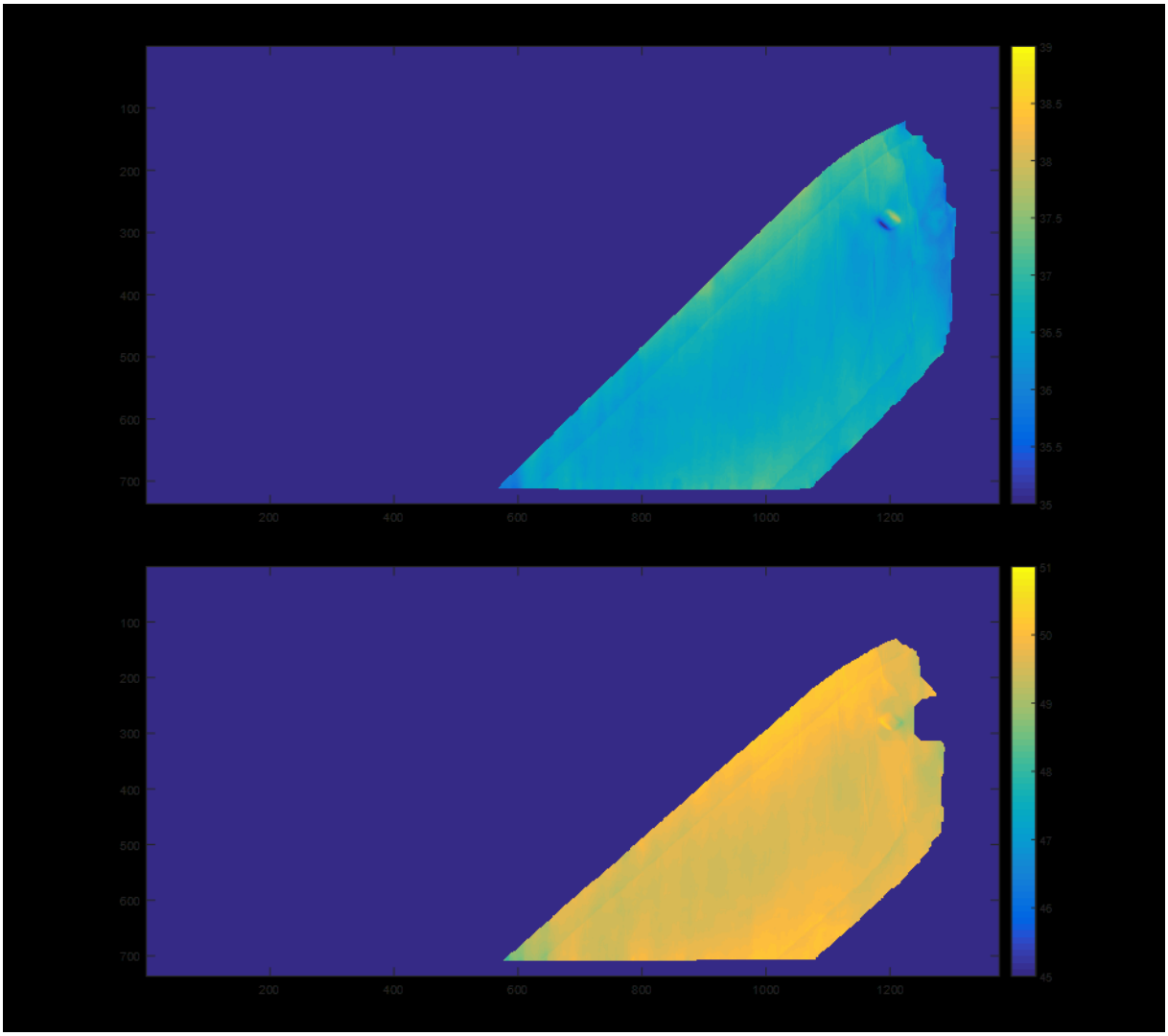

Figure IV-8:Temperature field of a high plan (0.059 m) in the zigzag channel of 4 mm width with inlet temperature of (a) 36.4°C and (b) 49.2 °C. Flow circulates towards the left.

4.2 Temperature measurement in heat transfer experiment

The fluorescence ratio *R* for all plans measured in heat transfer experiment is calculated and normalized to that at the reference temperature (24.9 °C) without heat transfer. The temperature field can be obtained with the calibration equation. Here an example of temperature field obtained is presented, as shown in Figure IV-9, which is the low plan (1 mm) at the location of 0.034 m in the zigzag channel of 4 mm width. The mean temperature of the zone observed is 51.8 °C with a standard deviation of 1.2 °C. As expected, it can be seen that the temperature field with heat transfer is less homogenous than that without heat transfer (compared with Figure IV-8).

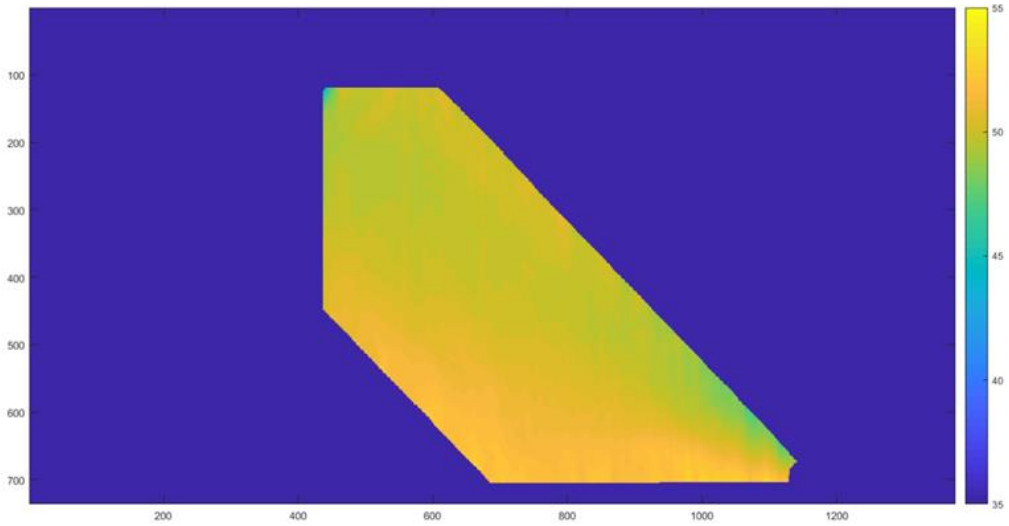

Figure IV-9: Temperature field of a low plan at the location of 0.034 m in the zigzag channel of 4 mm width with *Re* = 503. Flow circulates towards the left.

The temperature fields for all plans measured in three zigzag channels are obtained, the mean temperature ($T_{p,m}$) for all plans is calculated as well, which is presented in Table IV-4. The inlet and outlet temperatures of process fluid ($T_{p,in}$, $T_{p,out}$), inlet temperature of utility fluid ($T_{u,in}$) for the measurement at each location are also presented in this table. They are the mean value of the three plans for a given location except for zigzag channel of 2 mm width where only one plan is measured at one location.

Table IV-4: Mean temperature of all plans measured in three zigzag channels by the LIF technique

(a) Zigzag channel 4 mm, *Re* = 503

Location		$T_{p,m}$ **(°C)**		$T_{p,in}$	$T_{p,out}$	$T_{u,in}$
(m)	**High plan**	**Medium plan**	**Low plan**	**(°C)**	**(°C)**	**(°C)**
0.034	52.2	53.1	51.8	56.9	28.3	18.9
0.069	55.2	50.1	51.1	56.9	28.5	19.5
0.138	49.4	46.6	47.0	56.9	29.6	21.1

(b) Zigzag channel 4 mm, *Re* = 695

Location		$T_{p,m}$ **(°C)**		$T_{p,in}$	$T_{p,out}$	$T_{u,in}$
(m)	**High plan**	**Medium plan**	**Low plan**	**(°C)**	**(°C)**	**(°C)**
0.045	53.4	53.6	52.6	57.5	35.6	27.0
0.092	54.5	51.4	49.5	57.5	33.3	23.6
0.175	47.4	47.2	45.0	57.4	32.1	22.0

(c) Zigzag channel 3 mm, *Re* = 494

Location		$T_{p,m}$ **(°C)**		$T_{p,in}$	$T_{p,out}$	$T_{u,in}$
(m)	**High plan**	**Medium plan**	**Low plan**	**(°C)**	**(°C)**	**(°C)**
0.029	51.0	50.5	50.9	56.2	26.1	19.7
0.050	50.1	49.2	49.8	56.4	28.4	22.8
0.103	46.8	46.5	46.3	56.4	28.6	23.1

(d) Zigzag channel 3 mm, *Re* = 685

Location		$T_{p,m}$ **(°C)**		$T_{p,in}$	$T_{p,out}$	$T_{u,in}$
(m)	**High plan**	**Medium plan**	**Low plan**	**(°C)**	**(°C)**	**(°C)**
0.030	52.4	52.5	52.1	57.1	33.0	25.5
0.072	49.7	49.7	50.2	57.0	31.7	25.1
0.134	46.4	46.0	46.2	57.1	30.8	23.6

(e) Zigzag channel 2 mm, *Re* = 461

Location		$T_{p,m}$ **(°C)**		$T_{p,in}$	$T_{p,out}$	$T_{u,in}$
(m)	**High plan**	**Medium plan**	**Low plan**	**(°C)**	**(°C)**	**(°C)**
0.024	-	47.9	-	54.7	21.9	18.2
0.043	-	46.3	-	54.6	22.0	18.3
0.108	-	41.5	-	54.7	22.6	18.9

(f) Zigzag channel 2 mm, *Re* = 631

Location		$T_{p,m}$ **(°C)**		$T_{p,in}$	$T_{p,out}$	$T_{u,in}$
(m)	**High plan**	**Medium plan**	**Low plan**	**(°C)**	**(°C)**	**(°C)**
0.033	-	49.4	-	55.7	26.5	22.0
0.052	-	47.8	-	55.7	26.2	21.7
0.108	-	43.8	-	54.8	22.7	19.0

As an example, for the experiment at the location x = 0.103 m in the zigzag channel of 3 mm width with *Re* = 494, the inlet temperatures of the process fluid and the utility fluid are 56.4 °C and 23.1 °C, the outlet temperatures are 28.6 °C and 23.7 °C. The mean temperatures of the process fluid at the three plans (high, medium and low) measured by LIF are 46.8 °C, 46.5 °C and 46.3 °C. As expected, they are between the inlet and the outlet temperature. For a given channel, it can be observed that the mean temperature decreases when the location is away from the entrance. This is normal, because the process fluid is hot and cooled by a cold fluid, so the temperature far from the entrance is lower.

Among the three plans at one location, the low plan is closest to the cold fluid. However, it is not always the coldest, as can be seen for the data obtained in zigzag channels of 3 mm and 4 mm width. This can be explained by the presence of the Dean vortices which can generate tangential mixing. It can also be observed that the temperature varies more significantly from high plan to low plan for d_h = 4 mm than for d_h = 3 mm, indicating the temperature on the cross-section is more homogeneous when the channel width decreases. This is consistent with the results presented in Chapter II, where it has been observed an increase of the heat transfer coefficient in the zigzag channel when the hydraulic diameter decreases for same Reynolds number.

To conclude, the general trends observed tend to validate the consistency of the local thermometry method based on LIF technique with 2 dyes / 2 colors. However, because the inlet temperature of two fluids is not the same for each experiment, it is difficult to do more direct analysis for the results. In order to furtherly evaluate the reliability of this method, a heat transfer model is introduced which can estimate the local temperature of process fluid, it is then compared to the temperature obtained by LIF technique.

4.3 Comparison between temperature calculated with LIF and heat transfer model

The 1D heat transfer model can be expressed as follows (for process fluid):

$$u_p \rho_p c_{P,p} \frac{dT_{p,x}}{dx} = \frac{U dA(T_{u,s} - T_{p,x}) - U_l dA(T_{p,x} - T_{air})}{dV_p} \quad \text{(IV-7)}$$

where u_p, ρ_p and $c_{P,p}$ are the velocity, density and specific heat capacity of the process fluid respectively. $T_{p,x}$ is the mean temperature at the location *x* of the process fluid and $T_{u,s}$ is the mean temperature at location *s* of utility fluid (Figure IV-10). As the channel lengths of two plates are different (process plate and utility plate), in order to calculate the temperature, the reference location for two channels should be the same. Therefore, a transformation is needed which is presented as:

$$s = \frac{x L_u}{L_p} \quad \text{(IV-8)}$$

where $L_p$and L_u are the lengths of the process channel and the utility channel.

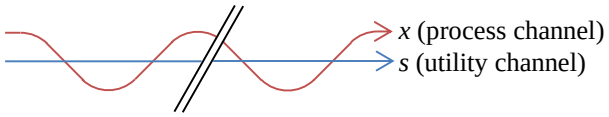

Figure IV-10: Illustration of the axial coordinates in the process and utility channels

T_{air} is the temperature of air and it is taken at 20 °C. dA and dV_p are the elementary heat transfer area and the elementary volume of process fluid corresponding to the channel length element *dx*. *U* is the overall heat transfer coefficient of the prototype and U_l is the heat transfer coefficient relative to the heat loss, which is calculated from a prior experiment with no utility fluid:

$$U_l = \frac{q_l}{\mathrm{A}\Delta T_{ml,l}} = \frac{\dot{m}_p C_{P,p} \Delta T_{p,l}}{\mathrm{A}\Delta T_{ml,l}} \quad \text{(IV-9)}$$

where q_l is the global heat loss. $\Delta T_{ml,l}$ is calculated as

$$\Delta T_{ml,l} = \frac{(T_{p,in} - T_{air}) - (T_{p,out} - T_{air})}{\ln(\frac{T_{p,in} - T_{air}}{T_{p,out} - T_{air}})} \quad \text{(IV-10)}$$

where $T_{p,in}$ and $T_{p,out}$ are the inlet and outlet temperature measured during the heat loss experiment.

For the utility fluid, there is a similar equation to calculate the temperature:

$$u_u \rho_u c_{P,u} \frac{dT_{u,s}}{ds} = \frac{UdA}{dV_u}\left(T_{p,x} - T_{u,s}\right) \quad \text{(IV-11)}$$

where u_u, ρ_u and $c_{P,u}$ are the velocity, density and specific heat capacity of the utility fluid respectively. dV_u is the elementary volume of utility fluid corresponding to the channel length element *ds*. The thermal loss in the utility side is neglected since its temperature is close to room temperature and the temperature difference between inlet and outlet is less than 1°C during the experiment. Finally, the overall heat exchange coefficient is calculated from the inlet out outlet temperatures measured by the thermocouples:

$$U = \frac{q}{\mathrm{A}\Delta T_{ml}} = \frac{\dot{m}_p C_{P,p} \Delta T_p}{\mathrm{A}\Delta T_{ml}} \quad \text{(IV-12)}$$

$$\Delta T_{ml} = \frac{\left(T_{p,in} - T_{u,in}\right) - \left(T_{p,out} - T_{u,out}\right)}{\ln\left(\frac{T_{p,in} - T_{u,in}}{T_{p,out} - T_{p,out}}\right)} \quad \text{(IV-13)}$$

The temperatures of process fluid and utility fluid can be deduced from equations IV-7 and IV-11, which is expressed as:

$$T_{p,x+\mathrm{d}x} = T_{p,x} + \left(\frac{UdA}{dV_p}\left(T_{u,s} - T_{p,x}\right) - \frac{U_l dA}{dV_p}\left(T_{p,x} - T_{air}\right)\right)\frac{\mathrm{d}x}{u_p \rho_p c_{p,p}} \quad \text{(IV-14)}$$

$$T_{u,s+\mathrm{d}s} = T_{u,s} + \frac{UdA}{dV_u}\left(T_{p,x} - T_{u,s}\right)\frac{\mathrm{d}s}{u_u \rho_u c_{p,u}} \quad \text{(IV-15)}$$

Based on these equations above, the temperatures of process fluid and utility fluid at different locations can be calculated by an iterative differential method using the two equations alternately with inlet temperature of two fluids (where $x = s = 0$). The temperature profiles of process fluid and utility fluid can be obtained finally. The local mean temperature calculated with the LIF technique is then compared to that deduced by the heat transfer model.

The temperature profiles of process fluid and utility fluid calculated with heat transfer model in the prototype with zigzag channel of 3 mm width at *Re* = 494 is presented, as shown in Figure IV-11. For the measurement at location $x = 0.103$ m, the inlet temperatures of process fluid and utility fluid are 56.4 °C and 23.1 °C. It should be noted that the two inlet temperatures are different for the measurement at different location, so the calculation is done for each location with corresponding inlet temperatures of two fluids. In the heat transfer model, the mean value of *U* at three locations for one Reynolds number is taken for the calculation where for each location, U can be calculated with inlet temperature and outlet temperatures of two fluids using

equation IV-12. The heat loss for process fluid is measured at 16.3 W for *Re* = 494 by just introducing the process fluid, the inlet and outlet temperatures are measured at 57.2 °C and 52.9 °C. With heat transfer model, the outlet temperature of process fluid and the utility fluid are estimated at 28.5 °C and 23.4 °C where in the experiment they were measured at 28.6 °C and 23.7 °C, showing the good reliability of the model for the temperature estimation. The three locations of temperature measurements by LIF technique are marked in this figure as well, corresponding to 0.029 m, 0.050 m and 0.103 m, where the mean temperature estimated by the heat transfer model are 54.2 °C, 52.6 °C and 49.1 °C respectively. However, as mentioned before, the inlet temperatures of process fluid and utility fluid are different for different locations, the temperatures estimated at 0.029 m, 0.050 m (54.2 °C, 52.6 °C) are not considered. They need to be simulated with the inlet temperatures at these two locations.

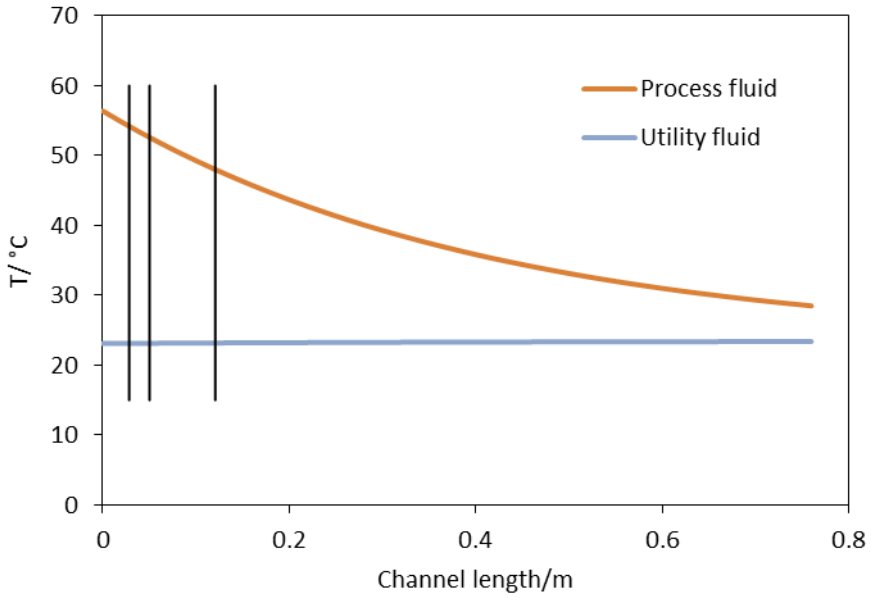

Figure IV-11: Temperature profiles of the process fluid and the utility fluid calculated with heat transfer model in the prototype with the zigzag channel of 3 mm width at *Re* = 494 (the black lines are the locations of temperature measurement by LIF technique)

The temperatures estimated by the heat transfer model (T_{mod}) at three locations in three zigzag channels with two Reynolds numbers, are presented in Table IV-5. The mean temperature of all the plans calculated from the experiment is also presented. It can be observed that the experimental measurements are generally in agreement with the model for the zigzag channel of 4 mm width. The temperature difference obtained from experiment and the model gets higher when the channel width decreases, maybe due to the calibration method. The calibration

equation was obtained in the zigzag channel of 4 mm width and directly applied to the measurement in zigzag channels of 3 mm and 2 mm width. This may bring some errors for the temperature calculation, although it was thought that the normalization of the fluorescence signal ratio to that at the reference temperature is sufficient for taking the channel geometry into account. To confirm this hypothesis, the temperature calibration needs to be done in zigzag channels of 3 mm and 2 mm width although it takes much more time. Another explanation can rely in the dye solution. The experiments have been firstly carried out in the prototype with the zigzag channel of 4 mm width (calibration and heat transfer experiments), then 3 mm and finally 2 mm width. The same solution was used to avoid the error related to the solution preparation since the fluorescence signal depends on the concentration of both dyes. However, evaporation probably occurred with experiment time as the solution was regularly heated up to 60 °C and the dye solution container was not hermetically sealed. Regular experiments for calibration check should be carried out to adjust the calibration equation.

Table IV-5: Temperatures calculated with LIF technique ($T_{p,m}$) and heat transfer model (T_{mod}). U_m is the mean value of heat transfer coefficient at three locations.

(a) Zigzag channel 4 mm with Re = 503 and U_m = 2320 W.K^{-1}.m^{-2}

Location		$T_{p,m}$ **(°C)**		T_{mod}
(m)	**High plan**	**Medium plan**	**Low plan**	**(°C)**
0.034	52.2	53.1	51.8	54.5
0.069	55.2	50.1	51.1	52.2
0.138	49.4	46.6	47.0	48.5

(b) Zigzag channel 4 mm with Re = 695 and U_m = 2730 W.K^{-1}.m^{-2}

Location		$T_{p,m}$ **(°C)**		T_{mod}
(m)	**High plan**	**Medium plan**	**Low plan**	**(°C)**
0.045	53.4	53.5	52.5	55.1
0.092	54.5	51.4	49.5	52.4
0.173	47.4	47.2	45.0	48.2

(c) Zigzag channel 3 mm with *Re* = 494 and U_m = 2860 W.K^{-1}.m^{-2}

Location		$T_{p,m}$ **(°C)**		T_{mod}
(m)	**High plan**	**Medium plan**	**Low plan**	**(°C)**
0.029	51.0	50.5	50.9	53.8
0.050	50.1	49.2	49.8	52.6
0.103	46.8	46.5	46.3	49.1

(d) Zigzag channel 3 mm with *Re* = 685 and U_m = 3350 W.K^{-1}.m^{-2}

Location		$T_{p,m}$ **(°C)**		T_{mod}
(m)	**High plan**	**Medium plan**	**Low plan**	**(°C)**
0.030	52.4	52.5	52.1	55.2
0.071	49.7	49.7	50.2	52.6
0.134	46.4	46.0	46.2	48.9

(e) Zigzag channel 2 mm with *Re* = 461 and U_m = 3700 W.K^{-1}.m^{-2}

Location		$T_{p,m}$ **(°C)**		T_{mod}
(m)	**High plan**	**Medium plan**	**Low plan**	**(°C)**
0.024	-	47.9	-	52.0
0.043	-	46.3	-	50.1
0.108	-	41.5	-	44.5

(f) Zigzag channel 2 mm with *Re* = 631 and U_m = 4260 W.K^{-1}.m^{-2}

Location		$T_{p,m}$ **(°C)**		T_{mod}
(m)	**High plan**	**Medium plan**	**Low plan**	**(°C)**
0.033	-	49.4	-	52.7
0.052	-	47.8	-	51.2
0.108	-	43.8	-	45.8

5. Conclusion

In this chapter, the local temperature measurement technique based on laser-induced fluorescence with two colors/two dyes is developed and applied to measure the fluid

temperature in millimetric zigzag channels during heat transfer. Temperature fields at different height levels and at different locations in three zigzag channels are obtained. As expected, it is observed that the temperature decreases with the channel length. Concerning the temperature over the cross-section, tangential fluid motion seems enough significant to create mixing as the temperature from the top of the channel to the bottom does not evidently decrease. Moreover, cross-sectional temperature appears to be more homogeneous in the zigzag channel of 3 mm width than in the zigzag channel of 4 mm width.

A heat transfer model is then introduced as a way to estimate the temperature in zigzag channels and to evaluate the consistency of the LIF technique. It is found that the temperature difference between the experiments and the model increases when the channel width decreases. This is probably because the temperature calibration is just done in zigzag channel of 4 mm and it is better to do it for the other two zigzag channels. The evaporation of the dye solution in the experiment may also influence the measurements. Regular experiments for calibration check should be carried out to adjust the calibration equation.

In terms of problems or improvements, firstly, as the width of the zigzag channels is very small (2 to 4 mm), to have a good temperature measurement at different height levels inside the channel, it is better to use a laser with a smaller beam width keeping the similar intensity (around 0.5 mm in the present work). Another problem is that during the experiment, the prototype moves a little with time so the zone observed moves as well, that is why an additional image processing is needed to adjust the zone observed at one operating condition to that at the reference temperature. The prototype was placed on the bench where there are equipment like pumps, thermostatic bath which can cause vibration, they should be placed on a distinct support.

It should finally be concluded that the thermometry by LIF technique with 2 dyes/2 colors present a good potential for local temperature measurement in millimetric channels although the measurement is sensible to the spatial disturbances due to the small channel size. Unlike thermocouples, it does not disturb the flow, provides immediate response that allows the detection of fast dynamic effects and presents a very high spatial resolution. The trends observed related to the measurement in the present work are very consistent and some improvements have been proposed to increase the accuracy of this method.

Chapter V: Study of heat transfer performance in compact HEX reactors with implementation of chemical reactions

The heat transfer performance of heat-exchanger reactor with millimetric channels is studied experimentally and numerically in the last three chapters. The heat transfer coefficient is characterized and a correlation of Nusselt number is established as a function of Reynolds number, fluid physicochemical properties and channel geometries. A new technique for local temperature measurement in millimetric channels based on Laser-Induced Fluorescence is developed in Chapter IV. With the aim of facilitating the industrial application of compact heat-exchanger reactors, the last chapter will introduce chemical reactions in heat-exchanger reactors studied before where the reactions occur in zigzag channels and evaluate their performances in terms of the conversion and selectivity for an exothermic competitive consecutive reaction scheme. The objective is to study the influence of heat transfer performance on the reaction (conversion and selectivity) in zigzag channels to illustrate the impact of scale-up for HEX reactors. A 1D model of plug flow is introduced and the influence of channel geometry in terms of hydraulic diameter on the temperature distribution, conversion rate and selectivity is discussed which is very useful for industrial applications of compact heat-exchanger reactors.

1. Chemical reaction

In this chapter, a competitive consecutive reaction scheme is studied which is presented as:

$$A + B \rightarrow R$$
$$B + R \rightarrow S \qquad \text{(V-1)}$$

where A and B are the reactants, R is the desired product and S is the undesired product (by-product). The reaction rates $r_1$and r_2 are calculated by:

$$r_1 = k_1 C_A C_B \qquad \text{(V-2)}$$

$$r_2 = k_2 C_B C_R \qquad \text{(V-3)}$$

where k_1 and k_2 are the reaction rate coefficients, which can be expressed as follows:

$$k_1 = k_{10}\, \mathrm{e}^{\frac{-E_1}{RT}} \qquad \text{(V-4)}$$

$$k_2 = k_{20}\, \mathrm{e}^{\frac{-E_2}{RT}} \qquad \text{(V-5)}$$

where k_{10}, k_{20}, E_1, E_2 are the frequency factors and activation energy of reaction 1 and 2. $\bar{R}$ is the universal gas constant ($\bar{R}$ = 8.314 J.mol^{-1}.K^{-1}).

Chemical reactions are influenced by many variables and in single liquid phase systems, composition, temperature, mixing and residence time distribution will determine the composition of the final products. In this chapter, the influence of inlet concentrations and utility temperature on the reaction rate and product distribution is discussed. The dataset of two reactions is presented in the following table. The physicochemical properties of process fluid where the reactions occur and of utility fluid presented here are at 20 °C. These data correspond to case studies proposed by Shelat et al. [116] who simulated different reaction schemes in HEX reactors with multiple injections of reactants.

Table V-1: Dataset for the two reactions

	Symbol	**Unit**	
Inlet concentration of reactant A	C_{A0}	mol.m^{-3}	
Inlet concentration of reactant B	C_{B0}	mol.m^{-3}	
Inlet concentration of product R	C_{R0}	mol.m^{-3}	0
Inlet concentration of product S	C_{S0}	mol.m^{-3}	0
Inlet temperature of the process fluid	T_{p0}	K	350
Density of the process fluid	ρ_p	kg.m^{-3}	1000
Viscosity of the process fluid	μ_p	Pa.s	1×10^{-3}
Heat capacity of the process fluid	$C_{p,p}$	J.kg^{-1}.K^{-1}	4184
Thermal conductivity of the process fluid	k_p	W.m^{-1}.K^{-1}	0.6
Activation energy for reaction 1	E_1	J.mol^{-1}	60000
Heat of reaction for reaction 1	ΔH_{r1}	J.mol^{-1}	-225000
Heat of reaction for reaction 2	ΔH_{r2}	J.mol^{-1}	-112500
Density of the utility fluid	ρ_u	kg.m^{-3}	1000
Viscosity of the utility fluid	μ_u	Pa.s	1×10^{-3}
Heat capacity of the utility fluid	$C_{p,u}$	J.kg^{-1}.K^{-1}	4184
Thermal conductivity of the utility fluid	k_u	W.m^{-1}.K^{-1}	0.6

Two reaction cases are studied in this chapter, one is the activation energy of the desired reaction larger than that of the undesired reaction ($E_1 > E_2$), where high temperature favors reaction 1. In the other case, the activation energy of the desired reaction is smaller than that of

the undesired reaction ($E_1 < E_2$), where high temperature favors reaction 2. They are presented in the following table.

Table V-2: Specific dataset for the two reaction cases studied

	Symbol	Unit	$E_1 > E_2$	$E_1 < E_2$
Frequency factor for reaction 1	k_{10}	$m^3.mol^{-1}.s^{-1}$	5×10^7	3.5×10^7
Frequency factor for reaction 2	k_{20}	$m^3.mol^{-1}.s^{-1}$	1.5×10^2	1.58×10^{20}
Activation energy for reaction 2	E_2	$J.mol^{-1}$	24000	150000

2. Simulation model

2.1 Geometry of HEX reactors

In this chapter, a steady state 1D plug flow model is used to simulate the competitive consecutive reaction scheme in heat-exchanger reactors with zigzag channels. The heat-exchanger reactors simulated are based on the ones studied in the Chapters II and IV. the geometry of zigzag channels in the process plate is exactly the same as before with a square cross-section of 2 mm, 3 mm and 4 mm width ($d_{h,p}$). With the consideration of industrial design, two utility plates with a straight channel engraved are used and put in the two sides of the process plate forming a sandwich. They are separated by two aluminum plates (1 mm thickness). For the simulation, the process fluid velocity is set at 0.7 $m.s^{-1}$, typical in millimetric channels. For each utility plate, the width of the channel (w_u) is the total width of one unit in zigzag channel (bend to bend), so the utility channel can completely cover the process channel. Assuming a utility fluid velocity of 1 $m.s^{-1}$ and a total flowrate 10 times larger than that of the process fluid, the depth of utility channel (d_u) then can be determined. The geometries of process channels and utility channels and the corresponding fluid flowrates are presented in the following table.

Table V-3: Geometries and flowrates for the simulation of HEX reactors

$d_{h,p}$ (m)	u_p ($m.s^{-1}$)	Q_p ($L.h^{-1}$)	Q_u ($L.h^{-1}$)	u_u ($m.s^{-1}$)	w_u (m)	d_u (m)	$d_{h,u}$ (m)
0.002	0.7	10.1	101	1	0.008	0.0018	0.0029
0.003	0.7	22.7	227	1	0.010	0.0032	0.0048
0.004	0.7	40.3	403	1	0.011	0.0051	0.0070

2.2 Assumptions

Before simulating the reaction, several assumptions have been made in this model. They are listed below:

1. The reactants are perfectly mixed at the inlet of HEX reactors and plug flow is assumed both in process channel and utility channels.
2. The influences of residence time distribution and mixing to the reaction are not taken into account.
3. Concentration and temperature gradients in the radial direction in zigzag channel and straight channel are assumed as zero.
4. The physicochemical properties of reactants and products are assumed to be the same, equal to those of water.
5. Fluid flowrates are supposed constant.
6. The heat loss in HEX reactors is assumed as zero.

2.3 Calculation of concentration and temperature

The temperatures of the process fluid and utility fluid are calculated with 1D thermal balances at steady state based on first order discretization on space:

$$u_p \rho_p c_{P,p} \frac{dT_{p,x}}{dx} = \frac{2U_x dA}{dV_p}\left(T_{u,s} - T_{p,x}\right) - \left(\Delta H_{r1} r_1 + \Delta H_{r2} r_2\right) \quad \text{(V-6)}$$

$$u_u \rho_u c_{P,u} \frac{dT_{u,s}}{ds} = \frac{U_x dA}{dV_u}\left(T_{p,x} - T_{u,s}\right) \quad \text{(V-7)}$$

Since the process plate is surrounded by two utility channels, the total heat exchange area of the process channel is twice the surface of one side *dA*:

$$dA = dA_p = d_{h,p} d\mathrm{x} \quad \text{(V-8)}$$

From these equations, the temperatures in process channel and utility channels of HEX reactor can be deduced:

$$T_{p,x+dx} = T_{p,x} + \left(\frac{2U_x dA}{dV_p}\left(T_{u,s} - T_{p,x}\right) - \left(\Delta H_{r1} r_1 + \Delta H_{r2} r_2\right)\right)\frac{dx}{u_p \rho_p c_{P,p}} \quad \text{(V-9)}$$

$$T_{u,s+ds} = T_{u,s} + \frac{U_x dA}{dV_u}\left(T_{p,x} - T_{u,s}\right)\frac{ds}{u_u \rho_u c_{P,u}} \quad \text{(V-10)}$$

These two equations are similar to that used in Chapter IV (equations IV-14 and IV-15) for estimating the local temperature with comparison to that measured by fluorescence, with just

introducing the reaction term in the calculation of process fluid. The overall heat transfer coefficient U_x can be calculated by

$$\frac{1}{U_x dA} = \frac{1}{h_{p,x} dA_p} + \frac{e_{Al}}{k_{Al} dA} + \frac{1}{h_{u,s} dA_u} \quad \text{(V-11)}$$

The heat transfer coefficient of the process fluid $h_{p,x}$ is calculated by the correlation (equation II-16) which has been established in Chapter II. The heat transfer coefficient of the utility fluid $h_{u,x}$ is calculated with the Gnielinski correlation (equation II-7). The density ρ, specific heat capacity C_p, Prandtl number P_r and viscosity μ of the process fluid and utility fluid at different temperatures can be calculated by the equations II-8 to II-7. The range of U_x calculated for each HEX reactor is presented in Table V-4. The U_xA/V in terms of process channels is also presented. Since the utility temperature in the simulation is different for two reaction cases (see next part), hence U_x for the same HEX reactor is different in two cases. It can be seen that U_x is generally the same for three HEX reactors, however, when process channels varies from 2mm to 4 mm, U_xA/V decreases greatly.

Table V-4: U_x and U_xA/V calculated in three HEX reactors for two reaction cases. "HEX reactor 2mm" represents HEX reactor with zigzag channel of 2mm width

	E1 > E2		**E1 < E2**	
	U_x ($W.m^{-2}.K^{-1}$)	U_xA/V ($kW.m^{-3}.K^{-1}$)	U_x ($W.m^{-2}.K^{-1}$)	U_xA/V ($kW.m^{-3}.K^{-1}$)
HEX reactor 2mm	7400-8000	3700-4000	6000-6500	3000-3250
HEX reactor 3mm	7000-7700	2333-2567	6000-6500	2000-2167
HEX reactor 4mm	6500-7000	1625-1750	5500-6100	1375-1525

The concentration of reactants and products in process plate is calculated by the following equations:

$$C_{A,x+\Delta x} = C_{A,x} - r_1 \Delta t = C_{A,x} - r_1 \frac{\Delta x}{u_p} \quad \text{(V-12)}$$

$$C_{B,x+\Delta x} = C_{B,x} - (r_1 + r_2) \frac{\Delta x}{u_p} \quad \text{(V-13)}$$

$$C_{R,x+\Delta x} = C_{R,x} + (r_1 - r_2) \frac{\Delta x}{u_p} \quad \text{(V-14)}$$

$$C_{S,x+\Delta x} = C_{S,x} + r_2 \frac{\Delta x}{u_p} \quad \text{(V-15)}$$

3. Results

The simulation of the model is carried out with Excel using the iterative solution method. With inlet reactant concentrations and process fluid and utility fluid temperatures, the concentration of the reactants and the products and the temperatures of the process and utility fluids at other locations can be deduced with all the equations presented above.

For the two reaction cases, two inlet concentrations are studied: $C_{A0} = C_{B0} = 300$ mol.m^{-3} with fast reaction rate and $C_{A0} = C_{B0} = 100$ mol.m^{-3} with relatively less fast reaction rate. The inlet temperature of the process fluid (T_{p0}) is fixed at 350 K for both cases.

3.1 Reaction case $E_1 > E_2$

For the reaction case $E_1 > E_2$, since temperature favors reaction 1 (desired reaction), it is better to keep a high temperature. So in this case, an inlet temperature of utility fluid (T_{u0}) at 350 K is considered. The concentrations of the desired product R, of the undesired product S and of the reactants A and B at different locations in the three zigzag channels are calculated with two initial concentrations of reactants (300 and 100 mol.m^{-3}). The concentration profiles in the zigzag channel of 2 mm width with inlet concentrations of 300 mol.m^{-3} are presented as an example (in Figure V-1). The concentration profiles in other channels and with inlet concentration of 100 mol.m^{-3} are similar, so here they are not presented. It can be seen that the reaction is very fast and that they are completed at the channel length of 0.2 m. The reactant B is totally consumed. The concentration of reactant A is equal to undesired product S at the end.

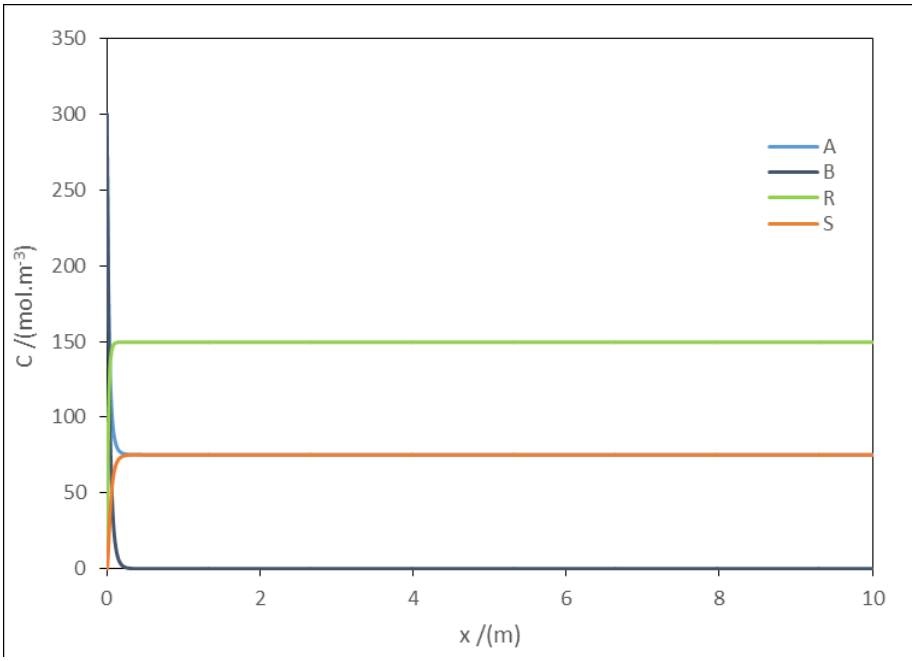

Figure V-1: Concentration profiles in the zigzag channel of 2 mm width, with C_{A0} = C_{B0} = 300 mol.m^{-3}

The temperatures of the process fluid and of the utility fluid in HEX reactor with the zigzag channel of 2 mm width with inlet concentrations of 300 mol.m^{-3} are shown Figure V-2. It can be seen as well from the temperature profile that the reaction is very fast. The temperature peak of the process fluid is where the reaction finishes. It is cooled rapidly by the utility fluid and reaches the same temperature as the utility fluid.

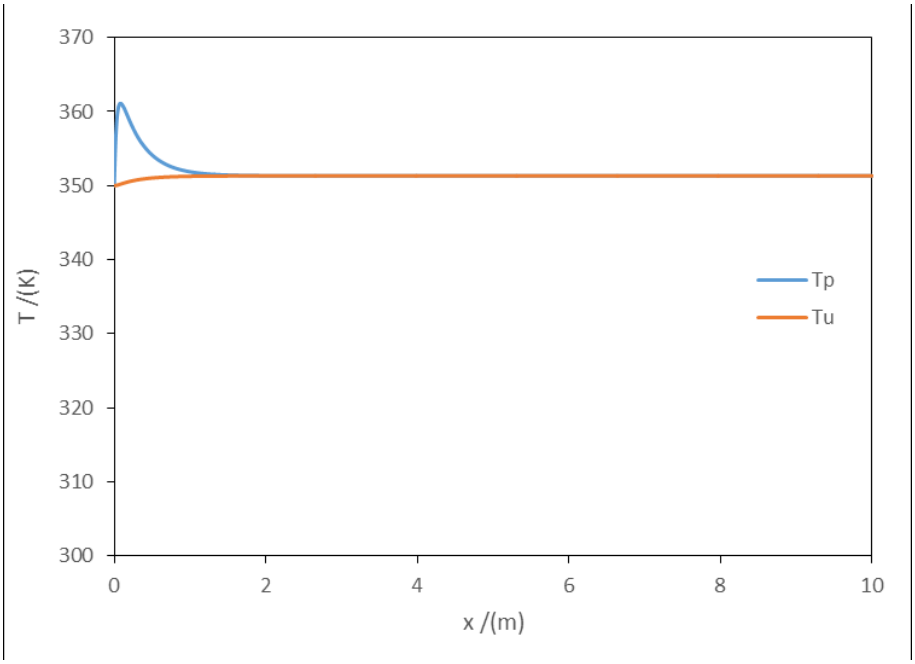

Figure V-2: Temperature profile of process fluid and of utility fluid in HEX reactor with zigzag channel of 2 mm and C_{A0} = C_{B0} = 300 mol.m^{-3}

The temperature profiles of process fluid in three zigzag channels for inlet concentration of 300 mol.m^{-3} are presented in Figure V-3. The temperature profiles of utility fluid in two other straight channels are not presented as they varies very little among the three channels and it is less interesting. In Figure V-3, the temperature peak increases with increasing the channel cross-section width. This is because the heat transfer performance (*UA*/*V*, as shown in Table V-4) decreases when the channel cross-section size increases: the heat produced by the reactions is transferred less efficiently to the utility fluid. This can be clearly seen after the peak, once the reactions are completed: the process fluid is cooled slowly when the channel cross-section size increases although the same temperature is reached at the end.

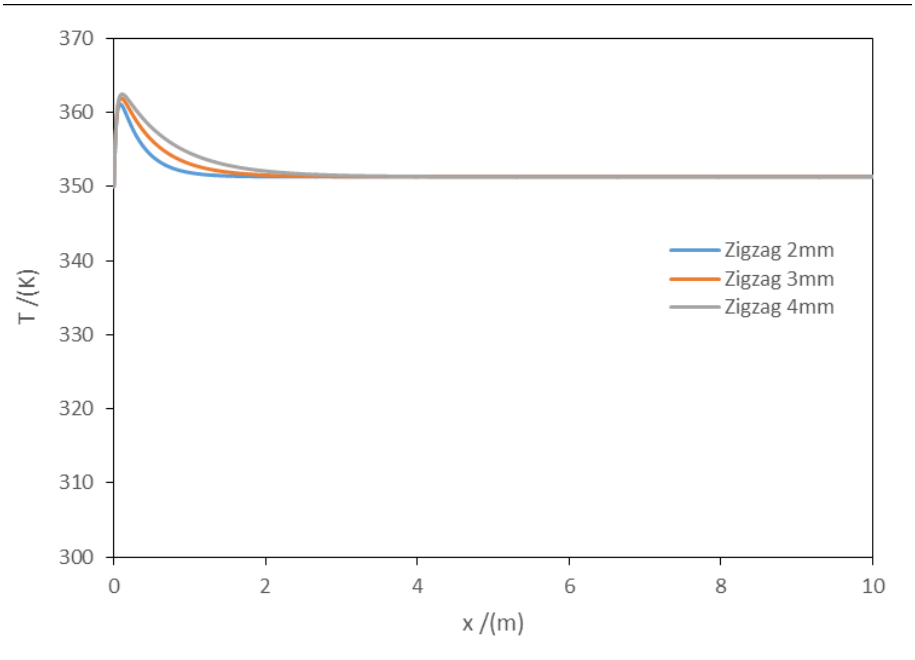

Figure V-3: Temperature profile of process fluid in three zigzag channels with C_{A0} = C_{B0} = 300 mol.m^{-3}

The difference between the temperature peak and the inlet temperature (ΔT_m) in the three zigzag channels for both initial reactant concentrations (300 and 100 mol.m^{-3}) is calculated and presented in Table V-5. The adiabatic temperature profile is also calculated by setting the overall heat transfer coefficient U_x = 0 in the simulation. The difference between outlet temperature and inlet temperature (ΔT_a) is presented in this table. The conversion of reactant A and the selectivity of desired product R in three zigzag channels are also presented in Table V-5. The conversion of A and the selectivity of R are calculated by the following equations:

$$Conversion = \frac{C_{A0} - C_{Ae}}{C_{A0}} \quad \text{(V-16)}$$

$$Selectivity = \frac{C_{Re}}{C_{Re} + C_{Se}} \quad \text{(V-17)}$$

where C_{Ae}, C_{Re} and C_{Se} are the concentrations of reactant A, desired product R and undesired product S at the end of the reactions.

Table V-5: Conversion, selectivity and maximal temperature difference with and without heat transfer (adiabatic) in three zigzag channels with two inlet concentrations

	$C_{A0} = C_{B0}$ = 300 mol.m^{-3}				$C_{A0} = C_{B0}$ = 100 mol.m^{-3}			
	Conversion of A	**Selectivity of R**	**ΔT_m (K)**	**ΔT_a (K)**	**Conversion of A**	**Selectivity of R**	**ΔT_m (K)**	**ΔT_a (K)**
Zigzag 2mm	74.9%	66.5%	11.1	14.5	72.4%	61.9%	2.6	14.8
Zigzag 3mm	75.1%	66.8%	11.9	14.5	72.5%	62.1%	3.0	14.8
Zigzag 4mm	75.2%	66.9%	12.5	14.5	72.6%	62.3%	3.3	14.8

From this table, it can be seen that the conversion of reactant A and the selectivity of desired product R both increase with increasing channel hydraulic diameter for the two concentrations, although for the present study conditions the increases are relatively small. This is because the heat is released less efficiently when the channel cross-section increases, resulting in higher temperatures in process fluid. Since temperature favors reaction 1 in this case, the conversion of A and selectivity of R both increase with increasing channel cross-section length.

The difference between the maximum temperature and the inlet temperature ΔT_m increases as well with increasing channel cross-section length for both concentrations. Compared to the temperature increase ΔT_a in adiabatic condition, the hot point of the three channels is 2-3 K (for $C_{A0} = C_{B0}$ = 300 mol.m^{-3}) and 11-12 K (for $C_{A0} = C_{B0}$ = 100 mol.m^{-3}) lower than adiabatic condition. As expected, the faster the reaction is, the more difficult it is to release the heat.

To conclude, in this reaction case ($E_1 > E_2$), the reaction is very fast and reactant B is totally consumed rapidly for the three zigzag channels. When the hydraulic diameter of zigzag channels varies from 2 mm to 4 mm, the conversion of reactant A and the selectivity of desired product R both increase, the difference between the maximum temperature and the inlet temperature increases as well. It means that scale-up favors conversion and selectivity for this reaction case. However it should be noticed that the hot point increases as well. This should be taken into account in the evaluation of scale-up strategies for the safety concern or product decomposition at high temperature.

3.2 Reaction case $E_1 < E_2$

For the reaction case $E_1 < E_2$, temperature favors reaction 2 (undesired reaction). Thus, it is better to keep a low temperature in order to form more desired product. An inlet temperature of

utility fluid at 305 K is then set. The concentrations of the desired product R, the undesired product S and the reactants A and B at different locations in three zigzag channels are calculated with two inlet reactant concentrations (300 and 100 $mol.m^{-3}$) and presented in Figure V-4. As the reaction rates are slower in this case, the reactions do not finish for inlet concentration of 100 $mol.m^{-3}$ for the channel length studied (as shown in Figure V-4 (d), (e), (f)). Therefore, it is better to present the concentration profiles for both inlet concentrations for the discussion. It can be seen that the reactions finish after 10 m for inlet concentration of 300 $mol.m^{-3}$ (in Figure V-4 (a), (b), (c)). For the inlet concentration of 100 $mol.m^{-3}$, the reactant B is not consumed completely after 10 m. When B is totally consumed, the concentration of reactant A should be equal to that of undesired product S.

The temperatures of process fluid and of utility fluid in HEX reactor with zigzag channel of 2 mm width with inlet concentrations of 300 $mol.m^{-3}$ is presented in Figure V-5. The temperature of the process fluid increases a little at the beginning, then it is cooled rapidly by the utility fluid and reaches the same temperature as utility fluid. That is because the reaction rate is fast when the reactants just enter the channel, this produces a hot point (temperature peak) which vanishes rapidly when the reaction rate becomes slower, as can be seen in Figure V-4.

The temperature profiles of the process fluid in the three zigzag channels for the inlet concentration of 300 $mol.m^{-3}$ are shown in Figure V-6. In Figure V-6, the temperature peak increases with increasing channel hydraulic diameter. That is because the heat transfer performance decreases (shown in Table V-4) when channel cross-section width increases, so heat produced by the reaction is transferred less efficiently. This can be clearly seen after the peak, the process fluid is cooled less efficiently for the channel cross-section of 4 mm width compared to that of 3 mm and 2 mm, although they reach the same temperature at the end.

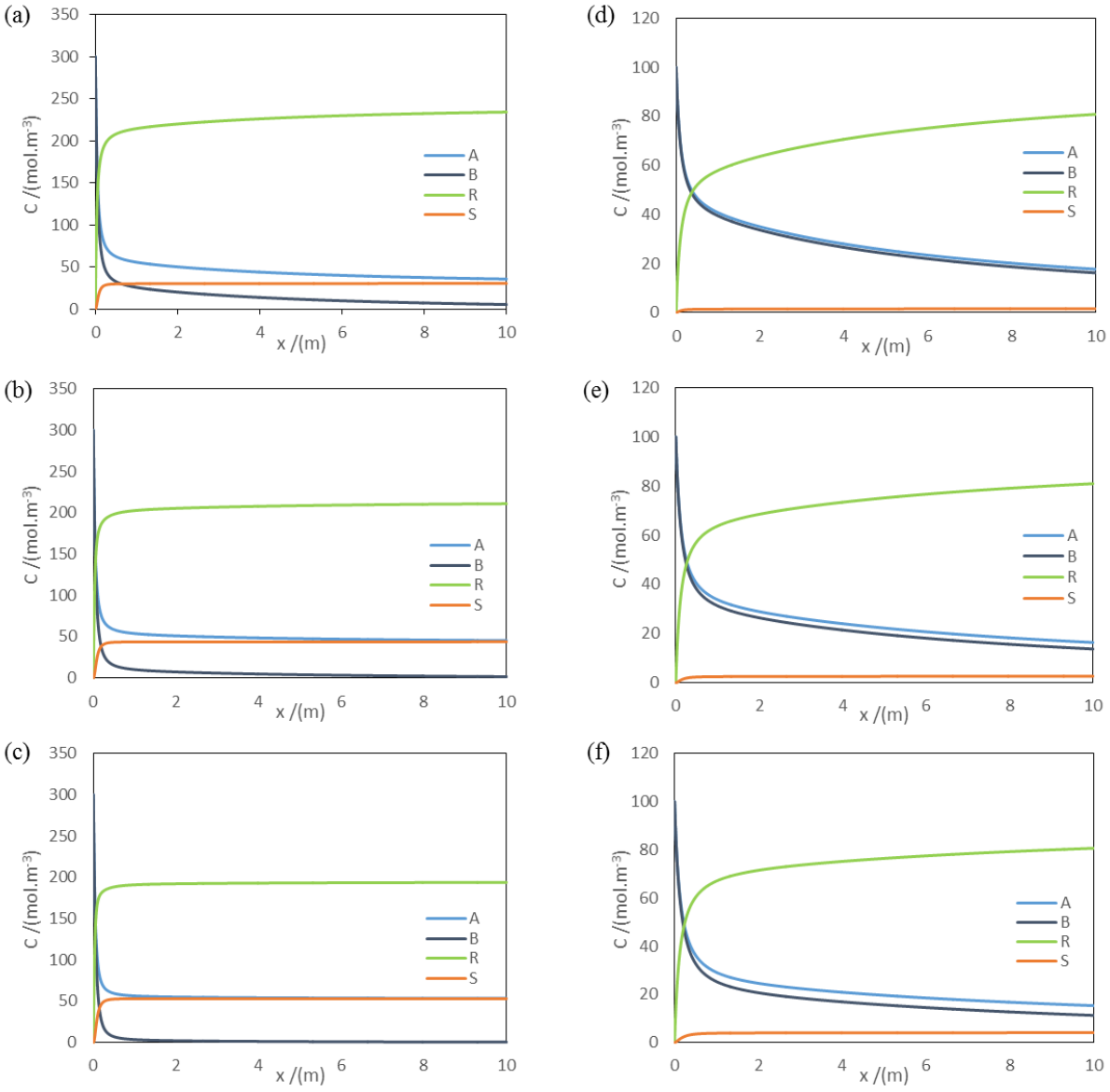

Figure V-4: Concentration profiles in zigzag channels of (a, d) 2 mm, (b,e) 3 mm and (c,f) 4mm with inlet reactant concentrations of (a, b, c) 300 mol.m^{-3} and (d, e f) 100 mol.m^{-3}

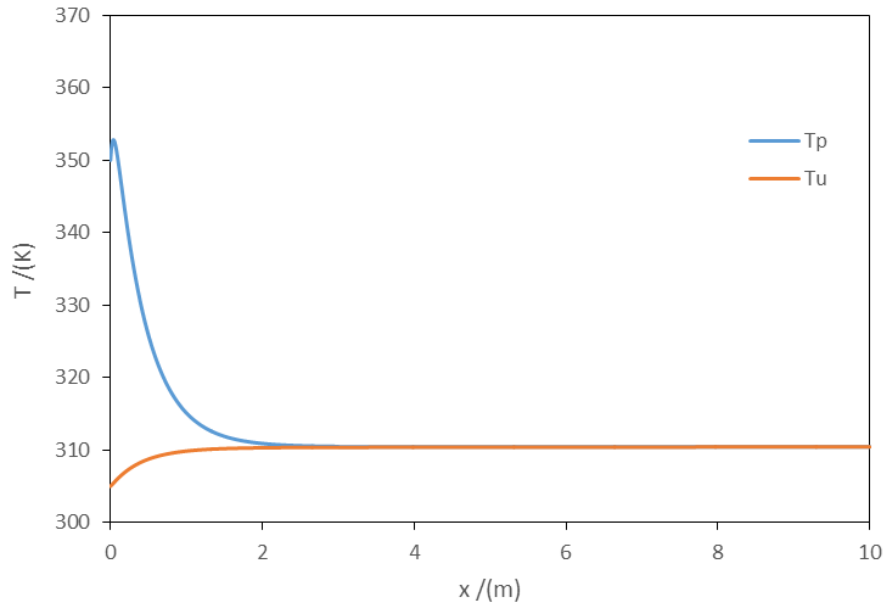

Figure V-5: Temperature profiles of process fluid and of utility fluid in HEX reactor with zigzag channel of 2 mm and C_{A0} = C_{B0} = 300 mol.m^{-3}

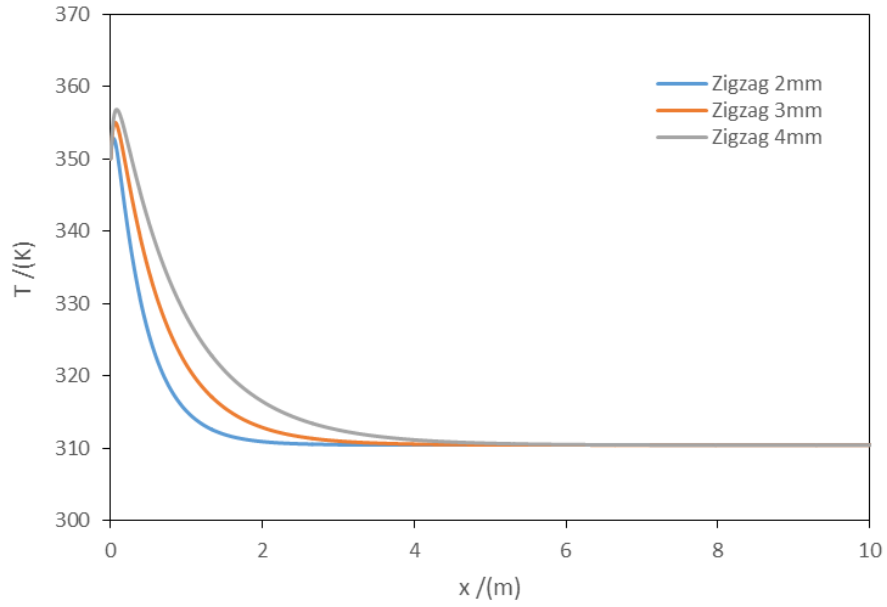

Figure V-6: Temperature profiles of process fluid in three zigzag channels with C_{A0} = C_{B0} = 300 mol.m^{-3}

The difference between the temperature peak and the inlet temperature (ΔT_m) in three zigzag channels for both inlet reactant concentrations (300 and 100 mol.m^{-3}) is calculated and presented in the Table V-6. The adiabatic temperature profile is also calculated with setting the

overall heat transfer coefficient U_x = 0 in the simulation. The difference of outlet temperature and the temperature (ΔT_a) is calculated and presented in the same table. The conversion of reactant A and the selectivity of desired product R in three zigzag channels are also presented in Table V-6.

Table V-6: Conversion, selectivity and maximal temperature difference with and without heat transfer (adiabatic) in three zigzag channels for two inlet concentrations

	$C_{A0} = C_{B0}$ = 300 mol.m^{-3}				$C_{A0} = C_{B0}$ = 100 mol.m^{-3}			
	Conversion of A	**Selectivity of R**	**ΔT_m (K)**	**ΔT_a (K)**	**Conversion of A**	**Selectivity of R**	**ΔT_m (K)**	**ΔT_a (K)**
Zigzag 2mm	88.2%	88.5%	2.8	14.7	82.3%	98.2%	0.0	15.0
Zigzag 3mm	84.9%	82.8%	5.0	14.7	83.6%	96.8%	0.0	15.0
Zigzag 4mm	82.2%	78.5%	6.8	14.7	84.7%	95.2%	0.0	15.0

From this table, the conversion of the reactant A and the selectivity of the desired product R both decreases with increasing channel cross-section width for inlet concentration of 300 mol.m^{-3}. This is because when the channel hydraulic diameter increases, the heat transfer performance decreases as discussed before, which leads to higher temperature in the zigzag channel of 4 mm compared to that of 2 mm. Since temperature favors reaction 2 in this case, the selectivity of R hence decreases with increasing channel cross-section width. Thus the production of the undesired product S and the consumption of reactant B by reaction 2 increases as well, which leads to the decrease of the conversion of reactant A (consumed by reaction 1). For the inlet concentration of 100 mol.m^{-3}, the selectivity of R decreases with increasing cross-section width as well. As for the conversion of reactant A, it increases with increasing channel cross-section width due to uncomplete reaction. It should decrease when the reactant B is totally consumed.

The difference between the maximum temperature and inlet temperature ΔT_m increases with increasing cross-section width for concentration of 300 mol.m^{-3}. For the concentration of 100 mol.m^{-3}, the temperature decreases all the time in three channels because heat transfer is faster than heat production. Compared to the temperature increase ΔT_a in adiabatic condition, the hot point of three channels is 8-12 K (for $C_{A0} = C_{B0}$ = 300 mol.m^{-3}) and 15 K (for $C_{A0} = C_{B0}$ = 100

mol.m^{-3}) lower than in the adiabatic case. It shows the good heat transfer performance of HEX reactors.

To conclude, in this reaction case ($E_1 < E_2$), the reaction is finished after 10 m for inlet concentration of 300 mol.m^{-3}, but not for inlet concentration of 100 mol.m^{-3} where the reactant B still remains at the end. When the hydraulic diameter of zigzag channels varies from 2 mm to 4 mm, the selectivity of the desired product R decreases for both inlet concentrations, the conversion rate of reactant A decreases for the inlet concentration of 300 mol.m^{-3} and increases for the inlet concentration of 100 mol.m^{-3} due to uncomplete reaction. The difference between the maximum temperature and inlet temperature increases with increasing cross-section width for concentration of 300 mol.m^{-3}. That means the scale-up does not favor the conversion and the selectivity and a hotter point is created. So for this reaction case, it is better to use smaller channels in parallel than a large channel for the scale-up strategy.

4. Conclusion

In this chapter, a 1D model of plug flow is used to study the heat transfer performance of compact HEX reactors with introducing chemical reactions. The heat transfer coefficient is calculated with the Nusselt number correlation established in the previous chapters. The performances of HEX reactors in terms of conversion and selectivity for the implementation of an exothermic competitive consecutive reaction scheme are discussed. Two cases of reactions are investigated, one is the activation energy of desired reaction larger than undesired reaction (E1 > E2), the other case is the activation energy of desired reaction smaller than undesired reaction (E1 < E2). For the case E1 > E2, high temperature of utility fluid is introduced while for E1 < E2, low temperature of utility fluid is considered for the purpose of producing more desired product R. For each case, two inlet concentrations of reactants are simulated.

The compact HEX reactors simulated in this chapter are based on the geometry studied in the last three chapters, with the same zigzag channels in the process plate (d_h = 2, 3, 4 mm). Two utility plates with straight channel are used with the consideration of industrial design. The influence of process channel hydraulic diameter on the hot point (temperature), the conversion rate and the selectivity is discussed. It is found that for the case E1 > E2, when the channel cross-section width varies from 2 mm to 4 mm, the conversion of the reactant A and the selectivity in the desired product R both increase which are favorable for the scale-up. The hot point increases as well which should be taken into account. For E1 < E2, the conversion of A

and the selectivity in the desired product R decrease with increasing channel cross-section length which is not favorable for the scale-up, so is the hot point. In this reaction case, it is better to use smaller channels in parallel than larger channels for the scale-up strategy.

For the resolution of the model, the correlation of Nusselt number in zigzag channels established in previous Chapters is applied in the simulation. Here it is shown as an example how the correlation can be used. The reliability of the simulation result shows the accuracy of the correlations. Plus the simulation results with reactions in this Chapter, all the data will be very useful for the scale-up of compact heat-exchanger reactors and facilitate their industrial applications.

General conclusion

The concept of process intensification emerged 40 years ago and many intensified technologies have been developed since then. They can be divided into two parts: single unit operation intensification and intensification among different units. Several intensified reactors are presented in Chapter I: static mixers, spinning disk reactors, rotating packed bed reactors and microreactors, based on different intensification strategies. For static mixers, it is the immobile inserts that can redistribute the fluid in the radial direction. The spinning disk and rotating packed bed reactors use the centrifugal force to intensify the transfer phenomena in the process. As for microreators, it is the miniaturization that enhances mass transfer and heat transfer providing high surface-to-volume ratio. The heat-exchanger (HEX) reactors are presented in more details. They combine two process intensification methods: the miniaturization and the multifunctionality. Several industrial HEX reactors are also presented. The hydrodynamic performances of HEX reactors are discussed: flow patterns, residence time, mixing and pressure loss. Several temperature measurement methods in liquid flows are presented for characterizing their thermal performance, including the laser-induced fluorescence thermometry.

This thesis concentrates on the thermal characterization of zigzag millimetric channels which can be used for the design of compact HEX reactors. Several theses have been carried out at the Laboratoire de Génie Chimique which dealt with the thermo-hydraulic performances of this type of HEX reactors, in particular the thesis of Anxionnaz [55]. In the present work, the influence of the channel geometry in terms of hydraulic diameter and straight section length between bends on the heat transfer coefficient has been particularly studied. The objective of this thesis is to use and develop characterization methods adapted to millimetric channels in order to correlate the heat transfer coefficient to fluid properties, channel geometry and operating conditions.

In Chapter II, the heat transfer performance of compact HEX reactor prototypes are experimentally characterized, in terms of overall heat transfer coefficient and heat transfer coefficient of the process side. The Reynolds number studied covers laminar regime and transient regime. For the HEX reactor prototypes, two kinds of process channel configuration are investigated: straight channels and zigzag channels with 3 different square cross-sections (d_h = 2mm, 3mm, 4 mm). With water as process fluid, the heat transfer coefficient in zigzag channels is much larger than that in straight channels, with a ratio between 2 and 5 in the range of Reynolds number studied, demonstrating the heat transfer enhancement of zigzag channels

compared to straight channel configuration. With the purpose of studying the influence of fluid property on the heat transfer in zigzag channels, another more viscous fluid is used in this work: a glycerol solution with a mass fraction of 74%. It presents a viscosity around 30 times higher than water at 20 °C. Its Reynolds number is in laminar regime. It is found that the evolution of heat transfer coefficient with glycerol solution as a function of Reynolds number is similar to that with water. A correlation of Nusselt number in zigzag channels is proposed from the experimental data, in terms of fluid properties (*Pr*), channel geometries (d_h/L_s), and fluid velocity (*Re*). This correlation does not fit very well with the experimental data of glycerol solution compared with water, maybe due to experimental errors. Concerning the influence of channel geometry on Nusselt number, the ratio of the channel hydraulic diameter divided by the straight section length between two bends (d_h /L_s) plays an important role.

In order to furtherly study the influence of this parameter (d_h/L_s) on the heat transfer, a numerical method based on CFD simulation is then used in Chapter III. The simulations are carried out in zigzag channels with square cross-section of 2 mm with Reynolds numbers ranging from 112 to 560 (laminar flow regime). The straight section length between two bends ranges from 2 mm to 12 mm are investigated. The heat transfer performance in a straight channel with the same cross-section is also studied as a reference. The numerical method is validated by comparison with experimental results in terms of Nusselt number obtained in Chapter II. The results show that local Nusselt numbers and Fanning friction factors vary along the zigzag channels in the form of oscillating curves. The amplitude of the oscillations is constant with periodic flow but varies in the case of non-periodic flow. Based on Fourier analysis, a map has been provided which allows the distinction of the conditions that give a periodic flow or a non-periodic flow. Non-periodic flow can be obtained by increasing the fluid velocity or by decreasing the straight section length between two bends. The heat transfer enhancement and thermo-hydraulic performance factor are quantitatively discussed, showing the zigzag channel enhances the heat transfer strongly and increases pressure drop less significantly compared with the straight channel. It appeared that non-periodic flow is not particularly interesting in terms of thermo-hydraulic performances.

In the simulation, problems of convergence or mesh independence have been met when Reynolds number increases (in laminar regime) or when the straight section length between two bends decreases. In addition, it is much more complicated to carry out the simulation in transient regime, since there is not a generic thermal-hydrodynamic model available for this particular flow regime. In order to overcome these limitations of simulation, an experimental method

based on laser-induced fluorescence thermometry with two-color/two dyes is developed in Chapter IV for the measurement of local temperature. The temperature field at different levels and at different locations in the three zigzag channels is obtained. It is found that the temperature over the cross-section is more homogeneous in the zigzag channel of 3 mm than in the zigzag channel of 4 mm. Furtherly, a heat transfer model is introduced to evaluate the consistency of the LIF. It is found that the temperature difference gets bigger when the channel hydraulic diameter decreases. That is probably because the temperature calibration method has just been carried out in the zigzag channel of 4 mm. It is better to do it for the other two zigzag channels as well.

In last Chapter, a 1D model of plug flow is used to study the heat transfer performance of compact HEX reactors for the implementation of chemical reactions. Their performance in terms of conversion, selectivity for an exothermic competitive consecutive reaction scheme is discussed. Two cases of reactions are investigated: one is the activation energy of desired reaction larger than undesired reaction (E1 > E2), the other case is the activation energy of desired reaction smaller than undesired reaction (E1 < E2). For the case E1 > E2, high temperature of utility fluid is introduced while for E1 < E2, low temperature of utility fluid is considered for the purpose of producing more desired product R. The objective is to illustrate how such a model, based on the prior characterization of heat transfer performance of the devices, can be used for choosing optimal scale-up strategies. In the studied cases, the reactor scaling-up favors the production of the desired product in the first case while numbering-up is more appropriate for the second case.

This work allows the development of methods (experimental and numerical) for flow characterization and heat transfer coefficient measurements adapted to millimetric channels used in compact HEX reactors. These methods have been implemented to study the heat transfer performances of square zigzag channels. However it shows that for numerical method, the development of new numerical models or assessment of the reliability of available models is needed to simulate transient flow regime for numerous innovative design of compact HEX reactors which can define correlations for a large range of technologies. All these data will facilitate the process design (choice of the devices and optimization of the operating conditions) and the process scale-up.

The proposed correlation for zigzag channels in Chapter II was established from the experimental data mainly with the variation of the channel width and flow rate of process fluid. Other geometry parameters like the radius of curvature, the straight section length between two bends (although being numerically studied), the angle between two straight sections, should also be studied to enrich the data, so are process fluids with a wide range of physico-chemical properties.

An original breakthrough in this thesis concerns the development of an experimental method based on laser-induced fluorescence thermometry with two-colors/two dyes. The result obtained in this work mainly showed the feasibility of the method. More studies need to be conducted for the future work to improve the reliability of this method for temperature field measurement inside the channel.

The work presented in this thesis concerns a monophase flow. However, in many chemical synthesis cases, the reaction takes place in a multiphase flow. Studies have already been conducted on the hydraulic behavior of these media as well as the determination of mass transfer coefficients. It would then be useful to extend the methodologies developed in this thesis for the characterization of heat exchange performance to more complex media, for example liquid-liquid flow.

References

[1] C. Ramshaw, Design Method for Plate Evaporators and Condensers, Proc. 1st Int. Conf. Process Intensif. Chem. Ind. 18 (1995) 34–47.

[2] A. Stankiewicz, J.A. Moulijn, Process Intensification: Transforming Chemical Engineering, Chem. Eng. Prog. 96 (2000) 22–34.

[3] S. Neveu, Potential benefits of process intensification for Rhodia, Proceeding of 3rd Meeting of Process Intensif. Network. Cranfield University. (2002).

[4] H. Hahn, Market pull meets technology push, Degussa Sci. Newsl. 10 (2005) 4–6.

[5] J.M. Ponce-ortega, M.M. Al-thubaiti, M.M. El-halwagi, Chemical Engineering and Processing : Process Intensification Process intensification : New understanding and systematic approach, Chem. Eng. Process. Process Intensif. 53 (2012) 63–75.

[6] T. Van Gerven, A. Stankiewicz, Structure, Energy, Synergy, Time-The Fundamentals of Process Intensification, Ind. Eng. Chem. Res. (2009) 2465–2474.

[7] D. Reay, C. Ramshaw, A. Harvey, Process Intensification: Engineering for Efficiency, Sustainability and Flexibility, in: Isot. Org. Chem., Butterworth-Heinemann, Oxford, 2008: pp. 8–9.

[8] F. Kang, D. Wang, Y. Pu, X.-F. Zeng, J.-X. Wang, J.-F. Chen, Efficient preparation of monodisperse CaCO3 nanoparticles as overbased nanodetergents in a high-gravity rotating packed bed reactor, Powder Technol. 325 (2018) 405–411.

[9] H.-L. Fan, S.-F. Zhou, J. Gao, Y.-Z. Liu, Continuous preparation of Fe3O4 nanoparticles through Impinging Stream-Rotating Packed Bed reactor and their electrochemistry detection toward heavy metal ions, J. Alloys Compd. 671 (2016) 354–359.

[10] C.-C. Lin, J.-S. Liao, Production of CuO nanoparticles using a simple precipitation method in a rotating packed bed with blade packings, J. Alloys Compd. 775 (2019) 419–426.

[11] C.-C. Lin, Y.-C. Lin, Preparation of ZnO nanoparticles using a rotating packed bed, Ceram. Int. 42 (2016) 17295–17302.

[12] D. Wenzel, A. Górak, Review and analysis of micromixing in rotating packed beds, Chem. Eng. J. 345 (2018) 492–506.

[13] F. Visscher, J. van der Schaaf, T.A. Nijhuis, J.C. Schouten, Rotating reactors – A review, Chem. Eng. Res. Des. 91 (2013) 1923–1940.

[14] H. Zhao, L. Shao, J. Chen, High-gravity process intensification technology and application, Chem. Eng. J. 156 (2010) 588–593.

[15] X. Shi, Y. Xiang, L.-X. Wen, J.-F. Chen, CFD analysis of liquid phase flow in a rotating packed bed reactor, Chem. Eng. J. 228 (2013) 1040–1049.

[16] K. Neumann, K. Gladyszewski, K. Groß, H. Qammar, D. Wenzel, A. Górak, M. Skiborowski, A guide on the industrial application of rotating packed beds, Chem. Eng. Res. Des. 134 (2018) 443–462.

[17] N.C. Jacobsen, O. Hinrichsen, Micromixing Efficiency of a Spinning Disk Reactor, Ind. Eng. Chem. Res. 51 (2012) 11643-11652.

[18] R. Jachuck, Process Intensification for Responsive Processing, Chem. Eng. Res. Des. 80 (2002) 233–238.

[19] P. Oxley, C. Brechtelsbauer, F. Ricard, N. Lewis, C. Ramshaw, Evaluation of Spinning Disk Reactor Technology for the Manufacture of Pharmaceuticals, Ind. Eng. Chem. Res. (2000) 2175–2182.

[20] K.V.K. Boodhoo, R.J. Jachuck, Process intensification: spinning disk reactor for styrene polymerisation, Appl. Therm. Eng. 20 (2000) 1127–1146.

[21] Z. Qiu, J. Petera, L.R. Weatherley, Biodiesel synthesis in an intensified spinning disk reactor, Chem. Eng. J. 210 (2012) 597–609.

[22] H.-S. Liu, Y.-H. Wang, C.-C. Li, C.Y. Tai, Characterization of AgI nanoparticles synthesized in a spinning disk reactor, Chem. Eng. J. 183 (2012) 466–472.

[23] S. Mohammadi, A. Harvey, K.V.K. Boodhoo, Synthesis of TiO2 nanoparticles in a spinning disc reactor, Chem. Eng. J. 258 (2014) 171–184.

[24] H. Bagheri Farahani, M. Shahrokhi, A. Molaei Dehkordi, Experimental investigation and process intensification of barium sulfate nanoparticles synthesis via a new double coaxial spinning disks reactor, Chem. Eng. Process. Process Intensif. 115 (2017) 11–22. https://doi.org/10.1016/j.cep.2017.02.007.

[25] H. Krummradt, U. Kopp, J. Stoldt, Experiences with the use of microreactors in organic synthesis, Proc. 3rd Int. Conf. Microreact. Technol. Springer-Verl. Berl. (2000).

[26] M. MOREAU, Methodologies pour la caracterisation hydrodynamique et l'extrapolation de réacteurs intensifiés millistructurés, INP. (2014).

[27] X. Yao, Y. Zhang, L. Du, J. Liu, J. Yao, Review of the applications of microreactors, Renew. Sustain. Energy Rev. 47 (2015) 519–539.

[28] G.N. Doku, W. Verboom, N. Reinhoudt, A. Van Den Berg, On-microchip multiphase chemistry: a review of microreactor design principles and reagent contacting modes, Tetrahedron. 61 (2005) 2733–2742.

[29] B.P. Mason, K.E. Price, J.L. Steinbacher, A.R. Bogdan, D.T. Mcquade, Greener Approaches to Organic Synthesis Using Microreactor Technology, Chem. Rev. (2007) 2300–2318.

[30] G. Kolb, V. Hessel, Micro-structured reactors for gas phase reactions, Chem. Eng. J. 98 (2004) 1–38. https://doi.org/10.1016/j.cej.2003.10.005.

[31] R.K. Thakur, C. Vial, K.D.P. Nigam, E.B. Nauman, G. Djelveh, Static mixers in the process industriesða review, Chem. Eng. Res. Des. 81 (2003)787–826.

[32] N.R. Schott, B. Weinstein, D. LaBombard, Motionless mixers, Chem Eng Prog. 75 (1975) 54–58.

[33] N. Khac Tien, F. Streiff, E. Flaschel, A. Renken, Motionless mixers for the design of multitubular polymerization reactors, Chem. Eng. Technol. 13 (1990) 214–220.

[34] J.R. Baker, Motionless mixers stir up new uses, Chem. Eng. Prog. 87 (1991) 32–38.

[35] K.J. Myers, A. Bakker, D. Ryan, Avoid agitation by selecting static mixers, Chem. Eng. Prog. 93 (1997) 28–38.

[36] Z. Anxionnaz, M. Cabassud, C. Gourdon, P. Tochon, Heat exchanger / reactors (HEX reactors): Concepts , technologies :, Chem. Eng. Process. Process Intensif. 42 (2008) 2029–2050.

[37] Q. Li, G. Flamant, X. Yuan, P. Neveu, L. Luo, Compact heat exchangers : A review and future applications for a new generation of high temperature solar receivers, Renew. Sust. Energ. Rev. 15 (2011) 4855–4875.

[38] N. Niedbalski, D. Johnson, S.S. Patnaik, D. Banerjee, Study of a multi-phase hybrid heat exchanger-reactor (HEX reactor): Part II – Numerical prediction of thermal performance, Int. J. Heat Mass Transf. 70 (2014) 1086–1094.

[39] N. Niedbalski, D. Johnson, S.S. Patnaik, D. Banerjee, Study of a multi-phase hybrid heat exchanger-reactor (HEX reactor): Part I – Experimental characterization, Int. J. Heat Mass Transf. 70 (2014) 1078–1085.

[40] M. Chen, X. Sun, R.N. Christensen, Thermal-hydraulic performance of printed circuit heat exchangers with zigzag flow channels, Int. J. Heat Mass Transf. 130 (2019) 356–367.

[41] M. Chen, X. Sun, R.N. Christensen, S. Shi, I. Skavdahl, V. Utgikar, Annals of Nuclear Energy Experimental and numerical study of a printed circuit heat exchanger, Ann. Nucl. Energy. 97 (2016) 221–231.

[42] D. Kwon, L. Jin, W. Jung, S. Jeong, Experimental investigation of heat transfer coefficient of mini-channel PCHE (printed circuit heat exchanger), Cryogenics. 92 (2018) 41–49.

[43] X. Guo, Y. Fan, L. Luo, Multi-channel heat exchanger-reactor using arborescent distributors : A characterization study of fluid distribution, heat exchange performance and exothermic reaction, Energy. 69 (2014) 728–741.

[44] F. Théron, Z. Anxionnaz-minvielle, M. Cabassud, C. Gourdon, P. Tochon, Chemical Engineering and Processing : Process Intensification Characterization of the performances of an innovative heat-exchanger / reactor, Chem. Eng. Process. Process Intensif. 82 (2014) 30–41.

[45] Y. Zhang, V. Sethi, Compact heat exchange reactor for synthesis of mixed alcohols, Catal. Today. 259 (2016) 393–401.

[46] A. Bakhtyari, M. Parhoudeh, M. Reza, Optimal conditions in converting methanol to dimethyl ether, methyl formate and hydrogen utilizing a double membrane heat exchanger reactor, J. Nat. Gas Sci. Eng. 28 (2016) 31–45.

[47] Alfa Laval, Alfa Laval ART PR 37. (2005a).

[48] Alfa Laval, Alfa Laval ART PR 49. (2005b).

[49] Corning, Corning Adv.-Flow^{TM} React. (2010).

[50] Chart industries, Shimtech React. (2009).

[51] L. Despènes, S. Elgue, C. Gourdon, M. Cabassud, Impact of the material on the thermal behaviour of heat exchangers-reactors, Chem. Eng. Process. Process Intensif. 52 (2012) 102–111.

[52] Laurène Despènes, Intensification et passage en continu d'une synthèse pharmaceutique en réacteur-échangeur, INP. (2010).

[53] Céline Fustier, Développement d'un réacteur intensifié en Carbure de Silicium pour la transposition en continu de réactions d'hydrosilylation, INP. (2012).

[54] Kevin Lachin, De la stabilité à la coagulation de latex acrylique : étude des mécanismes et mise en oeuvre en milliréacteur, INP. (2016).

[55] Z. ANXIONNAZ, Etude de l'influence de la géométrie des canaux sur les performances d'un réacteur/échangeur., INP. (2009).

[56] M. Roudet, K. Loubiere, C. Gourdon, M. Cabassud, Hydrodynamic and mass transfer in inertial gas–liquid flow regimes through straight and meandering millimetric square channels, Chem. Eng. Sci. 66 (2011) 2974–2990.

[57] W.R. Dean, Note on the notion of fluid in a curved pipe, Phil Mag 4. 20 (1927) 208–223.

[58] L. Wang, F. Liu, Forced convection in slightly curved microchannels, Int. J. Heat Mass Transf. 50 (2007) 881–896.

[59] R.M. Manglik, J. Zhang, A. Muley, Low Reynolds number forced convection in three-dimensional wavy-plate-fin compact channels: Fin density effects, Int. J. Heat Mass Transf. 48 (2005) 1439–1449.

[60] Y. Sui, C.J. Teo, P.S. Lee, Y.T. Chew, C. Shu, Fluid flow and heat transfer in wavy microchannels, Int. J. Heat Mass Transf. 53 (2010) 2760–2772.

[61] Y. Sui, P.S. Lee, C.J. Teo, An experimental study of flow friction and heat transfer in wavy microchannels with rectangular cross section, Int. J. Therm. Sci. 50 (2011) 2473–2482.

[62] N.R. Rosaguti, D.F. Fletcher, B.S. Haynes, Laminar flow and heat transfer in a periodic serpentine channel with semi-circular cross-section, Int. J. Heat Mass Transf. 49 (2006) 2912–2923.

[63] R. Gupta, P.E. Geyer, D.F. Fletcher, B.S. Haynes, Thermohydraulic performance of a periodic trapezoidal channel with a triangular cross-section, Int. J. Heat Mass Transf. 51 (2008) 2925–2929.

[64] N.R. Rosaguti, D.F. Fletcher, B.S. Haynes, Laminar flow and heat transfer in a periodic serpentine channel, Chem. Eng. Technol. 28 (2005) 353–361.

[65] P.E. Geyer, N.R. Rosaguti, D.F. Fletcher, B.S. Haynes, Thermohydraulics of square-section microchannels following a serpentine path, Microfluid. Nanofluidics. 2 (2006) 195–204.

[66] P.E. Geyer, D.F. Fletcher, B.S. Haynes, Laminar flow and heat transfer in a periodic trapezoidal channel with semi-circular cross-section, Int. J. Heat Mass Transf. 50 (2007) 3471–3480.

[67] N.R. Rosaguti, D.F. Fletcher, B.S. Haynes, Low-Reynolds number heat transfer enhancement in sinusoidal channels, Chem. Eng. Sci. 62 (2007) 694–702.

[68] Z. Zheng, D.F. Fletcher, B.S. Haynes, Chaotic advection in steady laminar heat transfer simulations: Periodic zigzag channels with square cross-sections, Int. J. Heat Mass Transf. 57 (2013) 274–284.

[69] H. Aref, Stirring by chaotic advection, J. Fluid Mech. 143 (1984) 1.

[70] M.G. Olsen, J.G. Santiago, R.J. Adrian, R.H. Liu, M.A. Stremler, K. V Sharp, M.G. Olsen, J.G. Santiago, R.J. Adrian, H. Aref, D.J. Beebe, Passive Mixing in a Three-Dimensional Serpentine Microchannel Passive Mixing in a Three-Dimensional Serpentine Microchannel, 9 (2000) 190–197.

[71] A.D. Stroock, S.K.W. Dertinger, A. Ajdari, I. Mezić, H.A. Stone, G.M. Whitesides, Chaotic mixer for microchannels, Science. 295 (2002) 647–651.

[72] F. Jiang, K.S. Drese, S. Hardt, M. Küpper, F. Schönfeld, Helical flows and chaotic mixing in curved micro channels, AIChE J. 50 (2004) 2297–2305.

[73] V. Kumar, K.D.P. Nigam, Laminar convective heat transfer in chaotic configuration, Int. J. Heat Mass Transf. 50 (2007) 2469–2479.

[74] C. Castelain, A. Mokrani, Y. Le Guer, H. Peerhossaini, Experimental study of chaotic advection regime in a twisted duct flow, Eur. J. Mech. BFluids. 20 (2001) 205–232.

[75] H. Peerhossaini, C. Castelain, Y. Le Guer, Heat exchanger design based on chaotic advection, Exp. Therm. Fluid Sci. 7 (1993) 333–344.

[76] N. Acharya, M. Sen, C. Hsueh-Chia, Heat transfer enhancement in coiled tubes by chaotic mixing, Int. J. Heat Mass Transf. 35 (1992) 2475–2489.

[77] Z. Anxionnaz-Minvielle, M. Cabassud, C. Gourdon, P. Tochon, Influence of the meandering channel geometry on the thermo-hydraulic performances of an intensified heat exchanger/reactor, Chem. Eng. Process. Process Intensif. 73 (2013) 67–80.

[78] M. Moreau, N. Di Miceli Raimondi, N. Le Sauze, C. Gourdon, M. Cabassud, A new numerical method for axial dispersion characterization in microreactors, Chem. Eng. Sci. 168 (2017) 178–188.

[79] K. Kunowa, S. Schmidt-Lehr, W. Pauer, H.-U. Moritz, C. Schwede, Characterization of Mixing Efficiency in Polymerization Reactors Using Competitive-Parallel Reactions, Macromol. Symp. 259 (2007) 32–41.

[80] R.L. Webb, E.R.G. Eckert, Application of rough surfaces to heat exchanger design, Int. J. Heat Mass Transf. 15 (n.d.) 1647–1658.

[81] R.K. Shah, A.L. London, Laminar flow forced convection in ducts: A source book for compact heat exchanger analytical data, Acad. Press Inc N. Y. (1978).

[82] R.K. Shah, Laminar flow friction and forced convection heat transfer in ducts of arbitrary geometry, Int. J. Heat Mass Transf. 18 (1975) 849–862.

[83] V. Gnielinski, Heat Exchanger Design Handbook, Chap. 2, Hemisphere Publ. Co. (1983).

[84] V. Gnielinski, New Equations for Heat and Mass Transfer in Turbulent Pipe and Channel Flow, Int. Chem. Eng. 16 (1976) 359–368.

[85] P.R.N. Childs, J.R. Greenwood, C.A. Long, Review of temperature measurement, Rev. Sci. Instrum. 71 (2000) 2959–2978 .

[86] P. Leblay, J.F. Henry, D. Caron, Infrared Thermography applied to measurement of Heat transfer coefficient of water in a pipe heated by Joule effect. 11th Int. Conf. Quantitative InfraRed Thermography (2012).

[87] S. Freund, S. Kabelac, Investigation of local heat transfer coefficients in plate heat exchangers with temperature oscillation IR thermography and CFD, Int. J. Heat Mass Transf. 53 (2010) 3764–3781.

[88] T. Nakajima, M. Utsunomiya, Y. Ikeda, Simultaneous Measurement of Velocity and Temperature of Water Using LDV and Fluorescence Technique, Appl. Laser Tech. Fluid Mech. (1991) 34–53.

[89] F. Lemoine, Y. Antoine, M. Wolff, M. Lebouche, Simultaneous temperature and 2D velocity measurements in a turbulent heated jet using combined laser-induced fluorescence and LDA, Exp. in Fluids. 26 (1999) 315–32.

[90] J. Sakakibara, K. Hishida, M. Maeda, Measurements of thermally stratified pipe flow using image-processing techniques, Exp. in Fluids. 96 (1993) 82–96.

[91] M.C.J. Coolen, R.N. Kieft, C.C.M. Rindt, A.A. Van Steenhoven, Application of 2-D LIF temperature measurements in water using a Nd : YAG laser, Exp. in Fluids. 27 (1999) 420–426.

[92] M. Bruchhausen, F. Guillard, F. Lemoine, Instantaneous measurement of two-dimensional temperature distributions by means of two-color planar laser induced fluorescence (PLIF), Exp. in Fluids. (2005) 123–131.

[93] G. Castanet, A. Labergue, F. Lemoine, Internal temperature distributions of interacting and vaporizing droplets, Int. J. Therm. Sci. 50 (2011) 1181–1190.

[94] J. Sakakibara, R.J. Adrian, Whole field measurement of temperature in water using two-color laser induced fluorescence, Exp. in Fluids. 26 (1999) 7–15.

[95] J. Sakakibara, R.J. Adrian, Measurement of temperature field of a Rayleigh-Bénard convection using two-color laser-induced fluorescence, Exp. in Fluids. 37 (2004) 331–340.

[96] W. Chaze, O. Caballina, G. Castanet, F. Lemoine, Spatially and temporally resolved measurements of the temperature inside droplets impinging on a hot solid surface, Exp. in Fluids. 58 (2017) 1–16.

[97] J.A. Sutton, Æ.B.T. Fisher, J.W. Fleming, A laser-induced fluorescence measurement for aqueous fluid flows with improved temperature sensitivity, Exp. in Fluids. (2008) 869–881.

[98] M.B. Shafii, C.L. Lum, M.M. Koochesfahani, In situ LIF temperature measurements in aqueous ammonium chloride solution during uni-directional solidification, Exp. in Fluids. (2010) 651–662.

[99] S. Elgue, A. Conté, C. Gourdon, Y. Bastard, Direct fluorination of 1,3-dicarbonyl compound in a continuous flow reactor at industrial scale, Chim. Oggi – Chem. Today. 30 (2012) 18–23.

[100] L. Despènes, S. Elgue, C. Gourdon, M. Cabassud, Impact of the material on the thermal behaviour of heat exchangers-reactors, Chem. Eng. Process Process Intensif. 52 (2012) 102–111.

[101] N.D.M. Raimondi, N. Olivier-Maget, N. Gabas, M. Cabassud, C. Gourdon, Safety enhancement by transposition of the nitration of toluene from semi-batch reactor to continuous intensified heat exchanger reactor, Chem. Eng. Res. Des. 94 (2015) 182–193.

[102] W.M. Kays, M.E. Crawford, Convection heat and mass transfer. 2nd ed, McGrawHill Co. (1980).

[103] M.C. Righetti, G. Salvetti, E. Tombari, Heat capacity of glycerol from 298 to 383 K, Thermochim. Acta. 316 (1998) 193–195.

[104] O.K. BATES, Thermal conductivity of liquids: Binary mixures of water and glycerol, Ind. Eng. Chem. Res. 28 (1936) 494–498.

[105] H.M. Xia, Z.P. Wang, S.Y.M. Wan, F.F. Yin, Numerical study on microstructured reactor with chaotic heat and mass transfer and its potential application for exothermic process, Chem. Eng. Res. Des. 90 (2012) 1719–1726.

[106] G.E. Karniadakis, G.S. Triantafyllou, Three-dimensional dynamics and transition to turbulence in the wake of bluff objects, J. Fluid Mech. 238 (1992) 1–30.

[107] A.M. Guzmán, C.H. Amon, Dynamical flow characterization of transitional and chaotic regimes in converging–diverging channels, J. Fluid Mech. 321 (1996) 25.

[108] A.M. Guzmán, M. Del Valle, Heat transfer enhancement in grooved channels due to flow bifurcations, Heat Mass Transfer. 42 (2006) 967–975.

[109] J. Zhang, N.S. Liu, X.Y. Lu, Route to a chaotic state in fluid flow past an inclined flat plate, Phys. Rev. E - Stat. Nonlinear Soft Matter Phys. 79 (2009) 1–4.

[110] Y. Sui, C.J. Teo, P.S. Lee, Direct numerical simulation of fluid flow and heat transfer in periodic wavy channels with rectangular cross-sections, Int. J. Heat Mass Transf. 55 (2012) 73–88.

[111] Z. Zheng, D.F. Fletcher, B.S. Haynes, Transient laminar heat transfer simulations in periodic zigzag channels, Int. J. Heat Mass Transf. 71 (2014) 758–768.

[112] R.L. Webb, E.R.G. Eckert, Application of rough surfaces to heat exchanger design, Int. J. Heat Mass Transf. 15 (1972) 1647–1658.

[113] F.P. Incropera, A.S. Lavine, T.L. Bergman, D.P. DeWitt, Fundamentals of heat and mass transfer, Wiley. (2007).

[114] J. Coppeta, C. Rogers, Dual emission laser induced fluorescence for direct planar scalar behavior measurements, Exp. in Fluids. 25 (1998) 1–15.

[115] W. Chaze, O. Caballina, G. Castanet, F. Lemoine, The saturation of the fluorescence and its consequences for laser-induced fluorescence thermometry in liquid flows, Exp. in Fluids. 57 (2016) 58.

[116] M.R. Shelat, C. Liang, H. Tuo, Conceptual analysis to evaluate suitability of compact heat exchanger reactors for rapid and complex chemical reactions, Chem. Eng. Process. Process Intensif. 140 (2019) 142–156.

Nomenclature

A cross-sectional area (m^2)

A_H heat exchange area (m^2)

C molar concentration ($mol.m^{-3}$)

C_p specific heat of the fluid ($J.kg^{-1}.K^{-1}$)

da element of cross-sectional area (m^2)

d_h hydraulic diameter (m)

D_{ax} axial dispersion coefficient ($m^2.s^{-1}$)

dl element of perimeter length (m)

dX element of development length (m)

e thickness of aluminum plate (m)

e_h heat transfer enhancement factor

E_1 activation energy of reaction 1

E_2 activation energy of reaction 2

f local Fanning friction factor

f_i frequency i (Hz)

F fluorescence signal (A.U.)

h heat transfer coefficient ($W.m^{-2}.K^{-1}$)

H enthalpy ($J.kg^{-1}$)

ΔH_{r1} heat of reaction for reaction 1 ($J.mol^{-1}$)

ΔH_{r2} heat of reaction for reaction 2 ($J.mol^{-1}$)

I_0 laser intensity ($W.m^{-2}$)

I_{sat} saturation intensity of the fluorescent dye ($W.m^{-2}$)

k thermal conductivity ($W.m^{-1}.K^{-1}$)

k_1 reaction rate coefficient of reaction 1

k_{10} frequency factor of reaction 1

k_2 reaction rate coefficient of reaction 2

k_{20} frequency factor of reaction 2

L channel length (m)

L_c curved section length (m)

L_s straight section length (m)

$\dot{m}$ mass flow rate ($kg.s^{-1}$)

$\boldsymbol{n}$ normal vector at a cross-section

N_{bend} number of bends

N_c number of divisions along the curved section

N_d number of divisions for the channel depth and width

N_e number of computational volume elements

N_s number of divisions along the straight section

N_{unit} number of periodic units

Nu local Nusselt number

p pressure (Pa)

$\bar{p}$ area average pressure (Pa)

Δp pressure drop (Pa)

P cross-section perimeter length (m)

$\mathcal{P}$ flow friction power (W)

Pe Péclet number

PF performance factor

Pr Prandtl number

q heat flux (W)

q_l thermal loss (W)

Q volumetric flowrate ($m^3\ s^{-1}$)

r radius (m)

r_1 reaction rate of reaction 1

r_2 reaction rate of reaction 2

R fluorescence ratio

$\bar{R}$ universal gas constant

R_0 fluorescence ratio at reference temperature

R_c radius of curvature (m)

Re Reynolds number

T temperature (K)

$\bar{T}$ area average temperature (K)

$\bar{T}_b$ bulk temperature (K)

$\bar{T}_w$ peripheral average temperature at the wall (K)

T_0 reference temperature (K)

ΔT_{ml} logarithmic mean temperature difference (K)

$\boldsymbol{u}$ velocity vector (m.s^{-1})

$\bar{u}$ mean fluid velocity (m.s^{-1})

w width (m)

U global heat transfer coefficient (W.m^{-2}.K^{-1})

V volume (m^3)

w width (m)

x coordinate over the developed length (m)

y coordinate over the channel width (m)

z coordinate over the channel depth (m)

Greek symbols

τ shear stress (Pa)

θ angle between two straight sections (°)

k thermal conductivity (W.m^{-1}.K^{-1})

μ dynamic viscosity (Pa.s)

ρ fluid density (kg.m^{-3})

σ_T standard temperature deviation (K)

λ wavelength (nm)

η transmission efficiency of the fluorescence light

Ω solid angle of the collection

ε_0 molar absorptivity of the fluorescent molecules

ϕ fluorescence quantum yield

Subscripts

0 value in straight channel

m mean value

p process fluid

s location x

u utility fluid

w wall

x location x

Superscripts

∞ hydrodynamically and thermally fully-developed flow

Appendix A: Experimental data in Chapter II

1. Heat transfer characterization with water as process fluid

(a) Zigzag channel 4 mm, Q_u=500 $L.h^{-1}$

Q_p ($L.h^{-1}$)	$T_{p,in}$ (°C)	$T_{p,out}$ (°C)	$T_{u,in}$ (°C)	$T_{u,out}$ (°C)	U ($W.m^{-2}.K^{-1}$)	Re_u	Nu_u	h_u ($W.m^{-2}.K^{-1}$)	Re_p	h_p ($W.m^{-2}.K^{-1}$)	Nu_p
60.6	45.5	40.8	29.6	30	8037	19346	126.8	9749	6959	13026	83.1
51	46.3	41.6	32.1	32.4	7771	20463	130.2	10050	5943	12146	77.4
40.5	47.1	42	33.6	33.9	7237	21145	132.2	10228	4762	10803	68.8
31.1	56.1	45.4	30.7	31.2	6550	19879	128.4	9894	4063	9466	59.9
20.6	57.6	44.9	32.7	33.1	5575	20735	131.0	10122	2708	7501	47.4
9.9	58.6	42.4	34.2	34.4	4031	21374	132.8	10288	1287	4933	31.2
4.7	58.4	39.6	34.8	35	2715	21649	133.6	10358	597	3093	19.6

(b) Zigzag channel 4 mm, Q_u=400 L.h^{-1}

Q_p (L.h^{-1})	$T_{p,in}$ (°C)	$T_{p,out}$ (°C)	$T_{u,in}$ (°C)	$T_{u,out}$ (°C)	U (W.m^{-2}.K^{-1})	Re_u	Nu_u	h_u (W.m^{-2}.K^{-1})	Re_p	h_p (W.m^{-2}.K^{-1})	Nu_p
60.2	45.8	41	28.3	28.8	7247	15021	101.7	7802	6939	12580	80.2
49.1	46.6	41.6	30.4	30.8	6902	15761	104.1	8014	5732	11386	72.6
38.7	47.4	42.1	32.6	32.9	6514	16515	106.5	8223	4566	10225	65.1
30.3	56.8	46	30.6	31.7	6209	15939	104.7	8064	3995	9585	60.6
20.3	57.7	44.3	30.2	31.5	5315	15868	104.4	8044	2660	7617	48.2
10.2	58.9	42.8	33.3	34.4	3941	16953	107.8	8342	1332	5031	31.8
5	58.9	40	34.3	35	2768	17246	108.7	8420	640	3260	20.6

(c) Zigzag channel 4 mm, Q_u=300 L.h^{-1}

Q_p (L.h^{-1})	$T_{p,in}$ (°C)	$T_{p,out}$ (°C)	$T_{u,in}$ (°C)	$T_{u,out}$ (°C)	U (W.m^{-2}.K^{-1})	Re_u	Nu_u	h_u (W.m^{-2}.K^{-1})	Re_p	h_p (W.m^{-2}.K^{-1})	Nu_p
60.7	46.7	43.1	32.6	33.8	7077	12523	81.8	6326	7188	14258	90.8
49.2	47.3	43.8	34	35	6787	12879	83.0	6426	5867	12950	82.4
39.8	47.8	43.6	35.4	36.3	6377	13267	84.2	6533	4779	11392	72.5
30.3	57.3	49.2	36.9	38.2	5959	13740	85.6	6662	4106	9997	63.0
20.8	58.2	48.6	38.1	39.1	5188	14020	86.5	6737	2827	7957	50.2
10.2	56.1	45.2	36.6	37.6	3796	13601	85.2	6624	1359	5121	32.3
5.1	58.8	41.3	35.6	36.3	2736	13294	84.3	6541	658	3372	21.3

(d) Zigzag channel 3 mm, Q_u=500 L.h^{-1}

Q_p (L.h^{-1})	$T_{p,in}$ (°C)	$T_{p,out}$ (°C)	$T_{u,in}$ (°C)	$T_{u,out}$ (°C)	U (W.m^{-2}.K^{-1})	Re_u	Nu_u	h_u (W.m^{-2}.K^{-1})	Re_p	h_p (W.m^{-2}.K^{-1})	Nu_p
34	56.1	45.9	31.8	32.5	9608	20418	130.1	10038	5941	14768	70.0
28.2	56.7	46.4	34.3	34.9	9063	21512	133.2	10323	4981	13359	63.3
22.5	57.7	46.3	35.7	36.2	8322	22157	135.1	10487	3992	11741	55.6
16.9	58.1	43.3	32.3	32.9	7317	20599	130.6	10086	2939	9955	47.2
11.2	58.8	42.2	33.6	34.1	6055	21191	132.3	10240	1942	7727	36.7
5.6	58.7	39.7	34.6	34.9	4283	21603	133.5	10346	951	5049	24.0
2.7	57.7	37.5	35	35.2	2841	21788	134.0	10393	447	3157	15.0

(e) Zigzag channel 3 mm, Q_u=400 L.h^{-1}

Q_p (L.h^{-1})	$T_{p,in}$ (°C)	$T_{p,out}$ (°C)	$T_{u,in}$ (°C)	$T_{u,out}$ (°C)	U (W.m^{-2}.K^{-1})	Re_u	Nu_u	h_u (W.m^{-2}.K^{-1})	Re_p	h_p (W.m^{-2}.K^{-1})	Nu_p
33.8	56	44.4	26.9	27.9	8857	14623	100.4	7685	5835	14993	71.1
28	56.5	42.1	23.1	24.2	8159	13391	96.2	7306	4762	13483	64.1
22.5	57.8	44.8	31.6	32.4	7878	16260	105.7	8153	3950	12029	57.0
16.9	58.4	42.4	29.6	30.4	6992	15538	103.4	7951	2925	10181	48.3
11.3	58.8	38.9	27.6	28.3	5787	14818	101.1	7742	1908	7881	37.5
5.7	58.1	33.2	25.8	26.3	4190	12563	93.3	7035	847	5303	25.4
2.9	55.8	28	24.5	24.8	2963	13712	97.3	7407	426	3452	16.5

(f) Zigzag channel 3 mm, Q_u=300 L.h^{-1}

Q_p (L.h^{-1})	$T_{p,in}$ (°C)	$T_{p,out}$ (°C)	$T_{u,in}$ (°C)	$T_{u,out}$ (°C)	U (W.m^{-2}.K^{-1})	Re_u	Nu_u	h_u (W.m^{-2}.K^{-1})	Re_p	h_p (W.m^{-2}.K^{-1})	Nu_p
33.8	57.1	50.2	39.1	40.1	8554	14301	87.3	6811	6143	15313	72.4
28	57.4	49.1	37.9	38.9	8030	13964	86.3	6722	5066	13830	65.4
22.4	57.8	47.8	36.7	37.6	7398	13628	85.3	6632	4023	12152	57.5
16.8	58.3	45.9	35	35.9	6591	13128	83.7	6495	2985	10223	48.4
11.2	58.8	43	33.5	34.2	5521	12714	82.4	6380	1954	7916	37.5
5.6	58.7	38.5	32.2	32.6	3976	12305	81.1	6263	942	5108	24.3
2.7	57.7	34.4	31	31.2	2644	11954	80.0	6161	435	3109	14.8

(g) Zigzag channel 2 mm, Q_u=500 L.h^{-1}

Q_p (L.h^{-1})	$T_{p,in}$ (°C)	$T_{p,out}$ (°C)	$T_{u,in}$ (°C)	$T_{u,out}$ (°C)	U (W.m^{-2}.K^{-1})	Re_u	Nu_u	h_u (W.m^{-2}.K^{-1})	Re_p	h_p (W.m^{-2}.K^{-1})	Nu_p
15	58.2	41.8	30.5	31	9448	19790	128.2	9870	3870	12614	39.9
12.5	58.8	42	32.4	32.8	9305	20599	130.6	10086	3245	12287	38.9
10	58.9	39.6	30.7	31.1	8425	19834	128.3	9882	2551	10851	34.4
7.5	58.9	36.9	29.2	29.6	7394	19170	126.3	9700	1870	9234	29.3
4.9	58.5	33.3	27.9	28.2	6039	18560	124.4	9529	1169	7234	23.0
2.4	57.5	29.3	26.6	26.8	4096	18003	122.6	9369	553	4621	14.7
1.4	56	27	25.5	25.6	2805	17538	121.1	9233	312	3045	9.7

(h) Zigzag channel 2 mm, Q_u=400 L.h^{-1}

Q_p (L.h^{-1})	$T_{p,in}$ (°C)	$T_{p,out}$ (°C)	$T_{u,in}$ (°C)	$T_{u,out}$ (°C)	U (W.m^{-2}.K^{-1})	Re_u	Nu_u	h_u (W.m^{-2}.K^{-1})	Re_p	h_p (W.m^{-2}.K^{-1})	Nu_p
15.1	58.4	41	28.2	28.9	9566	15039	101.8	7807	3863	13876	43.9
12.5	58.8	41.6	31.3	31.9	8989	16115	105.2	8113	3228	12524	39.6
10	58.8	39.2	29.7	30.3	8185	15552	103.4	7955	2539	11082	35.1
7.45	58.4	36.2	28.2	28.7	7215	14996	101.7	7795	1840	9426	29.9
5	57.8	32.6	26.7	27	5955	14449	99.9	7633	1198	7418	23.6
2.5	55.3	28	25.4	25.6	4136	14003	98.3	7497	558	4804	15.4
1.6	53.3	25.8	24.2	24.3	2840	13592	96.9	7369	343	3145	10.1

(i) Zigzag channel 2 mm, Q_u=300 L.h^{-1}

Q_p (L.h^{-1})	$T_{p,in}$ (°C)	$T_{p,out}$ (°C)	$T_{u,in}$ (°C)	$T_{u,out}$ (°C)	U (W.m^{-2}.K^{-1})	Re_u	Nu_u	h_u (W.m^{-2}.K^{-1})	Re_p	h_p (W.m^{-2}.K^{-1})	Nu_p
15	58.4	44	32.5	33.2	9037	12414	81.5	6294	3943	14005	44.3
12.6	58.7	43.9	33.9	34.5	8480	12797	82.7	6403	3318	12616	39.9
10.1	58.9	43.6	35.4	35.9	7799	13211	84.0	6518	2659	11090	35.0
7.5	58.7	37.8	29.1	29.6	6764	11502	78.5	6026	1879	9343	29.6
5	58.5	34	27.4	27.8	5606	11033	76.8	5882	1211	7317	23.3
2.5	57.4	29.4	26	26.3	3937	10649	75.5	5761	576	4728	15.1
1.3	55.2	26.3	24.8	24.9	2494	10323	74.3	5655	285	2795	8.9

(j) Straight channel 4 mm, Q_u=500 L.h^{-1}

Q_p (L.h^{-1})	$T_{p,in}$ (°C)	$T_{p,out}$ (°C)	$T_{u,in}$ (°C)	$T_{u,out}$ (°C)	U (W.m^{-2}.K^{-1})	Re_u	Nu_u	h_u (W.m^{-2}.K^{-1})	Re_p	h_p (W.m^{-2}.K^{-1})	Nu_p
60.6	47.6	44.9	28.3	29.1	4266	18864	125.3	9615	6727	5114	32.5
50.7	48.1	45.4	30.2	30.9	3946	19701	127.9	9846	5657	4644	29.5
40	48	45.1	29.7	30.2	3271	19390	127.0	9761	4425	3740	23.8
30.1	58.3	53.3	31.1	31.8	2968	20103	129.1	9954	3616	3342	21.0
20.3	58.9	53.5	32.1	32.6	2132	20463	130.2	10050	2323	2317	14.6
10.6	59.5	54.1	32.8	33.1	1030	20780	131.1	10134	951	1071	6.7
5.3	59.3	51.5	33.3	33.6	811	21008	131.8	10193	107	836	5.3

(k) Straight channel 4 mm, Q_u=300 L.h^{-1}

Q_p (L.h^{-1})	$T_{p,in}$ (°C)	$T_{p,out}$ (°C)	$T_{u,in}$ (°C)	$T_{u,out}$ (°C)	U (W.m^{-2}.K^{-1})	Re_u	Nu_u	h_u (W.m^{-2}.K^{-1})	Re_p	h_p (W.m^{-2}.K^{-1})	Nu_p
60.5	47.9	46	33.6	34.2	3861	12714	82.4	6380	7429	4937	31.4
50.1	48.2	46.3	34.6	35.1	3485	12990	83.3	6457	6183	4327	27.5
40.2	48.6	46.5	35.1	35.5	3075	13100	83.7	6488	4978	3709	23.5
30.1	58.2	53.5	32.3	33	2805	12387	81.4	6287	4235	3342	21.0
20.5	58.7	53.8	33.5	34.1	2195	12687	82.3	6372	2905	2506	15.7
10.5	59.1	53.5	31	31.3	1033	11954	80.0	6161	1488	1099	6.9
5.2	59.2	51.7	34.1	34.4	789	12824	82.8	6411	729	826	5.2

(l) Straight channel 3 mm, Q_u=500 L.h^{-1}

Q_p (L.h^{-1})	$T_{p,in}$ (°C)	$T_{p,out}$ (°C)	$T_{u,in}$ (°C)	$T_{u,out}$ (°C)	U (W.m^{-2}.K^{-1})	Re_u	Nu_u	h_u (W.m^{-2}.K^{-1})	Re_p	h_p (W.m^{-2}.K^{-1})	Nu_p
33.8	57.4	51.7	32.6	33	5748	20735	131.0	10122	6233	6894	32.5
28.1	58	52	33.6	34.2	5044	21191	132.3	10240	5212	5895	27.8
22.5	58	50.9	30.3	30.8	4233	19656	127.8	9833	4143	4840	22.9
16.8	58.7	51.2	31.6	31.9	3391	20238	129.5	9990	3112	3764	17.8
11.3	59.1	51.6	32.6	33	2293	20690	130.9	10110	2105	2456	11.6
5.6	58.9	51.4	33.2	33.5	1190	20917	131.5	10169	1042	1232	5.8
2.9	58	47.7	33.6	33.9	922	21099	132.1	10217	521	947	4.5

(m) Straight channel 3 mm, Q_u=300 L.h^{-1}

Q_p (L.h^{-1})	$T_{p,in}$ (°C)	$T_{p,out}$ (°C)	$T_{u,in}$ (°C)	$T_{u,out}$ (°C)	U (W.m^{-2}.K^{-1})	Re_u	Nu_u	h_u (W.m^{-2}.K^{-1})	Re_p	h_p (W.m^{-2}.K^{-1})	Nu_p
33.9	57.3	51.5	29.6	30.5	5163	11661	79.0	6074	6234	6743	31.8
28.1	57.6	51	28.1	28.9	4569	11266	77.6	5954	5160	5792	27.3
22.4	58	50.4	25.9	26.7	3898	10700	75.7	5777	4107	4784	22.6
16.8	58.7	52	32.7	33.2	3189	12468	81.6	6310	3134	3707	17.5
11.2	58.9	51.6	31.6	32	2142	12143	80.6	6216	2086	2367	11.2
5.6	58.8	50.4	30.4	30.6	1075	11794	79.4	6114	1033	1130	5.3
3	58	46.7	29.6	29.8	895	11581	78.7	6050	536	933	4.4

(n) Straight channel 2 mm, Q_u=500 L.h^{-1}

Q_p (L.h^{-1})	$T_{p,in}$ (°C)	$T_{p,out}$ (°C)	$T_{u,in}$ (°C)	$T_{u,out}$ (°C)	U (W.m^{-2}.K^{-1})	Re_u	Nu_u	h_u (W.m^{-2}.K^{-1})	Re_p	h_p (W.m^{-2}.K^{-1})	Nu_p
15	58.8	51	29.9	30.2	4376	19435	127.1	9773	4167	4825	15.2
12.5	58.8	50.6	28.8	29.1	3734	18951	125.6	9639	3463	4060	12.8
10.1	58.9	49.9	28	28.3	3177	18603	124.5	9541	2786	3412	10.7
7.6	58.9	49.8	27.3	27.5	2357	18302	123.6	9455	2093	2485	7.8
5	58.5	49	26.7	26.9	1492	18045	122.7	9381	1365	1543	4.9
2.4	57	43.8	26.2	26.4	1113	17833	122.1	9320	623	1141	3.6
1.3	55.1	37.6	25.6	25.7	856	17580	121.2	9246	315	873	2.8

(o) Straight channel 2 mm, Q_u=300 L.h^{-1}

Q_p (L.h^{-1})	$T_{p,in}$ (°C)	$T_{p,out}$ (°C)	$T_{u,in}$ (°C)	$T_{u,out}$ (°C)	U (W.m^{-2}.K^{-1})	Re_u	Nu_u	h_u (W.m^{-2}.K^{-1})	Re_p	h_p (W.m^{-2}.K^{-1})	Nu_p
15	58.8	50.5	26.4	26.9	4169	10776	75.9	5801	4149	4833	15.2
12.5	59	50.6	27.5	27.9	3616	11058	76.9	5890	3468	4098	12.9
10	59.1	50	28.6	29	3035	11344	77.9	5978	2762	3363	10.6
7.5	59.1	50.5	29.5	29.8	2270	11555	78.6	6042	2081	2447	7.7
5	58.6	50.5	28.8	29	1312	11371	78.0	5986	1381	1370	4.3
2.6	57.6	46	27.8	27.9	1077	11084	77.0	5898	690	1116	3.5
1.3	55	38.4	26.7	26.8	810	10827	76.1	5818	318	832	2.6

2. Heat tranfer characterization with glycerol solution (74% mass fraction) as process fluid

(a) Zigzag channel 4 mm, Q_u=500 $L.h^{-1}$

Q_p ($L.h^{-1}$)	$T_{p,in}$ (°C)	$T_{p,out}$ (°C)	$T_{u,in}$ (°C)	$T_{u,out}$ (°C)	U ($W.m^{-2}.K^{-1}$)	Re_u	Nu_u	h_u ($W.m^{-2}.K^{-1}$)	Re_p	h_p ($W.m^{-2}.K^{-1}$)	Nu_p
30.8	56.5	52.2	27.9	28.2	1844	18577	124.4	9534	350	2026	23.7
25.5	56.7	51.5	26.1	26.4	1560	17811	122.0	9313	256	1691	19.9
21.1	56.9	52.2	28.6	28.8	1605	18863	125.3	9614	241	1740	20.4
19.0	57.1	50.9	24.9	25.1	1804	17282	120.3	9157	214	1985	23.3
14.2	57.6	50.8	26.5	26.8	1463	17978	122.5	9362	161	1577	18.5
9.5	57.5	49.8	25.8	26	1082	17661	121.5	9269	106	1144	13.4
4.7	56.8	39.4	24.8	25	1367	17240	120.1	9144	44	1468	17.3
2.4	55.2	34	24.2	24.3	1002	15762	115.1	8686	20	1058	12.4

(b) Zigzag channel 3 mm, Q_u=500 L.h^{-1}

Q_p (L.h^{-1})	$T_{p,in}$ (°C)	$T_{p,out}$ (°C)	$T_{u,in}$ (°C)	$T_{u,out}$ (°C)	U (W.m^{-2}.K^{-1})	Re_u	Nu_u	h_u (W.m^{-2}.K^{-1})	Re_p	h_p (W.m^{-2}.K^{-1})	Nu_p
28.4	56.6	49.6	27.8	28.1	3243	18546	124.3	9525	416	3700	32.5
23.6	56.9	48.6	25.7	26	2967	18909	125.5	9627	342	3341	29.4
19.1	57.3	49.4	26.7	27	2275	18063	122.8	9386	282	2494	21.9
14.3	57.7	47.4	24.4	24.6	2143	17071	119.6	9093	206	2342	20.6
9.4	58.2	47.6	25.4	25.6	1516	17513	121.0	9226	137	1612	14.2
4.8	57.4	42.1	23.4	23.5	1085	16651	118.1	8965	64	1135	10.0
2.4	55.7	30.9	22.1	22.2	1279	16116	116.3	8799	25	1350	11.9

(c) Zigzag channel 2 mm, Q_u=500 L.h^{-1}

Q_p (L.h^{-1})	$T_{p,in}$ (°C)	$T_{p,out}$ (°C)	$T_{u,in}$ (°C)	$T_{u,out}$ (°C)	U (W.m^{-2}.K^{-1})	Re_u	Nu_u	h_u (W.m^{-2}.K^{-1})	Re_p	h_p (W.m^{-2}.K^{-1})	Nu_p
10.5	58.2	44	26.1	26.4	3690	17822	122.0	9317	218	4113	24.1
8.4	57.6	41.3	22.9	23.2	3136	16478	117.6	8912	166	3449	20.3
6.3	57.4	39.3	24	24.3	2945	16945	119.1	9055	119	3216	18.9
4.4	56.6	38.5	23	23.2	2030	16528	117.7	8927	81	2157	12.7
2.2	53.6	29.3	21.5	21.7	1765	15902	115.6	8731	33	1862	11.0
1.2	49.8	25	20	20.1	1161	15325	113.5	8544	16	1203	7.1

3. Density of glycerol solution (74% mass fraction) measured by a density meter

T (°C)	20	25	30	35	40
ρ (kg.m^{-3})	1192	1190	1187	1184	1181

4. Viscosity of glycerol solution (74% mass fraction) measured by the Kinexus ultra+ rheometer

T (°C)	20	30	40	50	60
μ (mPa.s)	32.6	18.8	12.4	8.0	6.0